DYNAMIC SEA CLUTTER SIMULATION AT LOW GRAZING ANGLES

A THESIS SUBMITTED TO
THE GRADUATE SCHOOL OF NATURAL AND APPLIED SCIENCES
OF
MIDDLE EAST TECHNICAL UNIVERSITY

BY

MUHAMMED Z. ERDOĞAN

IN PARTIAL FULFILLMENT OF THE REQUIREMENTS
FOR
THE DEGREE OF MASTER OF SCIENCE
IN
ELECTRICAL AND ELECTRONICS ENGINEERING

JANUARY 2018

Approval of the thesis:

DYNAMIC SEA CLUTTER SIMULATION AT LOW GRAZING ANGLES

submitted by **MUHAMMED Z. ERDOĞAN** in partial fulfillment of the requirements for the degree of **Master of Science in Electrical and Electronics Engineering Department, Middle East Technical University** by,

Prof. Dr. Gülbin Dural Ünver
Dean, Graduate School of **Natural and Applied Sciences** _____

Prof. Dr. Tolga Çiloğlu
Head of Department, **Electrical and Electronics Engineering** _____

Prof. Dr. Sencer Koç
Supervisor, **Electrical and Electronics Eng. Dept., METU** _____

Examining Committee Members:

Prof. Dr. Mustafa Kuzuoğlu
Electrical and Electronics Engineering Department, METU _____

Prof. Dr. Sencer Koç
Electrical and Electronics Engineering Department, METU _____

Prof. Dr. Çağatay Candan
Electrical and Electronics Engineering Department, METU _____

Prof. Dr. Özlem Aydın Çivi
Electrical and Electronics Engineering Department, METU _____

Prof. Dr. Feza Arıkan
Electrical and Electronics Eng. Dept., Hacettepe University _____

Date: **24.01.2018**

I hereby declare that all information in this document has been obtained and presented in accordance with academic rules and ethical conduct. I also declare that, as required by these rules and conduct, I have fully cited and referenced all material and results that are not original to this work.

Name, Last Name: MUHAMMED Z. ERDOĞAN

Signature :

ABSTRACT

DYNAMIC SEA CLUTTER SIMULATION AT LOW GRAZING ANGLES

Erdoğan, Muhammed Z.
M.S., Department of Electrical and Electronics Engineering
Supervisor : Prof. Dr. Sencer Koç

January 2018, 100 pages

High-amplitude clutter signals may be observed during radar operation due to environmental objects having large surface areas. By Doppler processing, modern radars can discriminate between echoes from mobile targets and echoes from stationary objects like mountains, buildings and so on. However, there is no simple way to do this discrimination for sea clutter since sea is always on the move. Therefore, statistical and empirical models are frequently used to characterize sea clutter. Yet, such models are unlikely to predict sea clutter accurately, particularly in complex sea conditions. In this thesis, we approach this issue in a different way. Dynamic simulation of sea clutter is performed to obtain more accurate results. In this simulation, sea surface is modeled depending on time-varying environmental factors, like sea wave height. Therefore, change of clutter is compatible with temporal and spatial correlation of sea surface. Then, a model is suggested to mimic realistic sea clutter parameters like normalized radar cross sections and Doppler frequency shifts. By applying the suggested model to the generated sea surface in certain time periods, complex radar data matrix is constructed. Finally, the simulation results are analyzed and compared to

some of the available experimental data for different scenarios, and good agreement is observed.

Keywords: Dynamic Sea Surface, Dispersion Relation, GIT Model, Visibility Analysis, Radar Cross Section, Doppler Spread Modeling, Spectrogram

ÖZ

DÜŞÜK SIYIRMA AÇILARINDA DİNAMİK DENİZ KARGAŞASI BENZETİMİ

Erdoğan, Muhammed Z.
Yüksek Lisans, Elektrik ve Elektronik Mühendisliği Bölümü
Tez Yöneticisi : Prof. Dr. Sencer Koç

Ocak 2018 , 100 sayfa

Radar çalışması esnasında, büyük yüzey alanlı çevre elemanlarından kaynaklı yüksek genlikli kargaşa sinyalleri gözlenebilir. Günümüz radarları Doppler işleme ile hareketli hedeflerden oluşan yankıları, durağan olan dağ, bina vb. kaynaklı yankılardan ayırt edebilir. Fakat deniz sürekli hareket halinde olduğu için bu tip basit yöntemlerle bir ayrıştırma yapmak söz konusu değildir. Bu yüzden, istatistiksel ve ampirik modeller deniz kargaşasını karakterize etmek için kullanılır. Ancak, bu tip modellerin karmaşık deniz koşullarında, deniz kargaşasını doğru bir biçimde öngörebilmeleri için deniz yüzeyinin ayrıntılı bir modeli gereklidir. Bu tezde, bu konuyu farklı bir bakış açısıyla ele almaktayız. Daha doğru sonuçlar elde etmek için deniz kargaşasının dinamik olarak benzetimi yapılmaktadır. Bu benzetimde deniz yüzeyi çevresel etmenlere, özellikle deniz dalga yüksekliğinin zaman içerisindeki değişimine bağlı kalınarak modellenmiştir. Dolayısıyla, kargaşanın değişimi, deniz yüzeyinin zamansal ve uzaysal ilintisiyle uyumlu olmaktadır. Bundan sonraki aşamada düzgelenmiş radar kesit alanı ve Doppler frekans kayması gibi deniz kargaşası parametrelerinin gerçekçi bir şekilde modellemesi yapılmıştır. Önerilen modelin, üretilen deniz yüze-

yine belirli zaman aralıklarında uygulanmasıyla birlikte karmaşık radar veri matrisi elde edilmiştir. Son olarak, farklı senaryolar için elde edilen sonuçlar analiz edilip, mevcut birkaç deneysel veriyle karşılaştırılmış ve sonuçların uyumlu olduğu gözlenmiştir.

Anahtar Kelimeler: Dinamik Deniz Yüzeyi, Dağılma Bağıntısı, GIT Modeli, Görünürlük Analizi, Radar Kesit Alanı, Doppler Saçılım Modelleme, Spektrogram

To my family

ACKNOWLEDGMENTS

I would like to express my sincere gratitude to my supervisor Prof. Sencer Koç for his guidance, criticism, advice, continuous support and insights that made this study possible.

I would like to thank the committee members Prof. Mustafa Kuzuoğlu, Prof. Özlem Aydın Çivi, Prof. Feza Arıkan, and Prof. Çağatay Candan for examining this thesis.

I am also thankful to my employer TÜBİTAK İLTAREN and my colleagues for encouraging me during my M.Sc. studies.

I would like to thank to my family and my fiancée for their support, patience and love.

TABLE OF CONTENTS

LIST OF TABLES

TABLES

LIST OF FIGURES

FIGURES

LIST OF ABBREVIATIONS

1D	One Dimensional
2D	Two Dimensional
3D	Three Dimensional
CSIR	Council for Scientific and Industrial Research, South Africa
FFT	Fast Fourier Transform
FEM	Finite Element Method
GB	Gigabyte
GIT	Georgia Institute of Technology
HH	Horizontal transmit Horizontal receive
HV	Horizontal transmit Vertical receive
I/Q	In phase/Quadrature
JONSWAP	Joint North Sea Wave Project
LGA	Low Grazing Angle
LL	Log-likelihood
MFIE	Magnetic Field Integral Equation
MLE	Maximum Likelihood Estimation
MoM	Method of Moments
MTI	Moving Target Indicator
NRCS	Normalized Radar Cross Section
NRL	Naval Research Laboratory
PEC	Perfect Electrical Conductor
pdf	probability density function
PM	Pierson-Moskowitz
PRF	Pulse Repetition Frequency
PRI	Pulse Repetition Interval
PSD	Power Spectral Density
RAM	Random Access Memory
RCS	Radar Cross Section
SKL	Symmetrized Kullback-Leibler
SS	Sea State
SWH	Significant Wave Height
TSC	Technology Service Corporation

VH	Vertical transmit Horizontal receive
VV	Vertical transmit Vertical receive
WAFO	Wave Analysis for Fatigue and Oceanography
WAFOL	WAFO Lagrange
WMO	World Meteorological Sea State

CHAPTER 1

INTRODUCTION

Sea clutter poses many problems during the detection operation of radars especially for the small targets like boats, buoys and so on. This issue does not only depend on the time-varying amplitude of the sea clutter, but also it depends on the dynamic behavior of the Doppler shifts due to the changing status of the sea surface. Although land clutter mostly can be suppressed by using Moving Target Indicator (MTI) due to being mostly non-mobile environment, sea clutter requires adaptive MTI processing to diminish the effects of the clutter, for which the filter parameters vary in time. Therefore, better characterization of the sea clutter has been demanded for decades to improve the clutter suppression of such radar signal processing tools.

Researchers have endeavored to characterize sea clutter in terms of grazing angle, radar frequency, polarization and various environmental parameters. The amplitude characteristics of the sea clutter is mostly qualified by the reflectivity parameter, σ_0 (a.k.a. normalized radar cross-section (NRCS)). The direct solution for the σ_0 can be obtained by solving the Maxwell's harmonic time dependent integral equations. The calculations for a such way is very difficult even if the Perfect Electrical Conductor (PEC) condition is assumed for the sea surface [1]. Holliday et al. [2] developed an iterative numerical method, namely forward-backward method, to solve MFIE (magnetic field integral equation) for PEC surfaces. Yet, the calculations are still complex, computationally slow and cover only 1D surfaces. According to Ward et al. [1], physical optics (Kirchoff) approximation and composite model suggested by Wright and Valenzula is not valid at low grazing angles (LGAs) due to multipath, shadowing and polarization dependent behavior of the sea clutter. Arikan et al. [3]

utilizes the two scale roughness model and physical optics to obtain NRCS at various frequencies and grazing angles. However, shadowing effect is neglected for grazing angles less than 18°, and grazing angles less than 3° have not been covered in [3].

Empirical and statistical models for the amplitude characterization of the sea clutter have become more practical and efficient solutions for this problem. The Georgia Institute of Technology (GIT) model suggested by Horst et al. [4] has been widely accepted as a proper model to characterize mean σ_0 with respect to grazing angle, radar frequency, angle between sea waves and radar direction, and so called Sea State (SS). The term sea state is used to describe the arduousness of the sea surface. Nathanson [5] presents data tables of average reflectivity for different polarizations, sea states, radar frequencies and needless to say grazing angles. These tables give rise to NRL (Naval Research Laboratory) sea clutter model as there are discrepancies between the collected average reflectivity data and the GIT model's results especially for the sea states lower than 3 [6]. There are many other empirical models to characterize the mean reflectivity, σ_0, some of which are examined in Chapter 3.

Considering as a random process, sea clutter amplitude variation can be described by the distributions like Rayleigh, Log-normal, Weibull and Gamma. The amplitude statistics depends on the detector type, size of the radar resolution cell, operational frequency and the roughness of the sea surface [7]. The statistical models are constructed based on the empirical data. In the literature, distributions of the analyzed sea clutter mostly resemble to log-normal, Weibull and K-distributions [8]. Also, the simulation results for different grazing angles presented in [9] resemble mostly Log-normal distribution, K-distribution and Weibull distribution.

In addition to the amplitude characteristics, the Doppler characterization of the sea clutter is generally made up from the empirical data. The study of Pidgeon et al. [10] can be accepted as a milestone that shows the dependency of the Doppler shifts and bandwidth on the polarization, sea waveheight, wind speed, angle between sea wave direction and radar propagation direction. From their measurements in 1991, Lee et al. [11] able to separate so called Bragg scattering mechanism from non-Bragg scattering mechanisms of the sea clutter in the Doppler frequency domain. Furthermore, they conclude that non-Bragg returns for horizontal polarization dominates the

one in the vertical polarization. Walker [12] observes that three different scattering mechanism dominates the clutter returns in Doppler domain from the wind-wave tank measurements. He also models the Doppler spectra combined up two or three Gaussian line shapes depending on the polarization in [13]. A more practical model developed by Whitrow [14] scales the model of Walker in [13] by the factors obtained from the graphical results of Rozenburg's wave tank measurements [15]. Whitrow [14] also relates the average RCS (radar cross section) to the Doppler spectral parameters such as Bragg peak frequency and spike bandwidth. These mechanisms and parameters are given in detail Chapter 3 and 4, respectively. In recent years, with the increasing number of shared measurement data by the like of Council for Scientific and Industrial Research (CSIR), South Africa field experiment datasets [16], more refined Doppler spectra models for the sea clutter have been introduced. Watts et al. [17] relate the mean Doppler frequency to the local clutter return power at medium grazing angles in 2016.

In this thesis, we have proposed a sea clutter model that adaptively changes the scattering parameters in compliance with a generated dynamic 3D sea surface. To achieve that, first we apply geometric optics and modified GIT model to the generated sea surface and obtain RCS matrix whose dimensions are range and time. Then, we generate Doppler spectra by using the obtained RCS matrix within the methods of Whitrow [14]. Since we attempt to mimic CSIR's sea clutter datasets collected at low grazing angles [16], some modifications on the parameters have been made. We also observe from the datasets in [16] that the local clutter intensities affect the Doppler shifts. Hence, we model the Doppler shifts similar to the findings of Watts [17]. After that, we generate correlated clutter returns by performing Fourier synthesis of complex Gaussian process with the modeled spectra. To validate the performed synthesis, conservation of energy is ensured through Monte Carlo iterations. Finally, by applying all mentioned processes to the each range bin, we complete the complex radar data matrix.

1.1 Outline

The organizational flow of this work is presented as follows. In Chapter 2, some terms related to sea and environment conditions like significant waveheight and sea state are explained. Then, in Section 2.2 physical phenomena of dispersion relation and sea wave spectrum are discussed. Finally, in Section 2.3 the generation of 3D sea surface by using WAFO and WAFOL [18, 19] toolboxes is presented with the demonstration of generated sample sea surfaces.

In Chapter 3, brief review of sea clutter theory is given. Firstly, amplitude characteristics of sea clutter is investigated in Section 3.2. Calculation of the clutter amplitude and empirical sea clutter models and their comparison are examined in this section. Secondly, in Section 3.3, Doppler characteristics of sea clutter is examined through the introduced scattering mechanisms. Finally, concept and construction of radar data matrix are probed in Section 3.4.

Chapter 4 intensifies on the proposed sea clutter model. The procedures and aims are introduced in Section 4.1. Section 4.2 shows how we compute the RCS values of each range bin and time interval from the generated sea surface. In this section, grazing angle calculation, application of empirical model and visibility analysis have been discussed. After that, generation of correlated Doppler shifts based on the suggested Doppler characteristics is analyzed in Section 4.3. Finally, scope and limitations of the suggested model are discussed in Section 4.4.

In Chapter 5, simulation results of the proposed model for the generated scenarios are presented. Also, some of the results are compared with the available data [16]. Initially, RCS results are demonstrated and compared via histograms in Section 5.1. After that, Doppler shift results are inspected through spectrograms and mean Doppler shifts are compared graphically in Section 5.2. Finally, in Section 5.3, analysis of sea wave physics from the simulation results is monitored.

In the end, this study is concluded in Chapter 6 by making comments and evaluations on the proposed model, simulation results and the future studies.

CHAPTER 2

MODELING SEA SURFACES

In this chapter, generation of time-varying (dynamic) sea surface to create scenarios for the proposed clutter simulations, and background information about sea waves are investigated. Initially, some terms and basic concepts regarding sea wave structures and environmental conditions are defined. Then, mathematics lying behind the sea surface waves like sea surface spectrum and spreading is examined. After that, key algorithms used to obtain realistic and time-varying structure of sea surfaces for this work, are presented. Finally, some simulation samples of resulting sea surfaces are given.

2.1 General Concept of Sea Waves

For this study, sea surface and its time dependency must be well-defined in order to obtain more desirable clutter model. Therefore, some terminology related to sea structure and sea conditions must be comprehended. First, sea wave structure is discussed. In Figure 2.1, one dimensional sea wave is illustrated.

One needs to distinguish between wave and surface elevation from Figure 2.1 to clarify the terms of wave height H, period T, and length L. Surface elevation is the instant elevation of the sea surface relative to the zero reference level, while the wave is surface elevation profile between two successive upward or downward reference level crossings in a certain time interval.

The wave height, H (as in Fig. 2.1), is defined as the vertical distance between

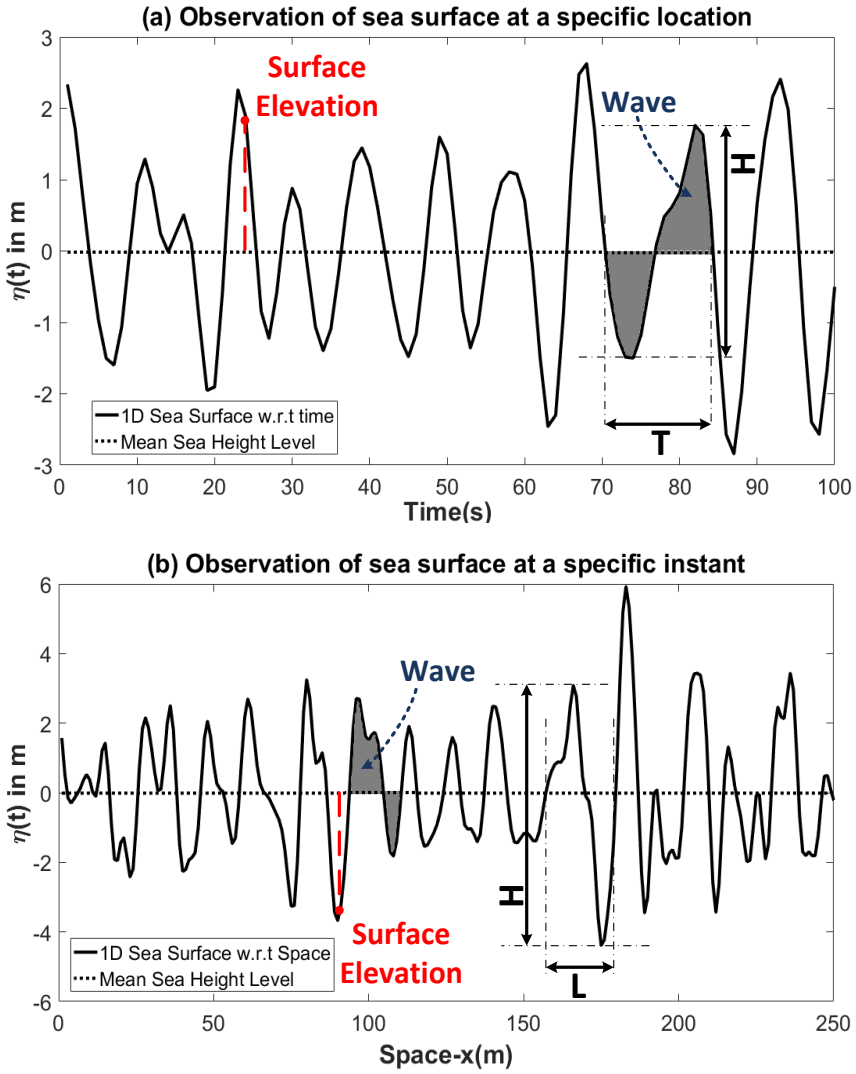

Figure 2.1: 1D sea surface at a specific point of observation [20].

maximum and minimum peaks of surface elevation in a wave. Similarly, the wave period, T (as in Fig. 2.1), is the duration between two successive zero crossings of the wave at a fixed location of the surface [20]. In analogy to the wave period, which is in time domain, spatial period or wave length, L, is the distance between two successive crests at an instant [5]. Another important term is the Significant Wave Height (SWH), $H_{1/3}$, which is the average of the highest one-third of waves in a wave record. This term is used to determine sea state, defined later on this section. SWH is given by

$$H_{1/3} = \frac{1}{N/3} \sum_{i=1}^{N/3} H_i \tag{2.1}$$

where i is the rank number of the wave, that is, $i = 1$ is the highest wave, $i = 2$ is the second highest wave in the wave record [20]. Nathanson [5] states that a widespread approximation for wind generated waves is $H_{1/3} = 4\sigma_h$, where σ_h denotes the standard deviation of the wave heights.

To characterize the sea surface in both spatial and temporal domain, one needs to define temporal and spatial wavenumber terms, which are essential to generate and analyze sea surfaces as discussed in Section 2.2. Temporal frequency is defined in terms of wave period by $\omega = 2\pi/T$; whereas spatial wavenumber is determined from the wavelength by $k = 2\pi/L$ [5]. In addition to these fundamental sea surface descriptions, to better analyze the sea clutter, some terms concerning sea conditions must be defined [1, 5, 21]:

Wind Wave: Waves arousing from the wind blowing on a water surface that leads to random sea surface height profile.

Swell: Having almost sinusoidal shape and having larger wavelength than standard local wind waves, swells occur from the wind waves that move out of the area where they are originally excited.

Gravity Wave: Essential waves excited due to motion of Earth and gravity acting on water mass. If wavelength of sea waves is greater than approximately $2\,\mathrm{cm}$, these waves are called as gravity waves.

Capillary Waves: Ripple waves that occur due to surface tension and have wavelength less than $2\,\mathrm{cm}$.

Whitecaps: As their front face rolling backwards, breaking waves on the open sea are called as whitecaps due to their foamy appearance. Whitecaps are highly-related to wind conditions.

Fetch: The distance over which the wind has been blowing with a constant speed and direction.

Duration: This term refers to how long a time the wind has been blowing with a constant speed and direction.

Fully Developed Sea: Equilibrium state reached after adequate fetch and duration for given wind force.

Sea State: The scale of the roughness of the sea surface, generally determined from the present largest wave heights. Beaufort Scale can be given as counter example to sea state, since while it scales wind speed, it is confused with sea state scale. Occasionally, Beaufort scale can give approximate result on sea state. However, the sea state is determined from the sea waves itself, not the wind. Sea states and descriptions are given for different sea scales in Table 2.1, and Table 2.2.

Table2.1: World Meteorological Organization (WMO) Sea State [22].

SS	SWH (m)	Description
0	0	Calm - glassy
1	0 - 0.1	Calm - rippled
2	0.1 - 0.5	Smooth - wavelets
3	0.5 - 1.25	Slight
4	1.25 - 2.5	Moderate
5	2.5 - 4	Rough
6	4 - 6	Very rough
7	6 - 9	High
8	9 - 14	Very high
9	>14	Phenomenal

WMO Sea State, as in Table 2.1, shows the sea states for wind waves; however, Douglas Scale, as in Table 2.2 calculates the sea states by taking swells into account besides the wind waves.

2.2 Wave Spectrum of Sea Surface

Being a stochastic process, spectral analysis for sea surface should be apprehended to generate such random surfaces. The spectrum shows the energy distribution on both spatial and temporal frequency domains.

Table2.2: Douglas Sea State [1].

SS	SWH (ft)	Wind Speed (kn)	Fetch (nmi)	Duration (h)	Description
1	0 - 1	0 - 6	-	-	Smooth
2	1 - 3	6 - 12	50	5	Slight
3	3 - 5	12 - 15	120	20	Moderate
4	5 - 8	15 - 20	150	23	Rough
5	8 -12	20 - 25	200	25	Very rough
6	12 - 20	25 - 30	300	27	High
7	20 - 40	30 - 50	500	30	Very high
8	>40	>50	700	35	Precipitous

Sea surface can be represented by a superposition of arbitrary sinusoidal waves that have different amplitudes, frequencies, phases and directions. Fourier series expression can be used to represent rough sea surface as [23]:

$$\widetilde{\eta}(t) = \sum_{i=1}^{N} \widetilde{a}_i \cos\left(\omega_i t + \widetilde{\alpha}_i\right). \tag{2.2}$$

Where, $\widetilde{\eta}(t)$ is the surface elevation at instant t and at a fixed point, $\widetilde{a}_i$ is the Rayleigh distributed amplitude of i^{th} component, ω_i is the temporal frequency of i^{th} component, $\widetilde{\alpha}_i$ is the uniformly distributed random phase of the i^{th} component, N is the number of total wave components.

Equation 2.2 yields stationary, Gaussian 1D surface elevation at a specific point of observation. To describe realistic 3D moving waves, the horizontal dimension component, that is, x, y-space dependency, should be inserted in Eq. 2.2 as

$$\widetilde{\eta}(x, y, t) = \sum_{i=1}^{N} \sum_{j=1}^{M} \widetilde{a}_{i,j} \cos\left(\omega_i t - k_i x \cos\theta_j - k_i y \sin\theta_j + \widetilde{\alpha}_{i,j}\right) \tag{2.3}$$

where k is the spatial wavenumber, and θ represents the direction of propagation. Adding space components to the 1D random phase and amplitude model of sea surface would introduce two more indices in the summation (i.e., for spatial wavenumber, k and direction, θ, there would be different indices than temporal frequency, ω, separately). However, spatial wavenumber and temporal frequency are related by the

so called dispersion relation; hence, index for spatial wavenumber, k and index for temporal frequency, ω, are the same [20].

2.2.1 Dispersion Relation

The temporal frequency of sea wave, ω, is related to the spatial wavenumber, k, by the *dispersion relation* [20]. The dispersion relation is

$$\omega^2 = gk \tanh kd \tag{2.4}$$

where d is the water depth and g is the gravitational acceleration.

There are two practical approximations that can be made on Eq. 2.4 [24]:

- ***Deep-water approximation:*** If the water depth d is much larger than the water wavelength L, this approach is valid. In this case, $d \gg L$, $kd \gg 1$, and $\tanh(kd) = 1$. Applying these assumptions on Eq. 2.4 yields:

$$\omega^2 = gk. \tag{2.5}$$

- ***Shallow-water approximation:*** If the water depth d is much smaller than the water wavelength L, this approach is valid. In this case, $d \ll L$, $kd \ll 1$, and $\tanh(kd) = kd$. Applying these assumptions on Eq. 2.4 yields:

$$\omega^2 = k^2 gd. \tag{2.6}$$

2.2.2 Spectrum Models for Sea Surfaces

Based on parameters like wind speed, fetch and water depth, several formulation for wave spectra has been suggested. Most of the wave spectra is in the following form:

$$S(\omega) = \frac{A}{\omega^5} e^{-B/\omega^4}. \tag{2.7}$$

Variance of the spectrum defined also as the area under the spectrum, can be characterized with respect to SWH, $H_{1/3}$. Therefore, wind speed can be used in the formulation of sea spectrum since SWH depends on it [25] as this relation can be observed

from sea state scale Tables 2.1 and 2.2. Bearing these considerations in mind, several spectrum models based on measurements and observations are explained in the following sections.

2.2.2.1 Pierson-Moskowitz Spectrum

After performing various measurements in the North Atlantic, Pierson and Moskowitz have characterized the sea spectrum based on the assumption that the sea is fully-developed [26]. This approach is rather simple than other sea spectrum models due to fully-developed sea assumption. Based on the many data collected under steady wind speed conditions, calculated wave spectrum is plotted in Figure 2.2 [27]. For

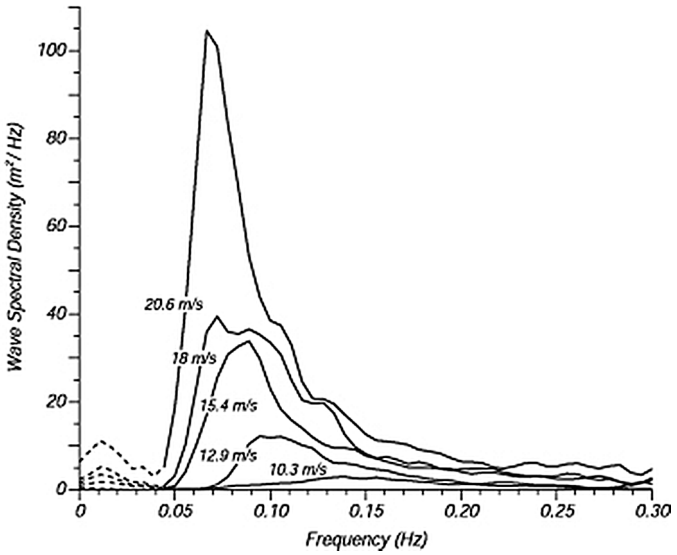

Figure 2.2: Fully developed sea spectrum at different wind speeds according to L. Moskowitz (1964) [27].

the plots given in Fig. 2.2, a good approximation is provided by [23]

$$S(\omega) = \frac{2\pi\alpha g^2}{\omega^5} \exp\left[\frac{-5}{4}\left(\frac{\omega_p}{\omega}\right)^4\right] \tag{2.8}$$

where ω is the angular frequency, ω_p is the peak angular frequency of the spectrum, $g = 9.81\ m/s^2$ is the gravitational acceleration, $\alpha = 8.1 \times 10^{-3}$ is Philip's constant.

Peak frequency ω_p and peak period T_p is related with wind speed U as:

$$\omega_p = \frac{0.855g}{U} \qquad T_p = \frac{2\pi}{\omega_p} = \frac{U}{0.136g} \tag{2.9}$$

To obtain variance of the sea surface elevation, $S(\omega)$ should be integrated over all ω [27]:

$$\sigma_h^2 = \int_0^\infty S(\omega)d\omega = 2.47 \times 10^{-3}\frac{U^4}{g^2}. \tag{2.10}$$

Recall that $H_{1/3} = 4\sigma_h$, so the SWH is:

$$H_{1/3} = 0.22\frac{U^2}{g}. \tag{2.11}$$

The wind speed dependency of both peak period and SWH for Pierson-Moskowitz spectrum is given in Figure 2.3. These relationships are used to generate sea surface in the next section.

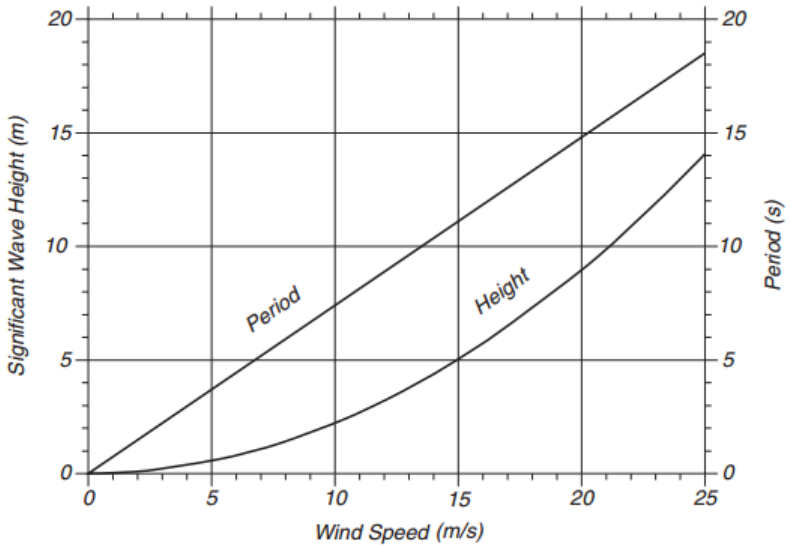

Figure 2.3: Relationship between $H_{1/3}$, T_p and U for PM Spectrum [27].

2.2.2.2 JONSWAP Spectrum

In conjunction with Joint North Sea Wave Observation Project (JONSWAP), Hasselman et al. stated that even if fully-developed sea condition is valid, wave to wave interactions like white-capping would be still notable [28]. In addition, Pierson-Moskowitz spectrum cannot model limited fetch conditions due to the fully-developed sea assumption. However, JONSWAP spectrum relates parameters like angular peak frequency to fetch along with the wind speed, and it has a sharper spectrum shape. The suggested spectrum is illustrated in Figure 2.4 (Numbers given in Fig. 2.4 are the

station number, not distance. As distance to shore, namely fetch, increases with the increasing station number). The formula given below is for the JONSWAP spectrum,

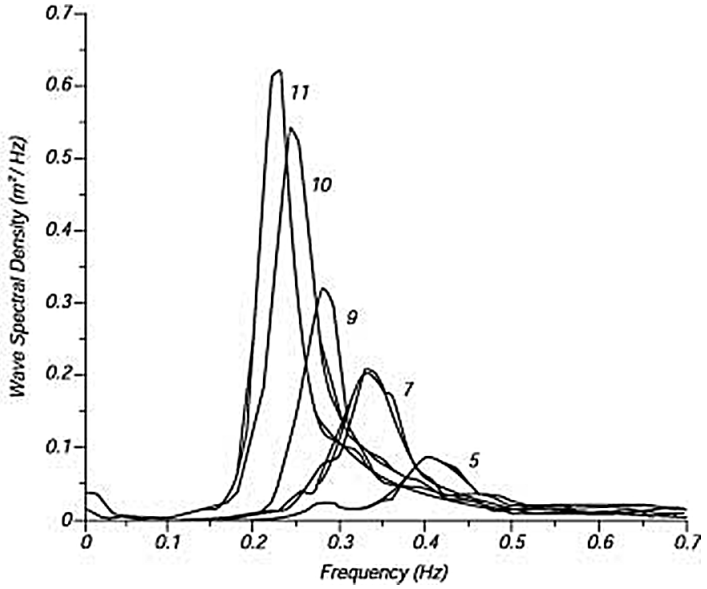

Figure 2.4: Wave spectrum of a continuously developing sea at different fetches proposed by Hasselman et al. (1973) [27].

and its similarity to Pierson-Moskowitz spectrum is obvious. The basic difference from the Pierson-Moskowitz spectrum is the introduction of the peak enhancement factor, r. It must also be noted that the relation between different parameters in JONSWAP spectrum is different from the Pierson-Moskowitz spectrum as

$$S(\omega) = \frac{\alpha g^2}{\omega^5} \exp\left[-\frac{5}{4}\left(\frac{\omega_p}{\omega}\right)^4\right]\gamma^r, \tag{2.12a}$$

$$r = \exp\left[-\frac{(\omega-\omega_p)^2}{2\sigma^2\omega_p^2}\right] \tag{2.12b}$$

where the parameters determined from the measurements are [27]

$$\gamma = 3.3, \tag{2.13a}$$

$$\sigma = \begin{cases} 0.07, & \text{if} \quad \omega \leq \omega_p, \\ 0.09, & \text{otherwise}, \end{cases} \tag{2.13b}$$

$$\alpha = 0.076\left(\frac{U^2}{Fg}\right)^{0.22}, \tag{2.13c}$$

$$\omega_p = 22\left(\frac{g^2}{FU}\right)^{1/3} \tag{2.13d}$$

in which, F is the fetch, g is the gravitational acceleration, and U is the wind speed.

Since JONSWAP spectrum is more realistic and more extensive for different environment conditions, this model is used in the generation of sea surface in this study.

In the foregoing discussion, one dimensional spectrum models is inspected; however to create 3D sea surface, one needs two dimensional sea surface spectrum. The sea surface can be represented as a 2D Fourier series in terms of random Gaussian components, temporal frequency ω, spatial wavenumber k, and spreading direction θ as given in Eq. 2.3. As examined in Section 2.2.1, temporal frequency is related to spatial wavenumber through the dispersion relation. Therefore, 2D spectrum can be represented in terms of temporal frequency and spreading direction. In the next section, directional spreading concept is clarified.

2.2.3 Directional Spreading

Direction of sea wave motion gives rise to angular distribution in spectrum that can be represented by a spreading function. Two dimensional sea surface spectrum can be written in terms of 1D spectrum $S_{1D}(\omega)$ and spreading function $D(\omega, \theta)$ as [18]:

$$S_{2D}(\omega, \theta) = S_{1D}(\omega)D(\omega, \theta). \tag{2.14}$$

Recall that total energy for 2D spectrum should remain same as in the previous 1D case, since spreading function only distributes the spectrum in different angles/directions, but it neither amplifies nor attenuates the spectrum. This essential condition for the determination of spreading function [29] is:

$$\int_{-\infty}^{\infty}\int_{-\pi}^{\pi} S(\omega, \theta)d\omega d\theta = \int_{-\infty}^{\infty}\int_{-\pi}^{\pi} S(\omega)D(\omega, \theta)d\omega d\theta = \int_{-\infty}^{\infty} S(\omega)d\omega. \tag{2.15}$$

There are numerous spreading function types like *cosine-squared*, Mitsuyasu, Donelan and Hasselman. Donelan and *cosine-squared* spreading functions are frequency independent; thus, these ones do not represent spectral density appropriately, especially at peak frequency. Mitsuyasu and Hasselman spreading functions both have dependency on frequency; yet, only Mitsuyasu spreading is investigated since this spreading type is employed during the generation of the sea surface.

2.2.3.1 Mitsuyasu Spreading Function

This frequency dependent function, which is actually based on *cosine-squared* spreading function, is expressed as

$$D(\omega,\theta) = \frac{\Gamma(s+1)}{2\sqrt{\pi}\Gamma(s+0.5)}\left[\cos^2\left(\frac{\theta-\theta_0}{2}\right)\right]^s \tag{2.16}$$

where θ_0 represents the wind direction, $\Gamma(s)$ symbolizes the Gamma function, and parameter s governs the directional energy distribution over the frequencies as follows:

$$s = \begin{cases} 9.77\left(\dfrac{\omega}{\omega_p}\right)^{-2.5} & \text{if} \quad \omega \leq \omega_p, \\ 6.97\left(\dfrac{\omega}{\omega_p}\right)^{5} & \text{if} \quad \omega > \omega_p. \end{cases} \tag{2.17}$$

From Eq. 2.17, s reflects that angular spreading increases at frequencies close to the peak spectral frequency, and it decreases at frequencies below than the peak frequency of the wave spectrum [29].

2.3 Generation of Sea Surfaces

In this study, WAFO [18] and WAFOL [19] toolboxes are utilized to generate sea surface, and these toolboxes work jointly in the MATLAB^{TM} environment. The toolboxes are generally used to create oceanic waters. However, CSIR's experimental data [1] used for comparing the simulated clutter in Chapter 5 is obtained from coastal waters. Environmental conditions like SWH, peak wave period and water depth can be adjusted for the generated sea surfaces. In order not to distort the dispersion relation, approximate depth of water where data is collected is entered as water depth (approximately $30\,\mathrm{m}$). In addition, for fully developed seas, relations based on wind speed are used to determine the SWH and peak period of the generated sea surface, as can be seen in Figure 2.3. However, for coastal waters wind speed may not match these curves. As given in the experimental reports of field tests conducted by CSIR [1], measured SWH is not consistent with the given wind speed according to the curves. Yet, peak period point on the curve corresponding to the measured SWH

matches to the observed peak wave period. Therefore, given SWH and peak period is directly used for the generation of sea surface.

In addition to setting various environmental conditions during the sea surface generation process, WAFO toolbox enables users to adjust different mechanisms like spectrum type, spreading type, front-to-back asymmetry of sea wave. As stated on the previous sections, JONSWAP spectrum and frequency dependent Mitsuyasu spreading is used throughout the entire work. Resulting directionally spreaded wavenumber spectrums of the WAFO generated sea surfaces are shown in Figure 2.5 for respectively $0°$ and $45°$ spreading directions.

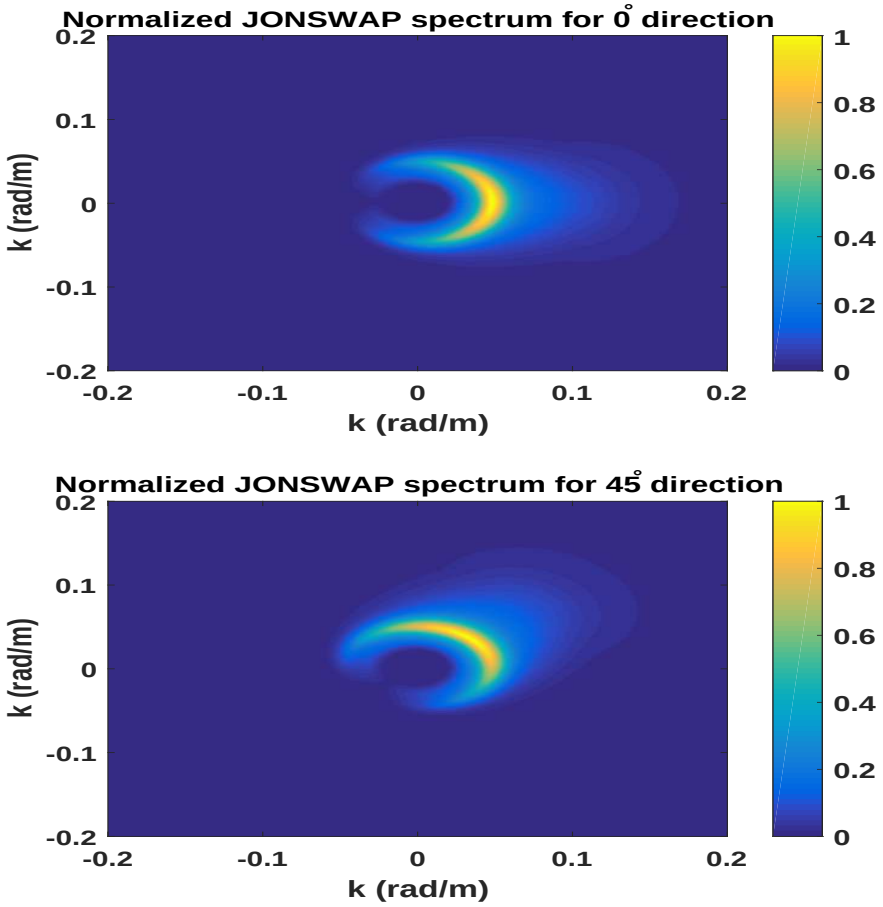

Figure 2.5: Normalized directional spread spectrum of generated sea surface for both $0°$ spreading direction, and $45°$ spreading direction.

WAFO toolbox [18] models the sea surface's stationary mechanisms while treating sea surface as Gaussian stochastic process. The Gaussian 2D wave generated by

WAFO represented in time t and space x as

$$z(t,x) = m + \sum_{i=0}^{N} \sqrt{S_i} R_i \cos\left(k_i x - \omega_i t + \widetilde{\alpha}_i\right) \tag{2.18}$$

where R_i is independent Rayleigh distributed amplitudes, S_i is weight factor of JONSWAP spectral density $S(\omega)$, and m is the mean surface height.

On the other hand, WAFOL toolbox adds both horizontal and vertical motion to the static sea surface by employing Gauss-Lagrange model [19]. Horizontal process, $l(t,x)$ is dependent on the vertical Gaussian process, $z(t,x)$. Indeed, horizontal process $l(t,x)$ is obtained by linear filter application to the vertical process $z(t,x)$. This is where non-Gaussian characteristics of Lagrange waves are added. The applied filter has complex response and front-back asymmetry, which causes peaked crests and shallower troughs, is given to the generated waves with the additional l_α/ω^2 term in the filter response. Therefore, the filter response having dependency on frequency ω and water depth h is given as:

$$H(\omega) = p(\omega) e^{j\theta(\omega)} = j\frac{\cosh(hk)}{\sinh(hk)} + l_\alpha/\omega^2. \tag{2.19}$$

If the term l_α is set to zero, then no front-to-back asymmetry would be obtained as generated sea waves appear smoother. The horizontal process generated by WAFOL [19] is presented as:

$$l(t,x) = \sum_{i=0}^{N} \sqrt{(S(\omega_i)\Delta\omega)} p(\omega_i) R_i \cos\left(k_i x - \omega_i t + \widetilde{\alpha}_i + \theta(\omega_i)\right). \tag{2.20}$$

Given Lagrange and Gaussian waves are 2D waves, that is the processes are composed of only x component of the space and time component t. The 3D versions of these processes can be handled in the same sense. Since the equations and relations for 3D Gauss-Lagrange processes are very complex, one can found them in [19].

3D model of randomly generated sea surfaces at a certain instant is presented in Figure 2.6. Note that axes of Fig. 2.6 are not scaled. In addition, top view images of the sea surfaces at different instants are given in Figure 2.7 and Figure 2.8 for respectively 0° and 45° spreading directions.

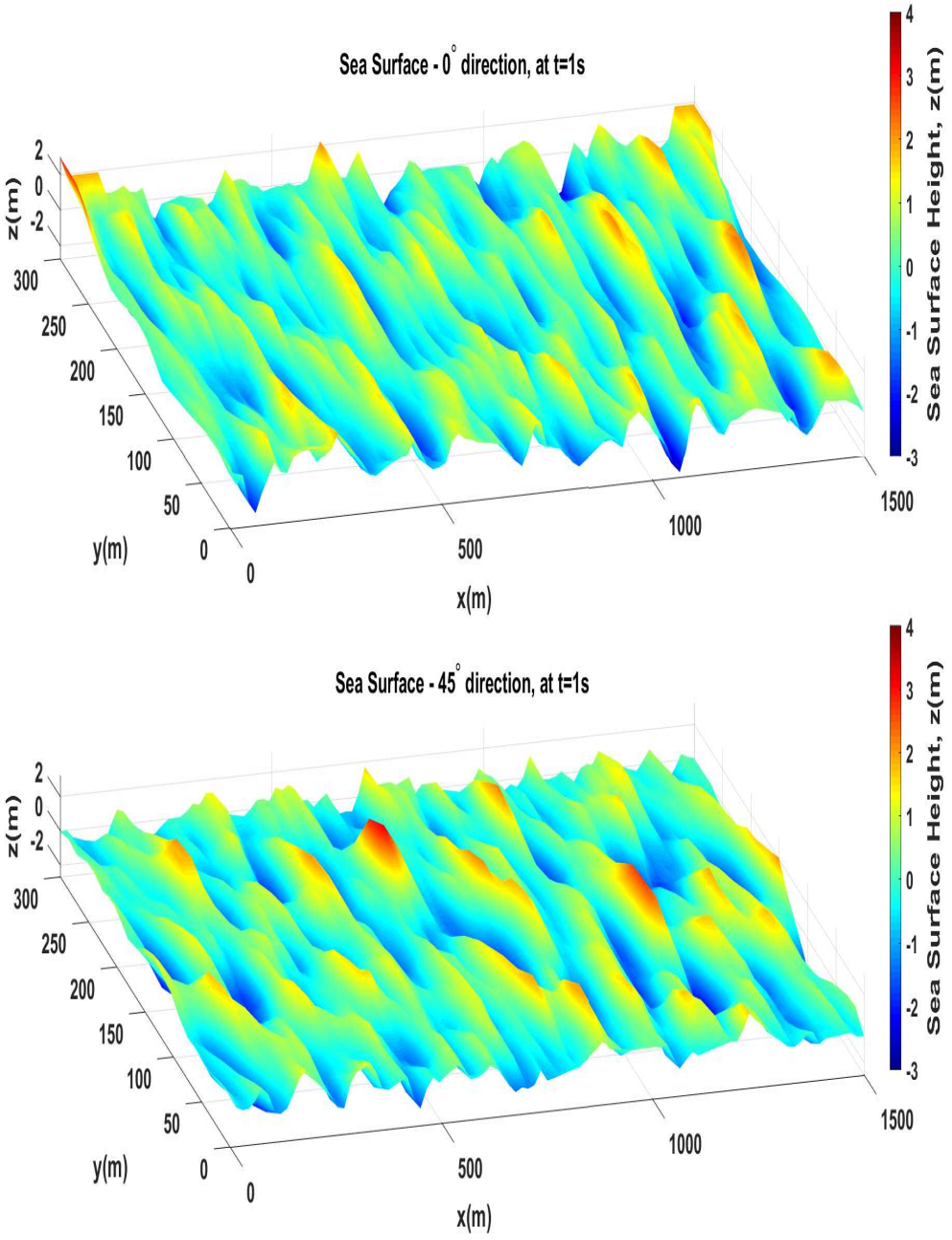

Figure 2.6: 3D view of generated sea surfaces ($l_\alpha = 0.75$).

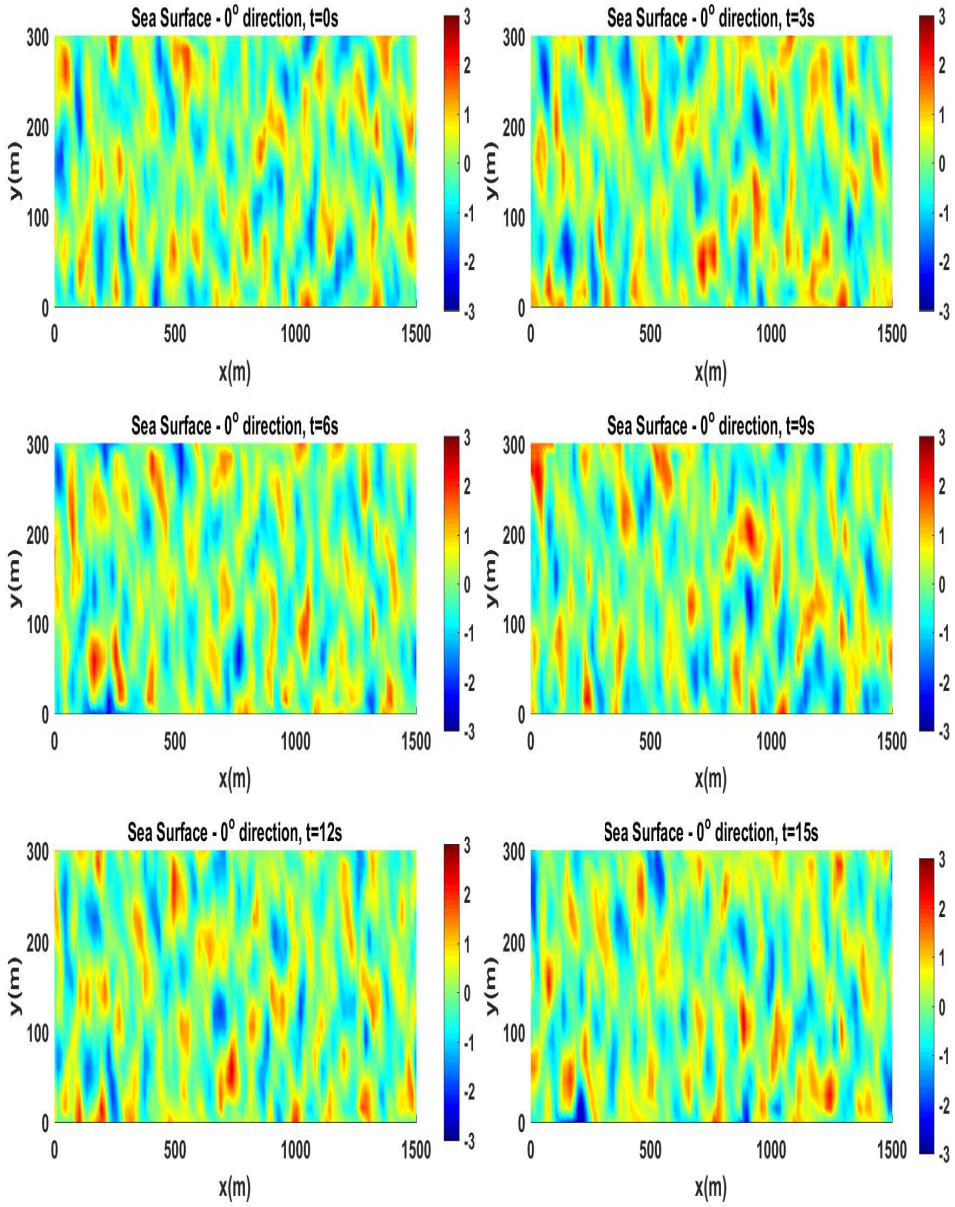

Figure 2.7: Top view of generated sea surface ($l_\alpha = 0.75$), moving with angle of $0°$, at different instants.

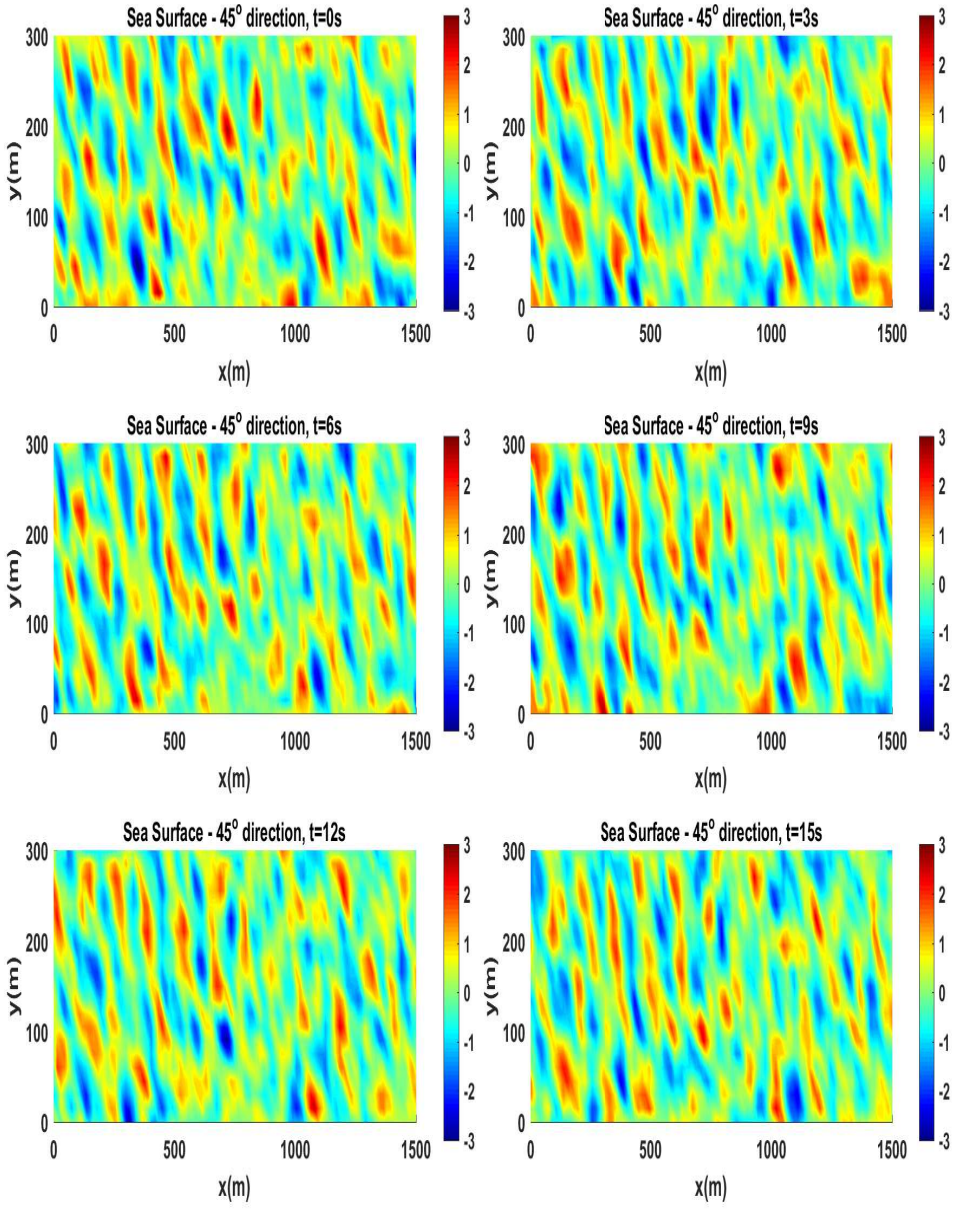

Figure 2.8: Top view of generated sea surface ($l_\alpha = 0.75$), moving with angle of $45°$, at different instants.

CHAPTER 3

THEORETICAL BACKGROUND OF CLUTTER

3.1 Introduction to Clutter

Before proceeding the outline of this chapter, the term clutter should be defined properly. Clutter is defined as the unwanted returns from the environment which deteriorate the detection of echoes from target [8]. The scattering properties of clutter vary with radar parameters like frequency and polarization, and also by the environmental conditions such as steadiness and reflectivity. Most generic way to represent scattering properties is the use of polarization scattering matrix as in Eq. 3.1, which consists of polarization, amplitude and phase terms as [30]:

$$S = \begin{bmatrix} \sqrt{\sigma_{HH}} e^{j\phi_{HH}} & \sqrt{\sigma_{HV}} e^{j\phi_{HV}} \\ \sqrt{\sigma_{VH}} e^{j\phi_{VH}} & \sqrt{\sigma_{VV}} e^{j\phi_{VV}} \end{bmatrix}. \tag{3.1}$$

In this thesis, we only investigate VV polarization. Due to having lack of experimental data to compare with our results, the other polarization types are not covered in this study. Therefore, only $\sqrt{\sigma_{VV}} e^{j\phi_{VV}}$ part of the scattering matrix is examined and modeled. Since the region of interest is only the sea surface, all clutter terms are considered as surface clutter.

Amplitude characteristics of the sea surface clutter in the next section which presents the fundamental computations for $\sqrt{\sigma_{VV}}$. After that, Doppler characteristics of the sea clutter are investigated which directly affects the phase term $e^{j\phi_{VV}}$ of the reflectivity parameter. Finally, radar data matrix which is combined from the complex reflectivity parameters, is presented.

3.2 Amplitude Characteristics of the Sea Clutter

In this section, initially the amplitude calculations of the clutter regardless of being sea or land. Then, the empirical models for the sea surface reflectivity and their comparison are given.

3.2.1 Amplitude Computation for the Clutter

The calculations presented in this subsection are valid for both land and sea surface clutter.

Surface clutter's amplitude depends on the illuminated area. To measure and compare the effects of surface clutter, the clutter RCS is divided by the illuminated area to obtain the clutter reflectivity (sometimes referred to as normalized RCS, NRCS) and is denoted by σ_0 [8]. The radar range equation for the backscatter power from surface clutter is given by

$$C = \frac{P_t G A_e \sigma_0 A_c}{(4\pi)^2 R^3} \tag{3.2}$$

where P_t is the transmitted power, G is the antenna gain, A_e is the effective antenna aperture, R is the range, A_c is the illuminated clutter area. So, if one obtains σ_0 and A_c, received clutter power can be estimated which may give prior knowledge about clutter properties of the operational environment.

One of the key parameters to determine A_c, is the grazing angle. The angle between the incident ray and the tangent to the sea surface in the plane defined by the incident ray and the surface normal is referred to grazing angle [31]. Its complementary angle is called incidence angle, which is the angle between the inbound radiation and normal to the sea surface. Grazing angle also has a great impact on σ_0 as discussed in the next section. At low grazing angles, length and width of circular arc sector shaped clutter area is illustrated in Figure 3.1. Radar resolution cell is comprised of range resolution $c\tau/2$, assuming no pulse compression, and angle resolution $R\theta_B$. At large distances and LGAs, the clutter area can be approximated by a rectangle and it is given by the equation

$$A_c = R\theta_{AZBW}(c\tau/2)\sec(\psi_g) \tag{3.3}$$

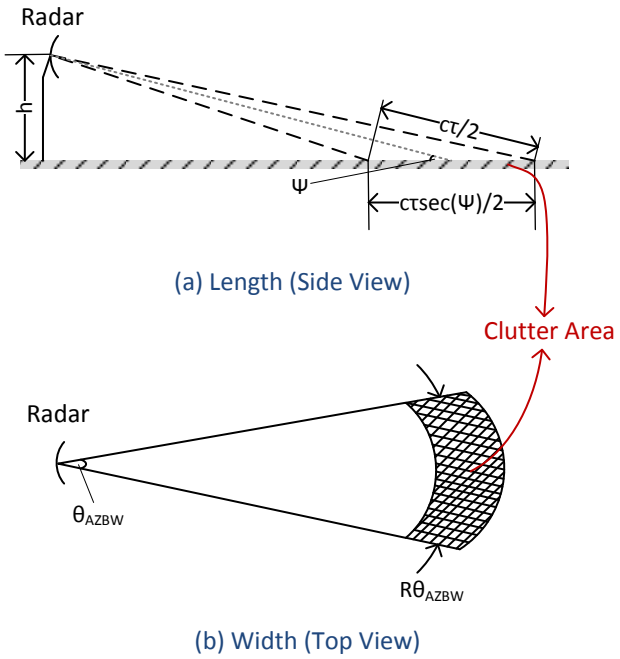

Figure 3.1: (a) Length for clutter area, (b) width for clutter area [8].

where clutter area's length is determined by τ: pulse width, ψ_g: grazing angle, and c: propagation velocity (almost equal to light speed), while its width is determined by R: range, and θ_{AZBW}: azimuth beamwidth [8].

Since now A_c is determined, one should characterize σ_0 to estimate backscatter power from the clutter. It is almost impossible to directly compute the value of the reflectivity term; thus, empirical models have been proposed especially for the sea clutter.

3.2.2 Empirical Sea Clutter Models

Due to randomness of sea surface, it is difficult to make a model for NRCS - σ^0. Besides, to determine σ^0, the electromagnetic computation methods like method of moments (MoM) and finite element method (FEM) could be very time-consuming so that these methods may not be the best choice for modeling dynamic sea surfaces [32]. Therefore, based on the experimental observations, empirical models have been developed in which σ^0 have shown dependency on wind direction, sea conditions,

grazing and look angle, and so on [1].

There are several empirical models, yet GIT model is employed in this study. In the following parts, empirical models with their mathematical expressions are given. After that, empirical models are compared to enlighten why GIT model is chosen for the simulation.

3.2.2.1 NRL Model

Naval Research Laboratory researchers developed an empirical sea clutter model by parameterizing Nathanson's experimental results for σ_0. The main aim is to provide a model that fits these experimental results better than the GIT model especially at lower sea states. The model is valid at the grazing angles from 0.1° to 10° in the frequency range of $0.5\,\mathrm{GHz}$ to $35\,\mathrm{GHz}$ [6]. The suggested expression for the vertical polarization is in the form of [33]

$$\sigma^0_{VV} = c_1 + c_2 \log \sin\alpha + \frac{(c_3 + c_4\alpha)\log f}{1 + c_5\alpha + c_6 SS} + c_7(1+SS)^{\frac{1}{2 + c_8\alpha + c_9 SS}} \quad (3.4)$$

where α is the grazing angle, f is the radar frequency, and SS is the sea state. Constants used in Eq. 3.4 is given in Table 3.1:

Table3.1: Optimized constant parameters for the NRL model.

Constants	**For VV Polarization**
c_1	-48.56
c_2	26.30
c_3	29.05
c_4	-0.5183
c_5	1.057
c_6	0.04839
c_7	21.37
c_8	0.07466
c_9	0.04623

3.2.2.2 GIT Model

This model is the most commonly used one to determine mean NRCS at LGAs. The model is valid from $1\,\mathrm{GHz}$ to $100\,\mathrm{GHz}$ and for the grazing angles from 0.1° to 10°. It is combined from three separate factors: Wind speed factor, A_w, multipath or interference factor, A_i, and wind direction factors, A_u, which are functions of several parameters [14].

The model, as given in [1], starts with conversion of the sea state, SS, to the wind speed, U, and average wave height, h_{av}, in meters:

$$U = 3.16SS^{0.8}, \tag{3.5}$$

$$h_{av} = 0.00452U^{2.5}. \tag{3.6}$$

There is a roughness parameter that is used in multipath (interference) factor, A_i:

$$\sigma_\phi = (14.4\lambda + 5.5)\frac{\phi_{gr}h_{av}}{\lambda} \tag{3.7}$$

where λ is the radar wavelength and ϕ_{gr} is the grazing angle in radians.

The multipath (interference) term, A_i, is given by:

$$A_i = \frac{\sigma_\phi^4}{1+\sigma_\phi^4} \tag{3.8}$$

Wind direction term, A_u, is

$$A_u = \exp\left(0.2\cos\left(\theta_w\right)(1-2.8\phi_{gr})(\lambda+0.015)^{-0.4}\right) \tag{3.9}$$

where θ_w is the wind direction with respect to the radar look direction.

The last factor, wind speed factor, A_w is:

$$A_w = \left(\frac{1.94U}{1+\frac{U}{15.4}}\right)^{\frac{1.1}{(\lambda+0.015)^{0.4}}}. \tag{3.10}$$

All of these factors are combined up to yield σ^0 in dB, for the both horizontal and vertical polarizations as:

$$\sigma^0_{HH} = 10\log\left(\lambda\phi_{gr}^{0.4}A_iA_uA_w\right) - 54.09, \tag{3.11}$$

$$\sigma^0_{VV} = \sigma^0_{HH} - 1.05\ln\left(h_{av}+0.015\right) + 1.09\ln\left(\lambda\right) + 1.27\ln\left(\phi_{gr}+0.0001\right) + 9.7 \tag{3.12}$$

3.2.2.3 TSC Model

This model is also based on Nathanson's data whose structure resembles the GIT model. However, the TSC model involves the parametric calculations which are composed of the data collected under ducting conditions. Grazing angle is covered from 0° to 10°, while the frequency is on the $0.5\,\mathrm{GHz}$ to $35\,\mathrm{GHz}$ range [1]. NRCS equations for the TSC model as follows:

$$\sigma^0_{HH} = 10\log(1.7\times10^{-5}\phi_{gr}^{0.5}G_uG_wG_A/(3.2808\lambda_{rad}+0.05)^{1.8}), \tag{3.13}$$

$$\sigma^0_{VV} = \begin{cases} \sigma^0_{HH} - 1.73\ln(8.225\sigma_z+0.05) + 3.76\ln\lambda_{rad} & \\ +2.46\ln(\sin\phi_{gr}+0.0001)+24.2672 & f<2\text{GHz}, \\ \sigma^0_{HH} - 1.05\ln(8.225\sigma_z+0.05) + 1.09\ln\lambda_{rad} & \\ 1.27\ln(\sin\phi_{gr}+0.0001)+10.945 & f\geq 2\text{GHz} \end{cases} \tag{3.14}$$

where

$$\sigma_z = 0.03505SS^{1.95}, \quad \sigma_\alpha = 4.5416\phi_{gr}(3.2808\sigma_z+0.25)/\lambda_{rad},$$
$$G_A = \sigma^1_\alpha.5/(1+\sigma^1_\alpha.5), \quad U = 3.189SS^{0.8}, \quad Q = \phi_{gr}^{0.6},$$
$$A_1 = (1+(\lambda_{rad}/0.00914)^3)^{0.1}, \quad A_2 = (1+(\lambda_{rad}/0.00305)^3)^{0.1},$$
$$A_3 = (1+(\lambda_{rad}/0.00914)^3)^{Q/3}, \quad A_4 = 1+0.35Q,$$
$$A = 2.63A_1/(A_2A_3A_4), \quad G_w = [(1.9438U+4)/15]^A,$$
$$G_u = \begin{cases} 1 & \phi_{gr} = \pi/2, \\ \exp(0.3\cos\theta_w\exp(-\phi_{gr}/0.17)/(10.7636\lambda^2_{rad}+0.005)^{0.2}) & \phi_{gr}<\pi/2 \end{cases} \tag{3.15}$$

λ_{rad} is the radar wavelength, ϕ_{gr} is the grazing angle, θ_w is the radar look direction w.r.t. wind direction, and SS is the Douglas sea state. NRCS values do not diminish rapidly with decreasing grazing angle in TSC model due to taking ducting effects into account.

3.2.2.4 Hybrid Model

This model has agreement with both Nathanson's data and the GIT model. It is valid up to grazing angles of 30° [1].

$$\sigma^0 = \sigma^0_{ref} + K_g + K_s + K_p + K_d \tag{3.16}$$

in which σ^0_{ref} is a reference reflectivity which is validated for sea state 5, grazing angle of 0.1°, upwind condition, and VV polarization. K_g, K_s, K_p and K_d are parameters dependent on grazing angle ϕ_{gr}, polarization, sea state SS, radar look direction with respect to wind direction θ_w. Then,

$$\sigma^0_{ref} = \begin{cases} 24.4 \log f - 65.2 & f \leq 12.5\text{GHz} \\ 3.25 \log f - 42 & f > 12.5\text{GHz} \end{cases} \tag{3.17}$$

$$\phi_{ref} = 0.1 \tag{3.18}$$

$$\phi_t = \arcsin\left(0.0632\lambda_{rad}/\sigma_h\right)180/\pi \tag{3.19}$$

where ϕ_{ref} is the reference angle, ϕ_t is the transitional angle. λ_{rad} is the radar wavelength, and $\sigma_h = 0.031SS^2$ which stands for the rms wave height. After that,

$$\text{If} \quad \phi_t \geq \phi_{ref}, K_g = \begin{cases} 0 & \phi < \phi_{ref} \\ 20\log(\phi/\phi_{ref}) & \phi_{ref} \leq \phi \leq \phi_t \\ 20\log(\phi_t/\phi_{ref}) + 10\log(\phi/\phi_{ref}) & \phi_t \leq \phi \leq 30^\circ \end{cases} \tag{3.20}$$

$$\text{If} \quad \phi_t < \phi_{ref}, K_g = \begin{cases} 0 & \phi \leq \phi_{ref} \\ 10\log(\phi/\phi_{ref}) & \phi > \phi_{ref} \end{cases} \tag{3.21}$$

$$K_s = 5(SS - 5) \tag{3.22}$$

$$\text{For VV pol.,} \quad K_p = 0 \tag{3.23}$$

$$K_d = (2 + 1.7\log(0.1/\lambda_{rad}))(\cos\theta_w - 1) \tag{3.24}$$

3.2.3 Comparison of Empirical Models

Generally, almost all of the empirical sea clutter models are functions of sea state or wind speed, grazing angle, radar frequency, polarization and wind direction. All comparisons are made with the assumption of VV polarization and upwind condition.

NRCS, σ^0 versus grazing angle graphs are given in Figure 3.2 for sea states 1, 2 and 3, at $6\,\mathrm{GHz}$ radar frequency. Figure 3.2 shows that as grazing angle increases σ^0

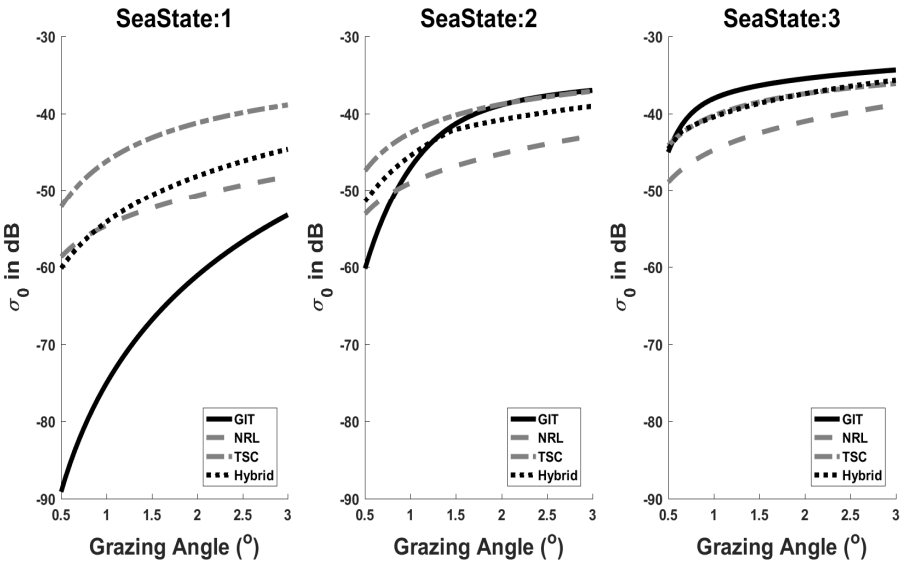

Figure 3.2: σ_0 vs. grazing angle at f=$6\,\mathrm{GHz}$, for sea states 1,2,3.

value increases. In Figure 3.3 σ^0 against frequency graphs for different sea states at 1.5° grazing angle are demonstrated. It can be deduced from Figure 3.3 that the

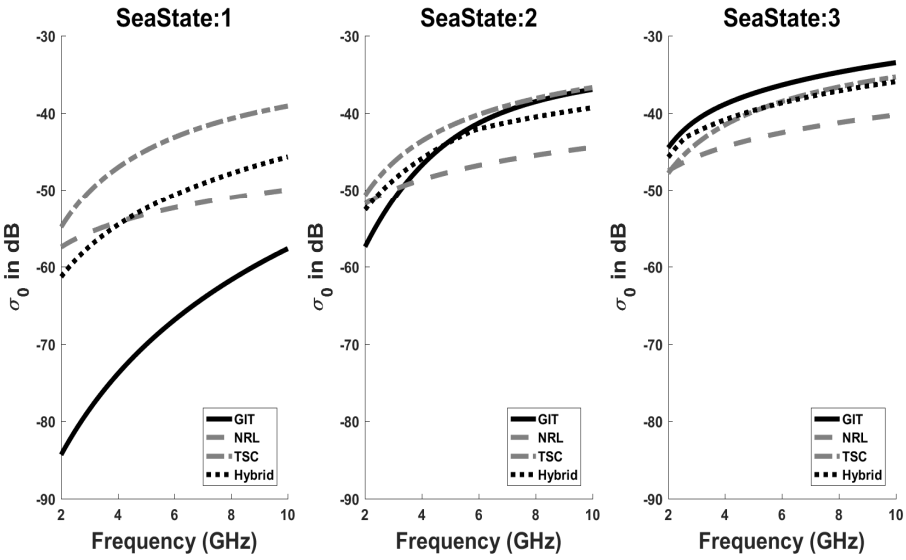

Figure 3.3: σ_0 vs. frequency at 1.5° grazing angle, for sea states 1,2,3.

clutter return increases with increasing frequency. In Figure 3.2 and 3.3, one can also see that GIT model underestimates σ^0 at low sea states with respect to the other empirical models, especially at lower frequencies and lower grazing angles. This

could be due to not taking evaporation ducts into account [34]. Since no evaporation duct situation is assumed in the proposed clutter model, GIT model is eligible for the work. In addition, since the aim of the suggested model is to create a simulation that dynamically adapts itself to the sea surface, used empirical model should contain sea surface height term. GIT and Hybrid models are the only well-accepted empirical models that contain sea surface wave height term. However, Hybrid model contains some terms to model the effects of evaporation ducts [34]. Consequently, the GIT model is the most appropriate choice for the purpose and scope of this study.

3.3 Doppler Characteristics of the Sea Clutter

Due to being static, land clutter results in zero mean Doppler shift which cause almost no difference between phase terms given in Eq. 3.1 for different regions of the monitored area. However, because of being always on the motion, Doppler spectrum of the sea clutter may vary from depending on both space and time. Doppler shifts modeled on Chapter 4, give rise to diversity of phases for different sectors of modeled sea as non-zero mean Doppler shifts are valid generally. Most particularly, there can be seen large differences in the center Doppler frequency when wind direction changes. There are three different conditions with respect to difference between radar look direction and wind direction that gives idea where the mean Doppler frequency shift lies on the spectrum:

Upwind: When radar look direction opposes the wind direction. Positive mean Doppler shift is expected.

Downwind: When radar look direction is along the wind direction. Negative mean Doppler shift is expected.

Cross-wind: When radar look direction is perpendicular to the wind direction. Zero mean Doppler shift is expected.

Evidently, this information is not sufficient to characterize sea clutter in both amplitude domain and Doppler frequency domain. Generally, clutter reflectivity increases with increasing radar frequency and grazing angle. On the next section, empirical

approaches to model magnitude of sea clutter are presented. To characterize sea clutter, especially for Doppler spectra, Ward and Walker et al. described three types of scattering mechanisms, namely Bragg, whitecaps and sea spikes [35]. On the Chapter 4, the terminology of scattering mechanisms as defined in [35] are adopted.

3.3.1 Bragg Scattering

Bragg scattering mechanism mentioned in [35] is indeed a composite scattering model that contains large and small scale components. The large component is due to large swells (gravity waves) which can be handled by Bragg resonance scattering mechanism. Bragg resonance scattering model treat these long-wavelength water waves as sinusoidals when the Bragg resonance condition is met. Bragg resonance condition is:

$$n\lambda_{radar} = 2\lambda_{water}\cos\psi_g, \quad n = 0, 1, 2... \tag{3.25}$$

where λ_{radar} is the radar wavelength, λ_{water} is sea surface wavelength, and ψ_g is the grazing angle. When this condition is met, according to Bragg scattering mechanism, scattered waves deploy constructive interference as it can be seen from Figure 3.4.

At microwave frequencies, where the resolution of the radar increases, Bragg resonance scattering mechanism is no more sufficient to characterize the clutter, since it can only model the large scale component. Composite model features small gravity waves and capillary waves as small scale component. Composite model treats sea surface as small ripples riding on large sea swells. Small perturbation method is applied to small scale component, while geometric or physical optics is applied to the large scale component.

The simple Bragg scattering mechanism described in [35], does not fit to many experimental observations by itself, especially for high-wind conditions and HH polarization. Therefore, it is concluded that there is non-Bragg mechanism that collaborates with Bragg mechanism in order to give rise to the experimentally observed phenomena [8] and [31].

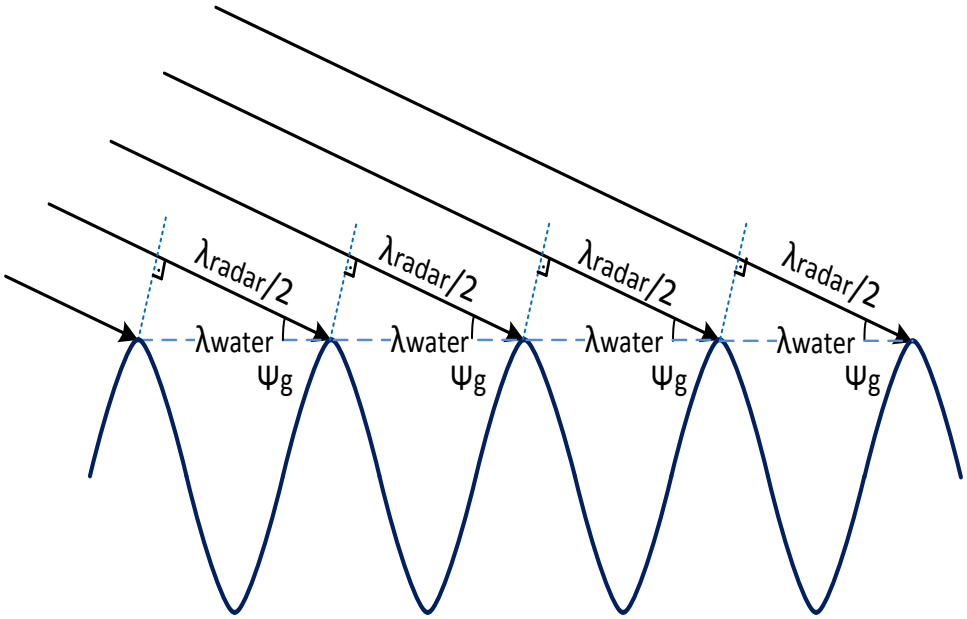

Figure 3.4: Schematic drawing of Bragg resonance scattering mechanism [31].

3.3.2 Whitecaps and Sea Spike Scattering

Non-Bragg scattering occurs due to breaking waves or waves which are about to break, both having long wavelength. Non-Bragg scattering mechanisms can be distinguished by their duration. Some of these mechanisms last about hundred milliseconds, then fade out swiftly; however, others continue about one to few seconds [31]. In the literature, non-Bragg scattering is referred to sea spikes. Yet, since they show different characteristics, non-Bragg scattering is split into whitecaps scattering and sea spike scattering as described in [35].

Whitecap scattering is due to whitecaps popping-out of breaking waves, which last in the order of seconds. It is polarization independent and causes larger mean RCS and Doppler frequency shift than Bragg scattering.

Lasting about one to two hundred milliseconds, sea spike scattering is due to crests of waves about to break. RCS due to this burst scattering is highly polarization dependent, that is HH pol. yields much higher RCS values than VV polarization [35].

3.4 Radar Data Matrix

Recall that the term $(c\tau/2)$ in Eq. 3.3 represents range resolution, and range resolution can be related to the pulse width τ, since throughout this study no pulse compression is assumed. Pulse width can be considered as time sampling interval of the radar receiver, that is, if one scatterer is detected at t_0 seconds, another scatterer can be detected at least the time of $t_0 + \tau$ seconds. Thus, if radar receiver takes samples from time t_0 to $t_n = t_0 + n\tau$, this corresponds to taking samples from range R_0 to $R_n = R_0 + n(c\tau/2)$. The range interval from R_0 to R_n, from which radar receiver extracts I/Q (in-phase/quadrature) data, is called the range strip, and it consists of n range bins. These range bins are referred to *fast-time* samples. Radar receiver can extract all I and Q data for each range bin from the transmission of a single pulse. In most applications, using a single pulse not sufficient to gather enough energy from the target return. Therefore, pulse trains are employed. Assuming radar transmits m successive pulses, there are m samples from a single range bin, separated by PRI (pulse repetition interval) in time. Hence, m successive pulses from a range cell form a data vector in the so called *slow-time* dimension. As fast time's sampling interval is pulse width (and accordingly range resolution, $c\tau/2$), slow time's sampling interval is PRI. Since radar PRI is much higher than pulse width, it s easy to see why these are called fast and slow time [30]. Figure 3.5 below may be helpful to better grasp these concepts. Both fast and slow time I/Q samples yield $m \times n$ dimensional complex data matrix shown in Figure 3.6. This complex data matrix is required to demonstrate evident time-variance of resulting clutter model in Chapter 5.

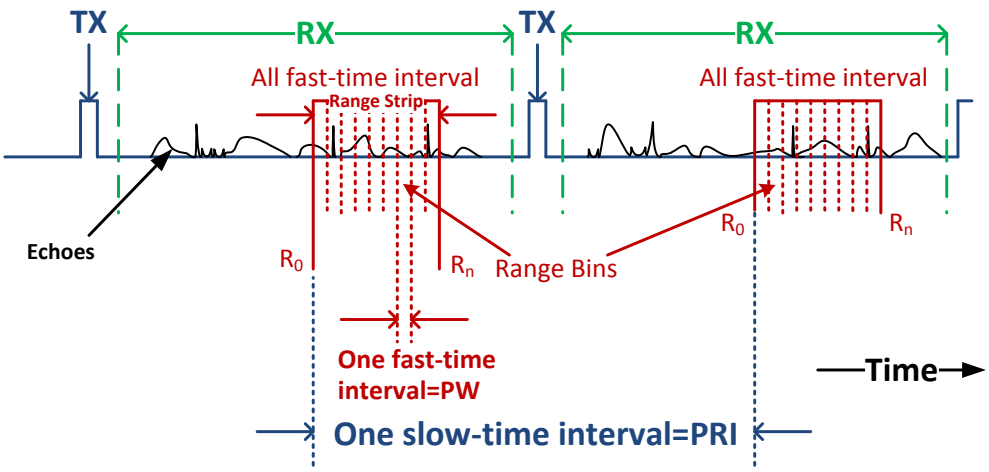

Figure 3.5: Demonstration of fast and slow time during radar transceiving operation.

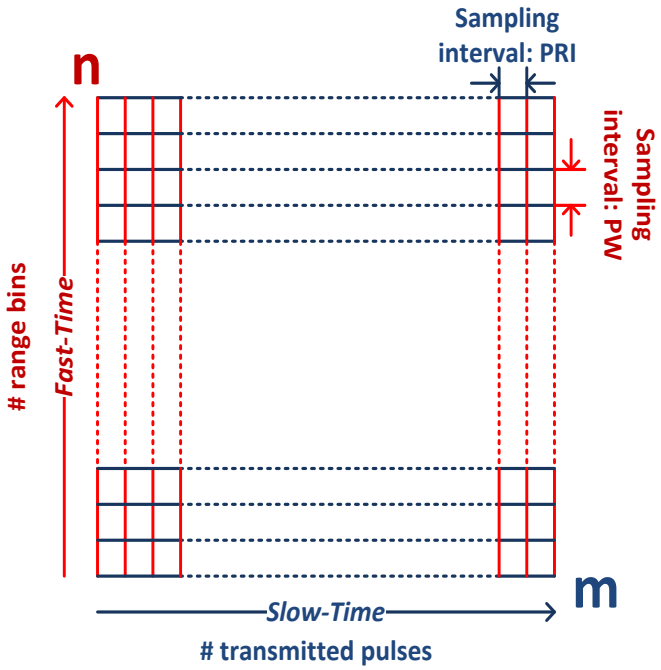

Figure 3.6: Radar data matrix in m x n dimensions [30].

CHAPTER 4

PROPOSED SEA CLUTTER MODEL

4.1 Introduction and Algorithmic Workflow

As mentioned in Chapter 1 “Introduction", the main motivation of this study is to model realistic sea clutter, that is, the simulated sea clutter model adapts itself on the scale of sea surface crests and troughs dynamically. For this purpose, experimental radar measurements at Overberg Test Range performed by CSIR [16] are selected as sample data. The key reason why these measurements are used in this study is that researchers at CSIR constructed complex radar data matrix based on their measurements. As complex data matrix has slow-time component (can be considered as real-time), the researchers reported RCS vs. time and range graphs (as in Figure 4.1-a), and power spectral density of clutter vs. time at specific range bin graphs (an example of which is shown in Figure 4.1-b). The proposed model for sea clutter mainly aims to incorporate the time-varying phenomena of sea surface to generate a simulated clutter that reasonably conforms with the measurements both in amplitude and frequency (Doppler) domain. After the construction of the model, it is desired to present results as in [16], that is, graphs of the proposed clutter model’s amplitude and Doppler shifts with respect to time and/or range can be compared with the displayed results in [16]. To obtain such time-varying clutter model, following work sequence is performed:

1. Realization of the sea surface,
2. Obtaining grazing angles on the generated sea surface and applying empirical sea clutter model,

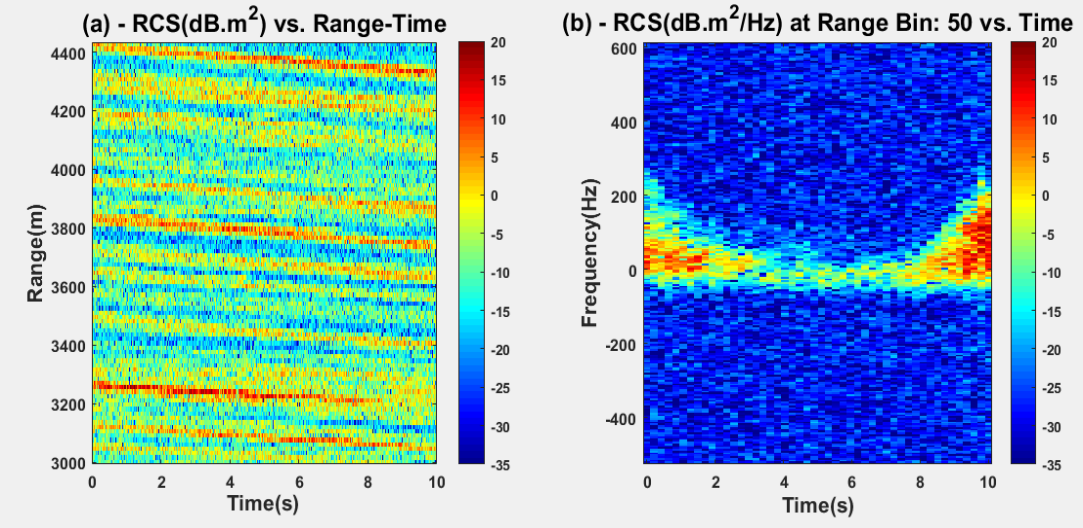

Figure 4.1: Graphs for CFA014 Data taken from [16], (a)- Amplitude of the clutter vs. range-time, (b)- Doppler frequency shift of the clutter w.r.t time at range bin: 50 (corresponds to the range of $3735\,\mathrm{m}$).

3. Determination of illuminated and shadow regions (visibility analysis) and applying required attenuation to the σ_0 values of shaded regions,

4. Composing clutter amplitudes of both illuminated and shadow regions,

5. Giving the Doppler spreads, based on obtained clutter amplitudes which is the variance of the resulting complex scattering parameter $\sqrt{\sigma_{VV}}e^{j\phi_{VV}}$,

Recall that step 1 is discussed in Chapter 2. Step 2 and step 3 are explained in the next section.

4.2 Clutter Amplitude Extraction from Sea Surface

In this section, calculation of grazing angle for the sea surface using the geometric optic assumption is explained. Then, application of the GIT model to the sea surface is discussed. And, finally, separation of illuminated and shadow regions is described, again based on the geometric optics assumption. Calculated clutter amplitudes are attenuated for shadow regions.

4.2.1 Grazing Angle Calculation and Applying GIT Model

With the assumption of geometric optics, radar is considered as a point source. Rays emanating from this source, are incident on the sea surface which is gridded. General scenario scene used for simulation of proposed model is illustrated in Figure 4.2, in which incident rays on sea surface grids can be seen.

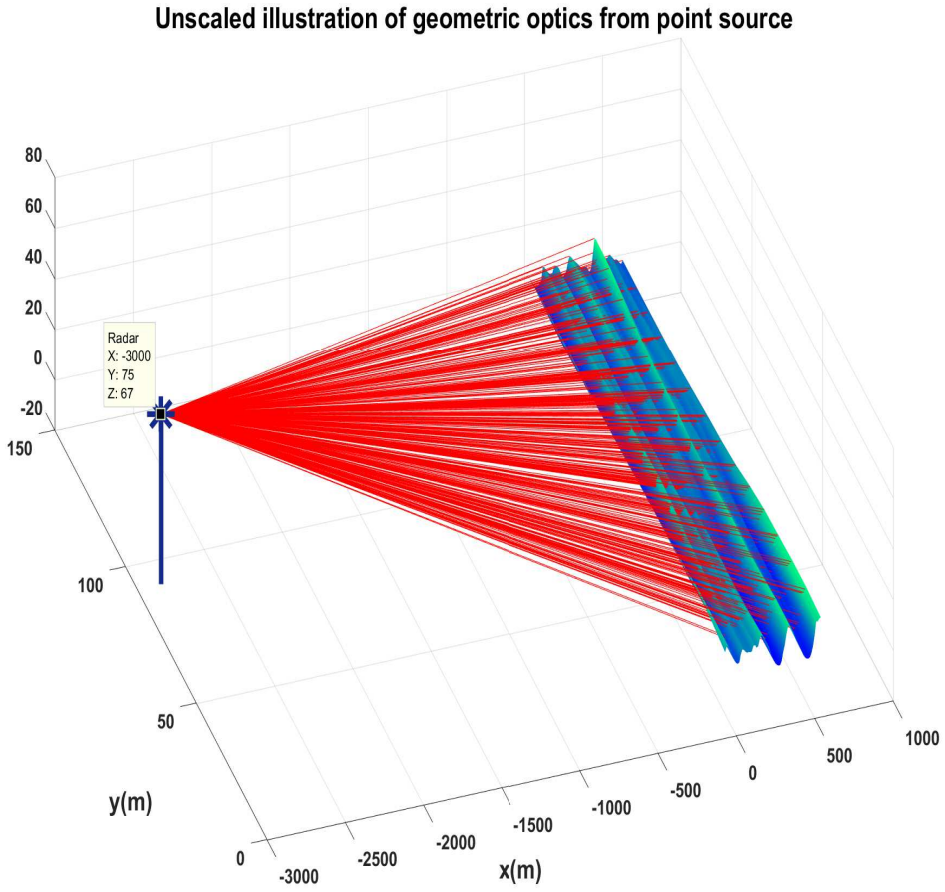

Figure 4.2: Sample scene of simulation and illustration of incident rays on sea surface.

To determine grazing angles, surface normals must be computed at first. Surface normals are computed for the patches illustrated in the top view part of Fig. 4.3 (as yellow dashed rectangles), whose centers are referred to vertices in this study. Thus, vertices are selected as sea surface grids. For the vertex $p_{m,n}$, where m and n are grid numbers in the x and y directions, respectively, unit surface normal is determined by

the cross product of grid edge vectors:

$$\vec{p}_{m+1,n} - \vec{p}_{m,n} = (p_{m+1,n}(x) - p_{m,n}(x))\hat{a}_x + (p_{m+1,n}(y) - p_{m,n}(y))\hat{a}_y + (p_{m+1,n}(z) - p_{m,n}(z))\hat{a}_z = \vec{A}, \tag{4.1}$$

$$\vec{p}_{m,n+1} - \vec{p}_{m,n} = (p_{m,n+1}(x) - p_{m,n}(x))\hat{a}_x + (p_{m,n+1}(y) - p_{m,n}(y))\hat{a}_y + (p_{m,n+1}(z) - p_{m,n}(z))\hat{a}_z = \vec{B}, \tag{4.2}$$

$$\hat{n}_{x,y,z} = \frac{\vec{A} \times \vec{B}}{|\vec{A} \times \vec{B}|} \tag{4.3}$$

where first vector $\vec{A}$ is a vector from point $p_{m,n}$ to next x–axis point $p_{m+1,n}$, while second vector $\vec{B}$ is a vector from point $p_{m,n}$ to next y–axis point $p_{m,n+1}$.

Similarly, unit vectors of incident rays for the each vertex is calculated by:

$$\vec{I}_{x,y,z} = \frac{\vec{p}_{m,n} - \vec{p}_{source}}{|\vec{p}_{m,n} - \vec{p}_{source}|} \tag{4.4}$$

where $\vec{p}_{source}$ is position vector of the radar. Surface normals and incident ray vectors are scaled with respect to sea surface grids and shown in Figure 4.3. Figure 4.3 shows that incident vectors are almost perpendicular to surface normals. This is expected for low grazing angles. To obtain grazing angles at each vertex, one requires to determine the angle between the incident ray and the surface normal at the point of incidence. This angle is the incidence angle and its complementary is the grazing angle. Incidence angle is obtained by:

$$\phi_i(x,y) = \arctan 2\left(\frac{||\vec{I}_{x,y,z} \times \hat{n}_{x,y,z}||}{\vec{I}_{x,y,z} \cdot \hat{n}_{x,y,z}}\right). \tag{4.5}$$

Then, grazing angle can be determined by:

$$\phi_{gr}(x,y) = 90^\circ - \phi_i(x,y) \tag{4.6}$$

Incidence angles larger than 90° occur from back faces of the sea surface crests for the up-wind condition. On the other hand, such incidence angles are due to the front faces of the sea surface crests for the down-wind condition. It is assumed that grazing angles smaller than 0.1° are rounded up to 0.1° (Recall that the value 0.1° is the minimum limit of which GIT model can be applied). However, before rounding up

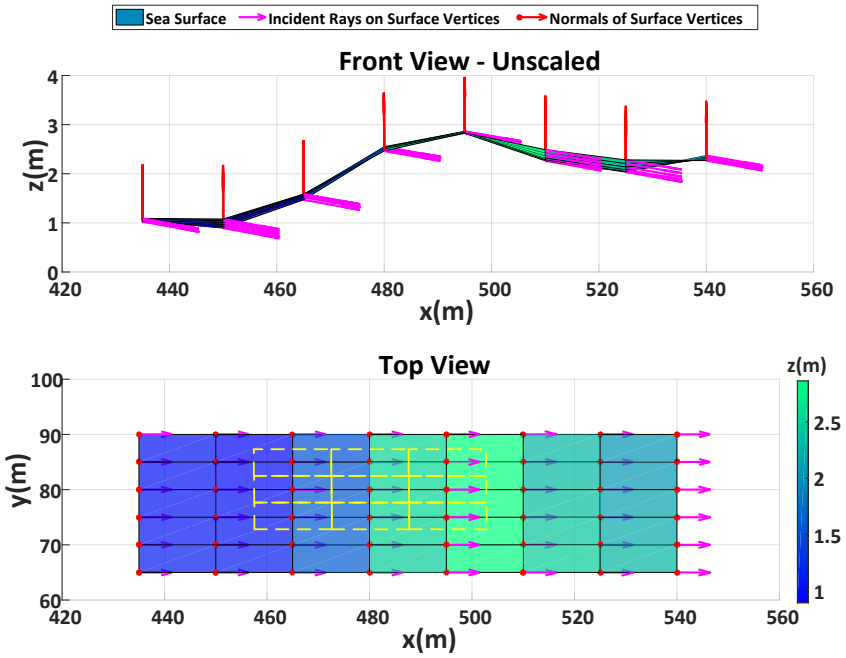

Figure 4.3: Surface normals and incident rays.

grazing angles lower than 0° to 0.1°, an attenuation function is created based on the grazing angles. The attenuation function (Fig. 4.4) is as follows:

$$\mathrm{ATT}(\phi_{gr}(x,y)) = \begin{cases} \tanh 1/\Gamma(0.2\phi_{gr}(x,y)) & \text{if} \quad \phi_{gr}(x,y) > 0 \\ 10^{-4} & \text{otherwise} \end{cases} \tag{4.7}$$

The function and its parameters are selected as in 4.7 to approximate the statistical amplitude models for sea clutter (see Chap. 5 for more details). Even though attenuation factor matrix is formed for all vertices, σ_0 values of non-visible vertices, which are determined by performing the visibility analysis (see Sec.4.2.2), are scaled by the assigned attenuation factors. The reason why we define the attenuation function in a such way can be understood with the following example. Assuming up-wind sea condition, consider two vertices that are non-visible: Let one vertex is on the back face of the sea surface, while the other is on the front face of the sea surface. Grazing angle of vertex on the back face is always negative, while the grazing angle of the other is always positive initially. The radar waves may be diffracted to the vertex on the front face regardless of being visible. Yet, such diffraction is not possible for the vertex on the back face. Therefore, vertices on front faces are less attenuated. The

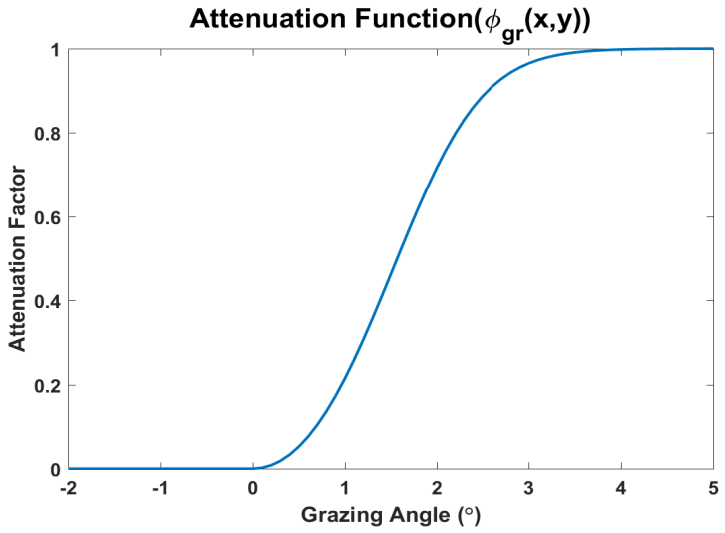

Figure 4.4: Attenuation function w.r.t. grazing angle

function also provides smooth transition that does not disrupt the continuity of modeled clutter returns. That is, while observing the returns from trough to crest or from back face to front face of the sea surface, RCS do not increase or decrease instantly. The application of this function as an attenuation matrix is investigated on Sec. 4.2.3 particularly.

Once the grazing angles are extracted from the generated sea, the GIT model can be used to determine the average surface reflectivity of sea surface patches. However, some modifications on the GIT model inputs should be made. The GIT model uses the wind speed and average wave height (h_{av}) that are related to the sea state as expressed in Eq. 3.5. Our goal is to employ the developed model for the non-oceanic waters also, which directly eliminates the fully developed sea assumption (for reasons given in Section 2.3), and the relations between wind speed, sea state and average wave height in Eq. 3.5 will not be true for such cases. In addition, sea state is not a fine measure to adjust other parameters since it can only take integer values. Therefore, we will use the SWH $H_{1/3}$ as input of the model instead of the sea state. The wind speed U and the average wave height h_{av} are then given by:

$$h_{av} = H_{1/3}/1.6, \tag{4.8}$$

$$U = 8.67 h_{av}^{0.4}. \tag{4.9}$$

Eq. 4.8 is mentioned in [2], while Eq. 4.9 is referred in [3]. In addition to these

modifications, wind direction term, used in Eq. 3.9, in GIT model is replaced with the wave direction since wind direction and wave direction may not match occasionally. Wave direction is used as input θ_w instead of wind direction.

With these modifications in the GIT model (will be referred to modified GIT from now on), average reflectivity of each patch represented by each vertex is determined by applying inputs SWH, θ_w, extracted grazing angles, and operational frequency to the modified GIT model. This done for each vertex regardless of that vertex being illuminated or not. If the vertex is not in direct line of sight from the radar, it is in the shadow region and attenuation due to shadowing should be included which is discussed in the next section.

4.2.2 Visibility Analysis

To determine if a vertex is illuminated or it is in the shadow region, viewshed analysis is applied. A viewshed is the area that is visible from a given location, and viewshed analysis is determination of the viewshed for the given observation location [36]. One can determine visibility of each vertex separately, as in Fig. 4.5. This can be done by the following steps:

1. Draw a line from point of observation to the vertex of interest (Let this point be P_{int} in Fig. 4.5).

2. Determine the slopes for virtual points where the line passes through (Green transparent dots in Fig. 4.5). This is done by interpolating slopes of nearest two vertices.

3. Check whether any of the calculated slopes on the drawn line is greater than the slope of the vertex of interest.

This basic method is called $R3$ algorithm. As this algorithm walks through all of the vertices to check visibility, it is computationally very slow. For this study, another viewshed algorithm is tested which is relatively faster than the $R3$ method.

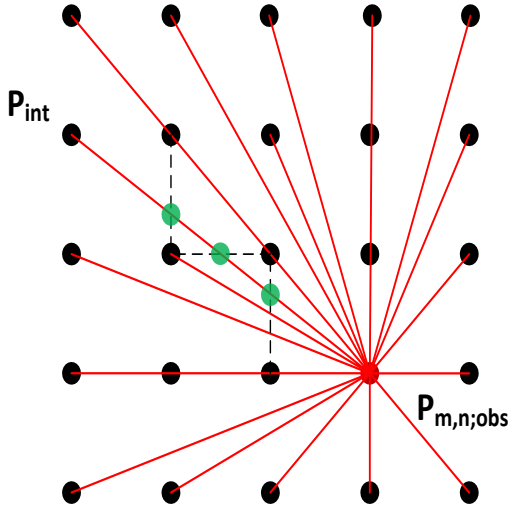

Figure 4.5: Schematic for $R3$ viewshed algorithm from observation point $P_{m,n}$.

4.2.2.1 X-Draw Algorithm

This method converts $R3$ algorithm's two-dimensional calculations into single dimension by using recursion. Algorithm splits vertices into layers that are nested rings. Layers get larger as they move further away from the observation point. Algorithm walks through each vertex on a layer, then move onto the next layer. Diagrams for X-Draw algorithm are presented in Fig. 4.6. X-Draw algorithm's process flow is as follows:

1. Initially set the accumulated slope to $-\infty$ at the observation point, $P_{m,n}$. Also, let this point to be origin, O.

2. Move to the first layer, slopes are accumulated and these slopes are set to be maximum before proceeding to the next layer. All vertices are visible for the first layer.

3. After moving to the second layer, consider vertex $P^{L2}_{m+1,n-2}$ as the point of interest, whose visibility depends on the maximum slopes of the lines joining from origin, O, to the nearest neighbor points ($P^{L1}_{m,n-1}$ and $P^{L1}_{m+1,n-1}$) in previous layer. The algorithm interpolates the maximum slopes of $\text{OP}^{L1}_{m,n-1}$ and $\text{OP}^{L1}_{m+1,n-1}$ (which are same as their own slopes) to calculate maximum slope

accumulated for vertex $OP^{L2}_{m+1,n-2}$ on the previous layer (first layer in this case). Call this slope as MS_{pi}, maximum accumulated slope for point of interest. If the slope of the line joining $P_{m,n}$ to $P^{L2}_{m+1,n-2}$, S_{pi} is greater than MS_{pi}, the vertex indexed $P^{L2}_{m+1,n-2}$ is visible. Also, for the next layer, MS_{pi} is set to be S_{pi}, which will be used for the calculations in the next layer. On the other hand, if MS_{pi} is greater than the S_{pi}, the point $P^{L2}_{m+1,n-2}$ is set to be invisible, and maximum slope for $OP^{L2}_{m+1,n-2}$ remains same (MS_{pi}).

4. This process is repeated until each point on each layer is inspected by the algorithm [37].

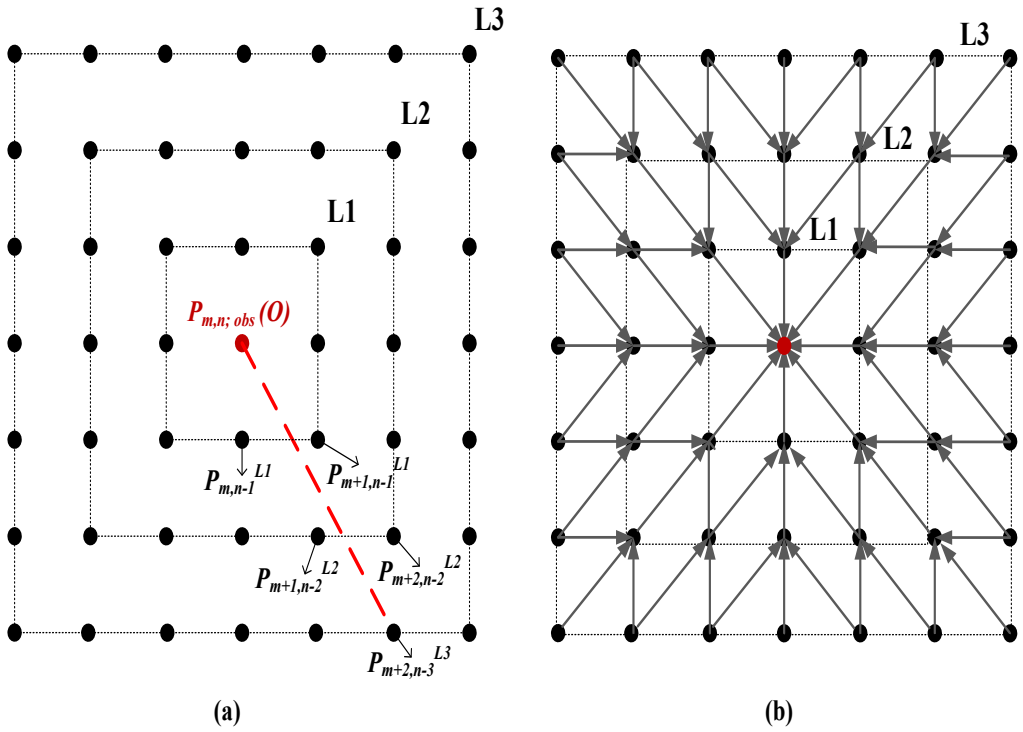

Figure 4.6: X-Draw algorithm diagram: (a)-Layers and dependency of sample vertex, (b)-Dependency flow in X-Draw

In X-Draw algorithm, each point on new layer depends on the nearest neighbors on previous layer. And since maximum slopes are accumulated for each layer, this implies preceding layers affect the visibility of vertices on succeeding layers. This dependency is illustrated in Fig. 4.6-b. To give an example for such dependency, con-

sider vertex $P^{L3}_{m+2,n-3}$ in Fig. 4.6-a. Line of sight from the observation point to the point $P^{L3}_{m+2,n-3}$ is determined by the slopes on red-dashed line. For the first layer, corresponding virtual interpolation line's slope MS_{L1i} is determined from the slopes of $\text{OP}^{L1}_{m,n-1}$ and $\text{OP}^{L1}_{m+1,n-1}$. For the second layer, MS_{L2i} is determined from the maximum slopes of $\text{OP}^{L2}_{m+1,n-2}$ and $\text{OP}^{L2}_{m+2,n-2}$. If MS_{L1i} is larger than MS_{L2i}, MS_{L2i} is updated as MS_{L1i}. Otherwise, MS_{L2i} remains same. If slope of $\text{OP}^{L3}_{m+2,n-3}$, is larger than MS_{L2i}, this point is set as visible. In the other case, it is set as invisible. This algorithm is less complex, and the problem can be handled as one dimensional case which makes it computationally very fast. However, the trade-off for speed is the accuracy [37]. It can be shown that the $R3$ algorithm has $O(N^3)$ complexity and is accurate but X-draw has $O(N^2)$ complexity and is approximate, as stated in the literature, [38].

As an example, a randomly generated sea surface is shown in Fig. 4.7-left. The observation point is located at ($-3000\,\text{m}$, $75\,\text{m}$ and $67\,\text{m}$) Cartesian coordinates. Illuminated and shadow regions for this scene are indicated in Fig. 4.7-right, where black regions are shaded, white regions are illuminated.

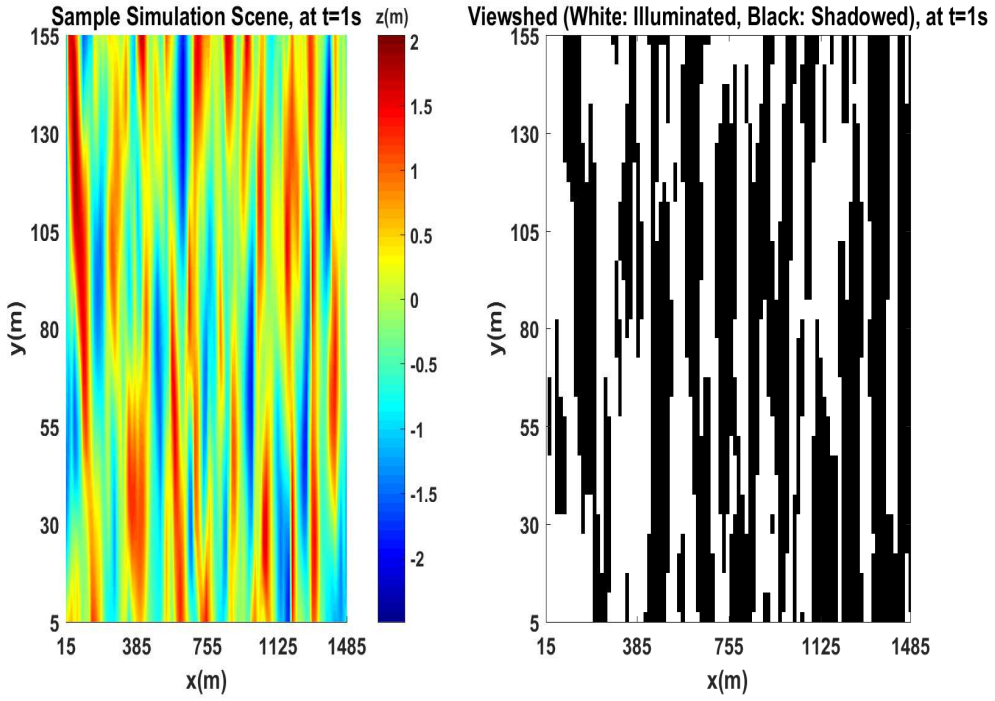

Figure 4.7: (Left) Top view of sample scenario sea surface, (Right) X-Draw viewshed visualization - white: illuminated region, black: shadow region.

4.2.3 Amplitudes of Illuminated and Shadow Regions

For the sample scene given in Fig. 4.2, where source is located at ($-3000\,\mathrm{m}$, $75\,\mathrm{m}$ and $67\,\mathrm{m}$) coordinates, angle coverage for all range bins is illustrated in Fig. 4.8. Although all vertices of the simulated sea surface area are traced with incident rays, due to angle resolution of the radar, σ_0 of vertices closer to the radar may be excluded during the calculation of RCS (uncovered areas in Fig. 4.8).

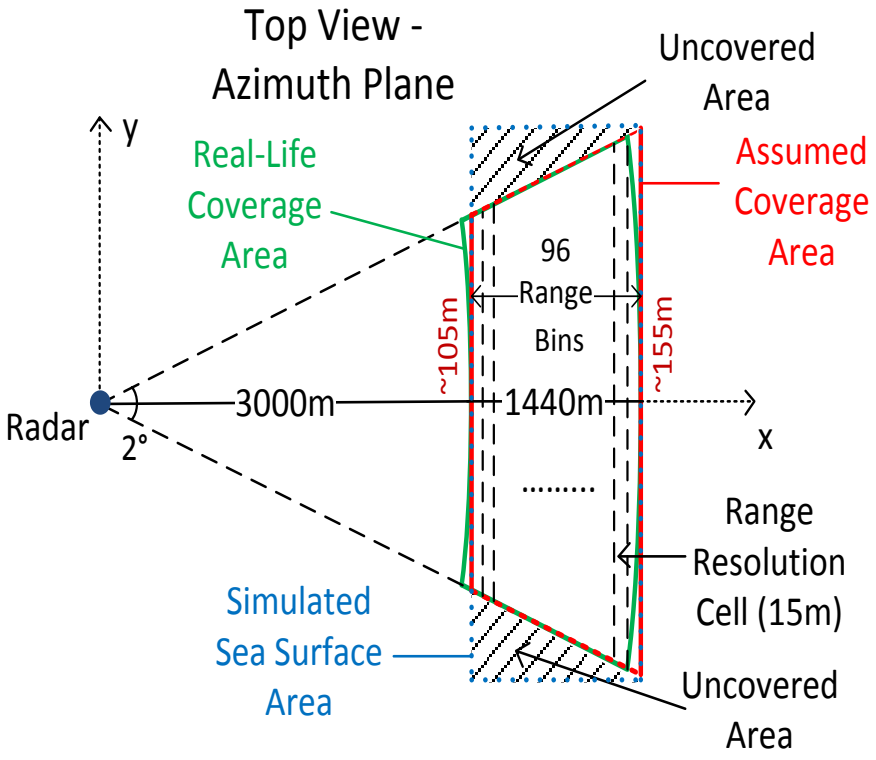

Figure 4.8: Comparison of real-life (black) and assumed (red) sea surface coverage of a radar.

Since the distance of the radar to the closest range of interest is 3 km as shown by the solid black arc in Fig. 4.8), the arc is almost linear. Therefore, in this study, sea scene is handled as a trapezoidal area. As a result of this, regular grids are employed instead of polar grids, which eases the computations.

In the simulations, the range resolution is chosen to be $15\,\mathrm{m}$, with a corresponding pulse width of $0.1\,\mu\mathrm{s}$. Hence, vertices are separated by $15\,\mathrm{m}$ from each other in range

direction which is assumed to be the x-axis in this study. Grids in y-axis are separated by $5\,\mathrm{m}$ from each other, but the number of grids within a resolution cell depends on the distance from the radar and the azimuth beamwidth of the radar.

The RCS of a radar resolution cell is computed as:

$$\begin{aligned}\mathrm{NRCS}(x,y,t) = \mathrm{GIT}(f,\phi_{gr}(x,y,t),\theta_w,\mathrm{SWH})\mathrm{vis}_{sea}(x,y,t)+\\ \mathrm{GIT}(f,\phi_{gr}(x,y,t),\theta_w,\mathrm{SWH})\mathrm{nonvis}_{sea}(x,y,t)\mathrm{ATT}(\phi_{gr}(x,y,t))\end{aligned} \tag{4.10}$$

$$\mathrm{RCS}(x,t) = \sum_{i=y_{ini(x)}}^{y_{fin(x)}} \mathrm{NRCS}(x,y_i,t)\mathrm{A}_{patch} \tag{4.11}$$

For Eq. 4.10, GIT function denotes applied modified GIT model at calculated grazing angles in a certain instant. Other parameters of this function is radar frequency, $\phi_{gr}(x,y)$, θ_w, and lastly given SWH. $\mathrm{vis}_{sea}(x,y,t)$ represents a two-dimensional visibility matrix of sea surface, while $\mathrm{nonvis}_{sea}(x,y,t)$ represents non-visibility matrix of sea surface in a certain time. These matrices are obtained by the mentioned viewshed algorithm and represent binary values according to the visibility of the patch of interest. $\mathrm{ATT}(\phi_{gr}(x,y,t))$ is the matrix of attenuation factors which are applied to the non-visible vertices. Recall that these factors vary according to the initial grazing angle value (before rounding up to 0.1°). For Eq. 4.11, A_{patch} corresponds to patch area and is the confined area of vertices determined by $(y_{i+1} - y_i)$(*Range Resolution*). All patch areas in a range bin form the radar resolution cell area. The number of patches to form the radar resolution cell area depends on the range. For example, 7 patches form radar resolution cell at the range of $3000\,\mathrm{m}$, while 11 patches form radar resolution cell at the range of $4440\,\mathrm{m}$. $\mathrm{NRCS}(x,y,t)$ is the computed σ_0 over both illuminated and shadow regions. Summation starting point $y_{ini}(x)$ and ending point $y_{fin}(x)$ represent trapezoidal starting and ending grid points, that depend on x (range bin).

For upwind condition, sample extracted initial RCS matrix in range and time domain is given in Fig. 4.9.

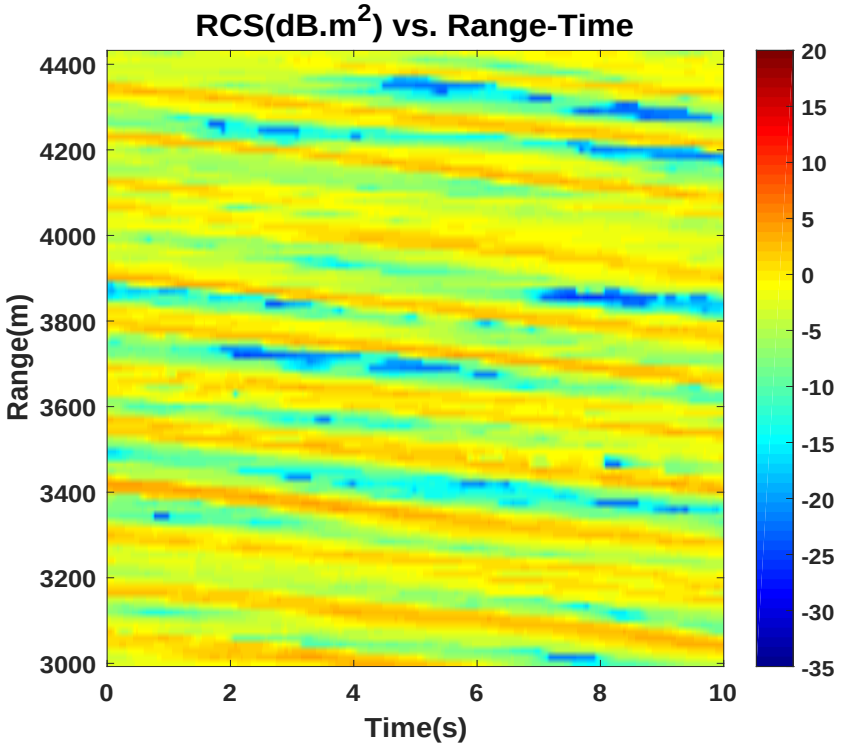

Figure 4.9: Result of initial RCS extraction in range and time domain.

4.3 Doppler Modeling of Extracted Clutter Amplitudes

In Sec. 4.2, calculation of the 2D RCS(x, t) in both time and range domain is discussed. The time step of computed 2D RCS(x, t), namely the initial RCS variance matrix, is set by the time step of generated sea surface's motion. Sea surface motion duration step is limited by WAFO toolbox. However, since the sea surface changes very slowly with respect to radar PRF (pulse repetition frequency), the time step used in these calculations is rather large, but small enough to reveal any changes on the sea surface. In addition, applying the calculations mentioned on the previous sections to the sea surface having motion with duration step size of PRI is computationally expensive. Yet, our aim is to simulate the clutter return for a radar; therefore, we need the variation of the RCS with a step size of PRI. We choose the PRI as $200\,\mu$s to compare our results with the data in [16]. For this purpose, we interpolate the RCS obtained in time. The selected interpolation method is the piecewise cubic interpolation that preserves the shape of RCS against time curve.

After this interpolation, phases are added, which result in observable Doppler shifts

on the frequency spectrum, in relation to the mechanisms mentioned in Chap. 3 - Sec. 3.3. Added phases should be correlated in time to obtain realistic Doppler spectra for sea clutter. Thus, first mean Doppler parameters like peak frequencies and bandwidths are obtained. Then, by using Fourier Synthesis method generation of correlated random phases is realized.

4.3.1 Mean Doppler Parameters of the Model

Recall that HH and cross polarization components are not covered in this work. The main reasons for that are lack of experimental data for HH and cross polarizations, simplifying scattering mechanism terms for Doppler shifts, and not to extend the presented analysis results in this study. So, only VV polarization is discussed and examined. Since sea spike scattering mechanism is not significant for VV polarization, only Bragg and whitecaps scattering mechanisms are considered for Doppler structure of data matrix. Walker [12] assigns Gaussian distribution for each mechanism as follows:

$$S_B(f) = P_B \exp\left(-\frac{(f - f_B)^2}{W_B^2}\right), \tag{4.12}$$

$$S_W(f) = P_W \exp\left(-\frac{(f - f_W)^2}{W_W^2}\right) \tag{4.13}$$

in which, subscripts B and W denote Bragg and whitecap components respectively. While f refers to the Doppler frequency domain, f_B and f_W are Doppler frequencies corresponding to the phase velocity of Bragg and whitecap mechanisms. W_B and W_W are Doppler bandwidth of the mechanisms, whereas P_B and P_W are the spectral amplitudes of mechanisms. In study [13], these two spectral components merge into total vertical polarization spectrum density as:

$$S_\Psi(f) = S_B(f) + S_W(f). \tag{4.14}$$

Whitrow [14] constructs a Doppler model, to which Doppler parameters of the proposed model mainly adhere, based on Walker's argument given in Equations 4.12, 4.13 and 4.14. For constructed Doppler model in [14], Bragg component generally controls peak and width of the Doppler spectra for vertical polarization. Whitrow [14] scales peak frequencies and bandwidths of Gaussian spectrum, $\Psi_V(f)$, using graphical results of Rozenberg's [15] wave tank measurements as follows:

- Fitting Bragg spectrum's peak frequency,
  - For upwind direction:

$$f_B^u = (17.36 + 10.59U^{0.29} + 0.0153U^{3.05})0.021/\lambda_{radar}, \tag{4.15}$$

  - For downwind direction:

$$f_B^d = (22.83 + 2.84U)0.021\lambda_{radar}, \tag{4.16}$$

  where λ_{radar} refers to operating wavelength of the radar, and superscripts u and d represents upwind and downwind directions. To give angular dependency on the Doppler shift, Eq. 4.15 and Eq. 4.16 may be combined as:

$$f_{B0} = \begin{cases} f_B^u \cos\theta_w, & \text{for} \quad 0 \leq \theta_w \leq \pi/2 \\ f_B^d \cos\theta_w, & \text{for} \quad \pi/2 \leq \theta_w \leq \pi \end{cases} \tag{4.17}$$

  In this expression, θ_w refers to the angle between radar look direction and sea wave direction.

- Fitting whitecap spectrum's peak Doppler shift,
  - For upwind direction:

$$f_W^u = (-39.43 + 57.48\sqrt{U} - 5.69U)0.021/\lambda_{radar}. \tag{4.18}$$

  - For downwind direction:

$$f_W^d = (22.83 + 2.84U)0.021/\lambda_{radar}. \tag{4.19}$$

  Similar to the case in Bragg mechanism,

$$f_{W0} = \begin{cases} f_W^u \cos\theta_w, & \text{for} \quad 0 \leq \theta_w \leq \pi/2 \\ f_W^d \cos\theta_w, & \text{for} \quad \pi/2 \leq \theta_w \leq \pi \end{cases} \tag{4.20}$$

- Fitting Bragg spectrum's Doppler bandwidth,
  - For upwind direction:

$$W_B^u = 5.28U. \tag{4.21}$$

  - For downwind direction:

$$W_B^d = 3.92U. \tag{4.22}$$

Merging these results by a sinusoidal transition yields:

$$\begin{aligned} W_{B0} &= \frac{W_B^u + W_B^d}{2} + \frac{W_B^u - W_B^d}{2} \cos\theta_w \\ &= (4.6 + 0.68U\cos\theta_w)0.021/\lambda_{radar}. \end{aligned} \tag{4.23}$$

- Fitting whitecap spectrum's Doppler bandwidth,
  - For upwind direction:

$$W_W^u = \begin{cases} 6.15U, & \text{for} \quad U < 5.97 \\ 36.7, & \text{for} \quad U > 5.97 \end{cases} \tag{4.24}$$

  - For downwind direction:

$$W_W^d = 3.92U. \tag{4.25}$$

  Combining above results in a smooth transition with angle gives:

$$W_{W0} = \begin{cases} (5.035 + 1.115\cos\theta_w)U0.021/\lambda_{rad}, & U < 5.97 \\ (18.35 + 1.96U + (18.35 - 1.96U)\cos\theta_w)0.021/\lambda_{rad}, & U > 5.97 \end{cases} \tag{4.26}$$

Whitrow [14] further modifies this wave tank parameters, because spectral data seems to have larger frequency shifts in open seas. Factors to modify are:

- Bragg peak frequency, f_{B0} factor - 1.3,
- Whitecap peak frequency, f_{W0} factor - 2.7 for upwind, and 2.3 for downwind,

Observed bandwidths from experimental data are also much lower than the findings in [14] because the environment where experiments were conducted is coastal waters. Therefore, bandwidths are scaled in this work as follows:

- Bragg bandwidth, W_{B0} factor - 0.55,
- Whitecap bandwidth, W_{W0} factor - 0.9.

Given peak frequencies of whitecap scattering almost always larger than the peak frequencies of Bragg mechanism. Furthermore, these frequencies are stable for given

wind speed, relative radar look angle θ_w, and operational radar wavelength [14]. That is, instantaneous deviations on sea surface wave heights do not affect Doppler frequencies. However, strong correlation between peak Doppler frequency and intensity of clutter returns is observed for some experimental data in [16]. Normalized clutter intensity and estimated peak frequencies for CFA002 data of [16] are given in Fig. 4.10 to show the mentioned correlation. It is assumed that maximum clutter return

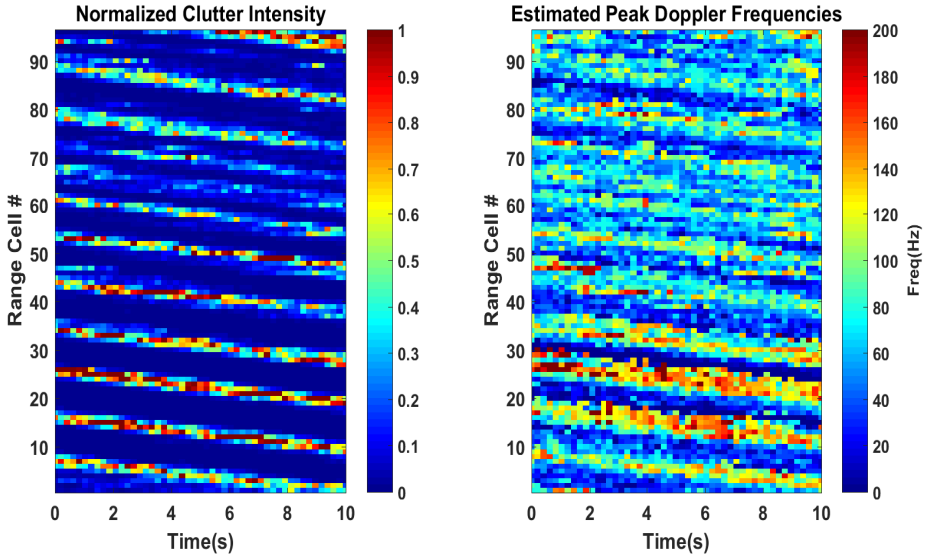

Figure 4.10: Correlation between normalized clutter return (left) and estimated peak Doppler frequencies (right).

occurs at peak frequencies in this study. In [17], a formula that relates the mean frequencies to the clutter return is given as:

$$f_m(x_n) = A + Bx_n + r \tag{4.27}$$

where x_n is the normalized local clutter return, A and B are constants, and r is a Gaussian random variable with zero mean and standard deviation, σ_r. For the proposed model, peak frequencies of Bragg and whitecap mechanisms are separately handled by using the initial frequency parameters f_{B0} and f_{W0} as:

$$f_B = A_B f_{B0} + (1 - A_B) f_{B0} x_n |\cos\theta_w| + r_B, \tag{4.28}$$

$$f_W = A_W f_{W0} + (1 - A_W) f_{W0} x_n |\cos\theta_w| + r_W \tag{4.29}$$

where x_n is the ratio of the local clutter return to the mean clutter return. The local clutter return is calculated by averaging the return for a given range cell over a small

time window [17]. r_B and r_W are the added zero mean Gaussian random variables. The parameters are selected to get a rough resemblance between the simulation results and CSIR data [16]:

$$A_B = 0.25, \quad A_W = 0.45, \tag{4.30}$$

$$\sigma_{r_B} = 2, \quad \sigma_{r_W} = 3. \tag{4.31}$$

On the other hand, Doppler bandwidth is independent from the clutter intensity. Therefore, only Gaussian random variance with zero mean and standard deviation of $\%5$ of W_{B0} is added to the Bragg component's bandwidth. No change is made on whitecap bandwidth.

In addition to the frequency and bandwidth Doppler parameters, relation between Bragg spectra amplitude, P_B, and whitecap spectra amplitude, P_W is given as [14]:

$$\left.\frac{P_W}{P_B}\right|_{\theta_w} = 0.437\frac{U}{10}\left(\frac{1+\cos\theta_w}{2}\right) + 0.0417\frac{U}{7}\left(\frac{1-\cos\theta_w}{2}\right). \tag{4.32}$$

This relation holds in general; however, if one examines the experimental results of [16], it can be seen in Fig. 4.11 that spectral amplitudes of whitecaps may exceed the Bragg ones. In Fig. 4.11 blue line represents normalized mean Doppler spectra,$S(f)$, for all range bins, red dashed line represents normalized mean Doppler spectra for range bin 27. Therefore, P_B to P_W ratio given in 4.32 should be randomized. Ratio in 4.32 is called as $[P_W/P_B]_0$ and considered as an initial value. For the proposed model, $[P_W/P_B]_{Rayl}$ ratio has been designated as Rayleigh distributed random variables with the scale parameter of $1.2 \times [P_W/P_B]_0$ to approximate our results to the empirical results in [16]. The distribution of $[P_W/P_B]_{Rayl}$ ratio is shown in Fig. 4.12.

4.3.2 Generation of Correlated Doppler Shifts

Since the proposed model's aim is to generate complex random variables, $\sqrt{\sigma_{VV}}e^{j\phi_{VV}}$, correlated phases for given amplitude (variance), σ_{VV}, is achieved by employing Fourier synthesis method in [1]. Fundamentally, the method is application of a filter, whose response is determined by the desired spectral power density. Relation between power spectra of the input and output processes is given as:

$$S_\Psi(f) = |H(f)|^2 S_{G_{wn}}(f) \tag{4.33}$$

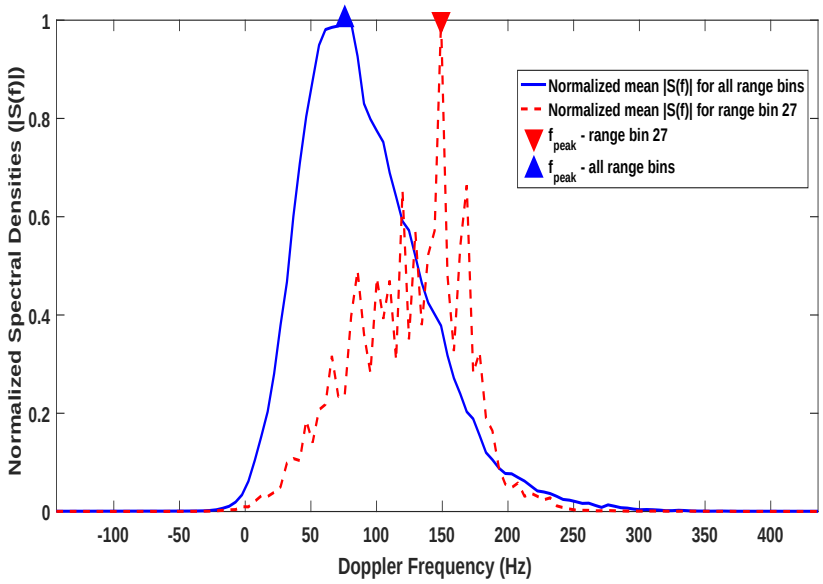

Figure 4.11: Peak frequency comparison: mean Doppler spectra of all range cells against mean Doppler spectra of range bin: 27 for the experimental CFA002 data [16]

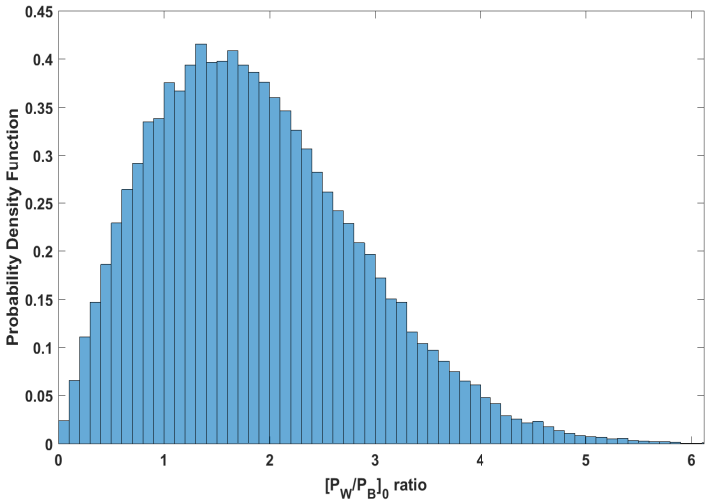

Figure 4.12: Histogram of $[P_W/P_B]_{Rayl}$ w.r.t. $[P_W/P_B]_0$.

for which, filter response is selected as the square root of the desired output response, $|H(f)| = \sqrt{S_\Psi(f)}$. Since the input is white Gaussian noise its power spectral density is flat and is set to unity to obtain desired output response.

By Fourier inversion, desired complex parameter is in the form of:

$$\psi(t) = \sum_{i=1}^{N_f} \alpha(f_i) \widetilde{g}_{wn_i} e^{-j2\pi f_i t} \tag{4.34}$$

where $\alpha(f_i)$ represents Fourier series coefficient of $\psi(t)$, and $\widetilde{g}_{wn_i}$ is complex Gaussian having unity variance. $f_i = \Delta f i$ is the discrete frequency whose domain is defined in $[-\text{PRF}/2, \text{PRF}/2]$. PRF is defined as $1/\text{PRI}$. PRF is chosen to be $5\,\text{kHz}$ in the simulations, as in [16]. Superscript N_f refers to the length of observation window in time whose steps, i, is in PRI. The observation duration, $t_{obs} = \text{PRI} \times N_f$, can be accepted as the time interval for which Doppler characteristics of sea surface is considered as stationary. To be specific, $\psi(t)$ is the complex data for certain time observation window, t_{obs}. Collecting and sequencing $\psi(t)$ values successively from window to window, result in a complex data vector for a single range bin. That is, obtained complex vector corresponds to a single row in the complex data matrix. Expression of $\alpha(f_i)$ in terms of desired output spectra is given later in this section.

Recall that desired spectra is the bimodal Doppler spectra given in Eq. 4.14. By integrating the desired spectra over all frequencies, one obtains [14]:

$$P_T = \int_{-\infty}^{\infty} S_\Psi(f) df = P_B W_B \sqrt{\pi} + P_W W_W \sqrt{\pi} = \sigma_{VV}. \tag{4.35}$$

Being determined in 4.2, σ_{VV} is the RCS magnitude for a single range bin, which is also total power, P_T, for that range bin. Hence, one can determine Bragg amplitude parameter, P_B:

$$P_B = \frac{\sigma_{VV}}{\sqrt{\pi}\left(W_B + W_W \dfrac{P_W}{P_B}\right)} \tag{4.36}$$

by injecting the defined $[P_W/P_B]_{Rayl}$ into $\dfrac{P_W}{P_B}$. Then, again using the same relation whitecap amplitude, P_W can be decided.

After determining all parameters, consider the basic relation between autocorrelation

function and power spectral density:

$$P_T = \int_{-\infty}^{\infty} S_\Psi(f)df = \mathbf{E}(\psi(t)\psi(t)^*). \tag{4.37}$$

Therefore, autocorrelation of desired complex parameter, $\mathbf{R}_\psi(0)$, equals to the extracted clutter RCS of single range bin, σ_{VV}. This relation is used for all range bins in the computation of complex data matrix. To ensure conservation of average power, $\alpha(f_i)$ coefficients are determined by using relations in Eq. 4.35 and Eq. 4.37. To determine $\alpha(f_i)$, following steps are carried:

$$\mathbf{E}(\psi(t)\psi(t)^*) = \mathbf{E}\left(\left[\sum_{i=1}^{N_f}\alpha(f_i)\widetilde{g}_{wn_i}e^{-j2\pi f_i}\right]\times\left[\sum_{k=1}^{N_f}\alpha^*(f_k)\widetilde{g}^*_{wn_k}e^{j2\pi f_k}\right]\right) \tag{4.38}$$

$$= \mathbf{E}\left(\sum_{i=1}^{N_f}|\alpha(f_i)|^2|\widetilde{g}_{wn_i}|^2\right) = \sum_{i=1}^{N_f}|\alpha(f_i)|^2|\widetilde{g}_{wn_i}|^2. \tag{4.39}$$

Due to having unity magnitude, $|\widetilde{g}_{wn_i}|^2$ equals to 1. Thus, Eq.4.39 results in:

$$\sum_{i=1}^{N_f}|\alpha(f_i)|^2 = \sigma_{VV} = \int_{-\infty}^{\infty} S_\Psi(f)df. \tag{4.40}$$

Multiplying both sides with Δf, which is defined as $f_{i+1} - f_i$:

$$\sum_{i=1}^{N_f}|\alpha(f_i)|^2\Delta f \simeq \Delta f\int_{-\infty}^{\infty} S_\Psi(f)df. \tag{4.41}$$

For each window in time, sized N_f, assuming ***Riemann sum*** holds as integral (and notice that frequencies above $\text{PRF}/2$ and below $-\text{PRF}/2$ yield 0 spectral amplitude):

$$\int_{-\infty}^{\infty}|\alpha(f_i)|^2df = \Delta f\int_{-\infty}^{\infty} S_\Psi(f)df. \tag{4.42}$$

Hence, the coefficient $\alpha(f_i)$ can be written in the form of:

$$\alpha(f_i) = \sqrt{\Delta f S_\Psi(f_i)}. \tag{4.43}$$

Recall that frequency domain $[-\text{PRF}/2, \text{PRF}/2]$ is divided into N_f intervals. Therefore, discrete frequency difference Δf equals to PRF/N_f. As a result of these findings,

$$\alpha(i) = \sqrt{S_\Psi\left(\frac{i\text{PRF}}{N_f}\right)\frac{\text{PRF}}{N_f}}. \tag{4.44}$$

So obtained complex vector, which has not been declared as complex data row vector of complex data matrix, $\psi(t)$ is:

$$\psi(t) = \sum_{i=1}^{N_f} \sqrt{S_\Psi\left(\frac{i\text{PRF}}{N_f}\right)\frac{\text{PRF}}{N_f}}\widetilde{g}_{wn_i}e^{-j2\pi f_i t}. \tag{4.45}$$

Sweeping N_f length window over time and concatenating obtained $\psi(t)$ to each other results in a complex data vector for the interested range bin.

After performing these processes, 100 Monte Carlo iterations are realized to observe whether average power of modeled complex vectors approximates to the RCS value. In Figure 4.13, this conservation of power can be observed. Blue lines represent power of each Monte Carlo realization. By averaging them, one can show there is small discrepancy between average power and windowed RCS, σ_{VV}, for which window size N_f is 1024.

The mentioned procedures are applied to all range bins in order to complete complex data matrix. For the upwind condition, proposed Doppler spread is illustrated in Fig. 4.14 as a time-Doppler plot.

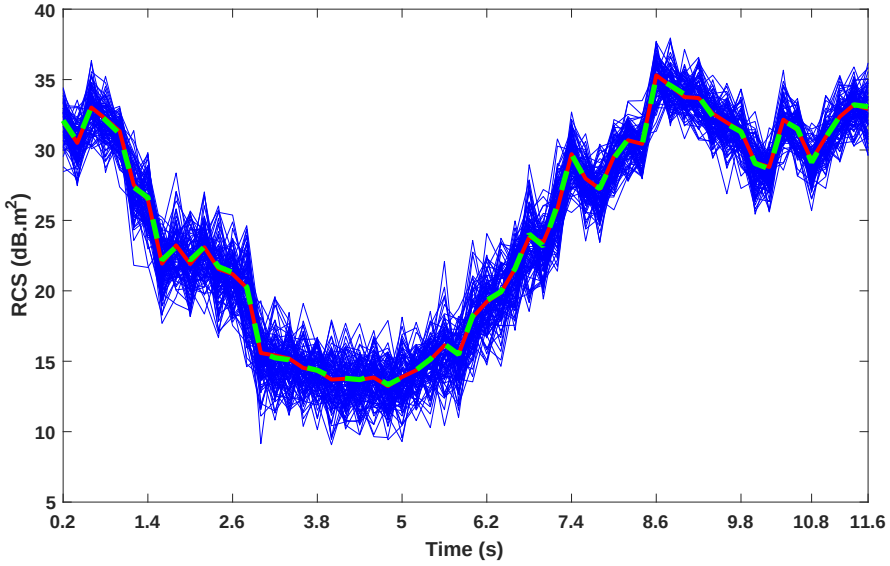

Figure 4.13: Conservation of average power, as green dashed line refers to average RCS values of 100 iterations, while red line refers to initially extracted σ_{VV} values.

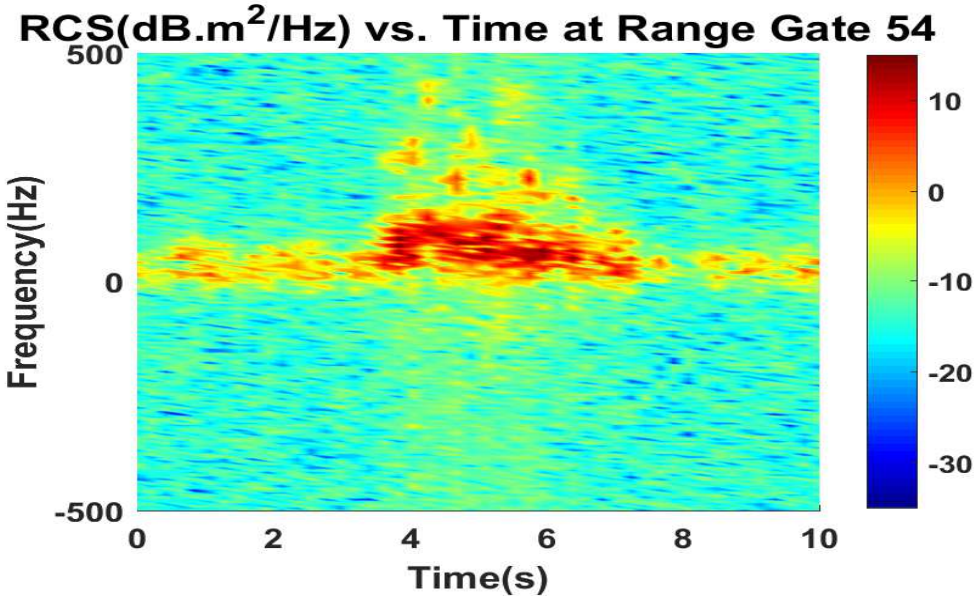

Figure 4.14: Time vs. Doppler result of the proposed model at range gate 54 (corresponds to the range of $3810\,\mathrm{m}$).

4.4 Discussion on the Limitations of the Proposed Model and Some Considerations

As almost all of the models for the sea clutter has some constraints, the proposed model has the following limitations some of which arise from the limits of underlying models (see Section 3.2.2 for more detail):

- The modified GIT model fails to give appropriate results for sea states lower than 3 [6], and sea states higher than 6 [39].
- The proposed model is valid for grazing angles between 0.1° and 10° which is again limited by the used modified GIT model [14].
- The radar frequency range of the proposed model is $1\,\mathrm{GHz}$ to $10\,\mathrm{GHz}$ again limited by the GIT model [14].
- The patches used to calculate the RCS of the generated sea surface must be small enough to observe variations on the sea surface, that is, the edge length of a patch must be at least five times smaller than the wavelength of the generated sea waves [9, 40]. In this study, we have examined our model with a patch size

of $5\,\mathrm{m} \times 15\,\mathrm{m}$ for sea wave wavelength of approximately $105\,\mathrm{m}$ (corresponding SS is 5). This patch size is appropriate to observe the changes on sea surface for SS 5. The main reason is to mimic the conditions given in [16], since we compare the simulation results of the proposed model with the experimental data in Chapter 5. The environmental conditions and radar parameters are given in the scenarios mentioned on the next chapter. Our model is limited to sea states above 3 by the GIT model, which corresponds to sea wave wavelength of approximately $30\,\mathrm{m}$. Therefore, patch dimensions smaller than $5\,\mathrm{m} \times 5\,\mathrm{m}$ should never be necessary. Smaller patch size can be selected for lower sea states, as long as limitations of WAFO toolboxes [18, 19] are not exceeded.

- Dimension of the sea surface patches must not exceed radar resolution cell dimensions, not to obtain same amplitude (texture) for adjacent range bins. In this study, we have assumed radar uses $0.1\,\mu\mathrm{s}$ pulse width which corresponds to $15\,\mathrm{m}$ range resolution; thus, selected sea patch dimensions are eligible for the study.

In this study, we have not covered HH, HV and VH polarizations. Although GIT model provides σ_{HH} parameter as a function of environmental parameters, it does not give the cross polarization parameters. The reasons why we did not implement HH polarization case can be listed as follows:

- Experimental data in [16], used to compare our results with, does not contain any results for HH polarization.
- Simplifying the proposed model by discarding the sea spike scattering term from Walker's Doppler spectra model [13] in Eq. 4.14.
- To shorten the scope of the analysis results presented in Chapter 5.

The mentioned reasons do not pose any obstacle to construct the model for HH polarization and analyze the results. They are mainly due to narrow down the scope of the study.

CHAPTER 5

SIMULATION RESULTS

In this chapter, simulation results are presented based on the calculations and assumptions made for the proposed model. First of all, the RCS values of the proposed model and experimental data of [16] are given in range-time graphs. NRCS, σ_0 statistics for both simulation results and experimental datasets are investigated via normalized histograms. Then, we attempt to fit statistical amplitude distributions that characterize sea clutter to the resulting normalized histograms. Secondly, by using spectrogram (see Appendix A), time-Doppler graphs of resulting complex data matrices are examined. Then, mean spectra of the simulation results and available data are examined and compared with the ones mentioned in the literature. Finally, dispersion relation of sea surfaces are analyzed through the clutter amplitudes of both proposed model and experiment data in [16].

Before proceeding the results, the simulation scenarios must be introduced. There are four scenarios to be simulated. Two of these scenarios (scenario 1 and 2) are emulated from the CSIR's field experiments [16]. Results of these two scenarios are compared through the presented graphs and histograms. On the other hand, due to lack of experimental data, last two scenarios are not compared with any empirical result. Basic assumptions and parameters (almost all of them considered as same with the parameters in [16]) for all four scenarios are as follows:

- Starting point of the generated sea surface for each scenario is taken as the reference coordinate $(0\,\mathrm{m}, 0\,\mathrm{m})$.

- Radar location in all the scenarios is fixed and is chosen to be $(-3000\,\mathrm{m}, 75\,\mathrm{m})$,

which is referenced to the starting point of the generated sea surface. Also, they are placed at the height of $67\,\mathrm{m}$.

- All sea surfaces is generated with SWH, $H_{1/3}$ =$3.4\,\mathrm{m}$ as in [16], and peak period T_p =$9\,\mathrm{s}$. Given value for the peak period is also an approximation to the observed T_p from the results of [16]. Sea depth is assumed to be $30\,\mathrm{m}$, as experiments in [16] mostly surveyed at coastal waters. Front-back asymmetry ratio is selected as $l_\alpha = 0.5$, not to obtain sinusoidal shaped sea surfaces.
- Generated sea surfaces extend in range (on x-axis) of $1440\,\mathrm{m}$. Extension of the surfaces in y-dimension is about $165\,\mathrm{m}$.
- Radar look direction is 0°, that is, radar boresight is on the x-axis.
- Transmitted radar pulses are at $6.9\,\mathrm{GHz}$ frequency.
- PRI value for the pulses is taken as $200\,\mu\mathrm{s}$. Thus, PRF is $5\,\mathrm{kHz}$.
- PW of the pulses is $0.1\,\mu\mathrm{s}$. Hence, range resolution is $15\,\mathrm{m}$.
- Azimuth beamwidth, θ_{AZBW}, is 2°
- Observation window duration t_{obs} is assumed as $0.2\,\mathrm{s}$, that gives window length, $N_f = 1000$ for $200\,\mu\mathrm{s}$ PRI value.
- Wind speed, U, is not given in the scenarios, since for the proposed model U is determined from the given SWH.

Only parameter that distinguishes the four scenarios is the supplementary angle of the difference between radar look direction and the angular direction of sea waves, which has already been denoted as θ_w. This difference is achieved by the generation of sea waves in distinct directions. The simulation scenarios with respect to θ_w values are presented in Table 5.1.

For scenarios 1 and 2, there are available few experimental data; however, one should remind that large amount of data is needed to make fair comparison while working with random processes. Unfortunately, no experimental data is found for the scenarios 3 and 4. Scenario for crosswind condition, where θ_w equals to 90°, is not examined since amplitude of the sea clutter may not be distinguished from the noise floor.

Table5.1: Simulation scenarios and conditions.

Scenario #	θ_w **in** $^\circ$	**Condition**
Scenario 1	2	Upwind
Scenario 2	42	Upwind-Crosswind
Scenario 3	80	Nearly Crosswind
Scenario 4	179	Downwind

5.1 Simulation Results for Clutter Amplitudes

After modeling the Doppler shifts by the proposed sea clutter model mentioned in Chapter 4, magnitude of the complex data matrix can be represented as distribution of RCS, σ_{VV}, in both range and time. Scenarios 1 and 2 are compared with the experimental datasets of [16] in range-time domain, as amplitude distributions of simulation result and empirical data for a given scenario are quite similar. Scenario 3 and 4 cannot be validated due to lack of experimental data. In addition, resulting RCS matrices are further used in section 5.3 to ensure that dispersion relation holds for our simulation.

Along with the RCS plots, NRCS σ_0 values of simulation results for each scenario and available experimental datasets are also examined through the normalized histograms. The histograms shown in this section are normalized with respect to the *probability density functions (pdf)* of data so that the sum of histogram values multiplied by histogram bin size is unity. NRCS values are also normalized for histogram plots, by dividing them to the mean of the used samples, which corresponds to $\sigma_0/\overline{\sigma_0}$. Statistical amplitude distributions of *Log-Normal*, *Gamma* and *Weibull* distributions are fitted for each normalized histogram as these distributions provide a good fit for σ_0 values mostly. On the other hand, *K-distribution* which is commonly accepted as having the best fitting *pdf* for the sea clutter amplitude statistics, is held out of the scope of this study. This is because envelope of the K-distribution is given by the texture component (see Appendix B), and considering the observation times in the resulting RCS matrices, Gamma distribution is sufficient to statistically model the amplitude of the generated sea clutter. In addition, the Gamma distribution is less complex than the K-distribution. The parameters of fitted distributions are estimated

via *Maximum Likelihood Estimates (MLE)* method. Distribution that fits best to the given NRCS samples is determined by the comparison of the Log-likelihood (LL) parameters. This parameter gives an intuition that fitted distribution having highest LL value for given data samples provides best fit with respect to other fitted distributions [41, 42]. We have utilized the Statistics Toolbox of MATLAB^{TM} to determine this parameter for each distribution given. Finally, we check the similarities of the fitted distributions to the results for both data and model by applying the Symmetrized Kullback-Leibler (SKL) divergence method.

5.1.1 Range vs. Time Result for Scenario 1

The scenario is emulated from the CFA16-002 experimental dataset of CSIR [16]. One can notice the similarity between RCS matrix of the proposed model for scenario 1, shown in Fig. 5.1, and RCS matrix of the experimental data, shown in Fig.5.2. One can estimate the wave direction from the graphs given below. High amplitudes occur mostly due to the crest faces that look towards radar (upwind). As these high amplitudes appear moving from further range bin to closer range bin, which indicates the upwind situation.

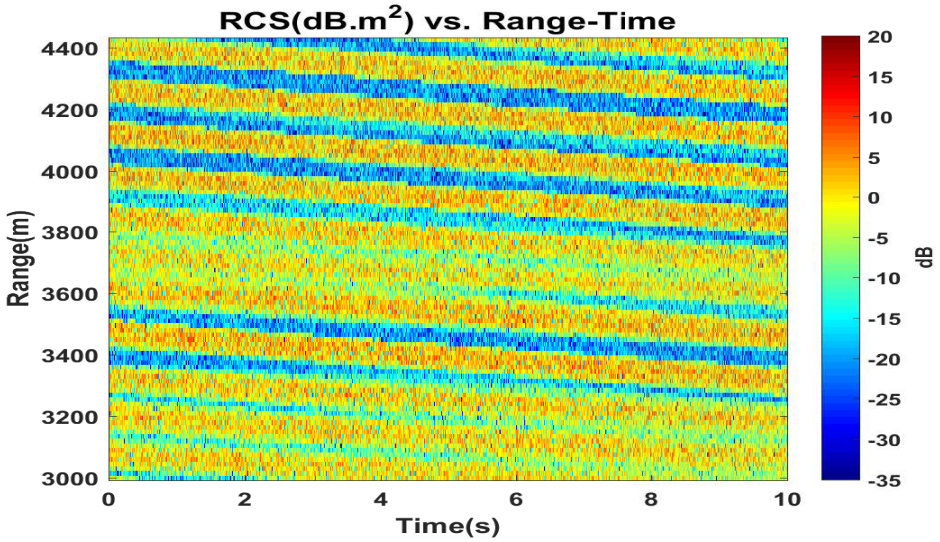

Figure 5.1: Amplitude of resulting complex matrix in range and time for scenario 1.

The log-scaled normalized histograms of obtained $\sigma_0/\overline{\sigma_0}$ values for both simulation result and experimental data CFA16-002 of [16] are presented in Fig. 5.3 and 5.4,

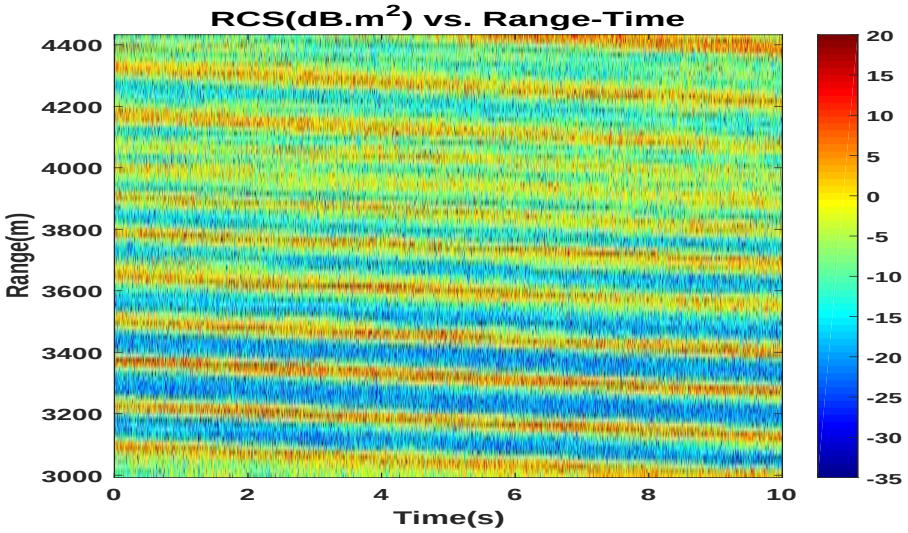

Figure 5.2: Amplitude of experiment data in range and time (CFA16-002 of [16]).

respectively. For these histograms, σ_0 values are also normalized by dividing it to the sample mean value.

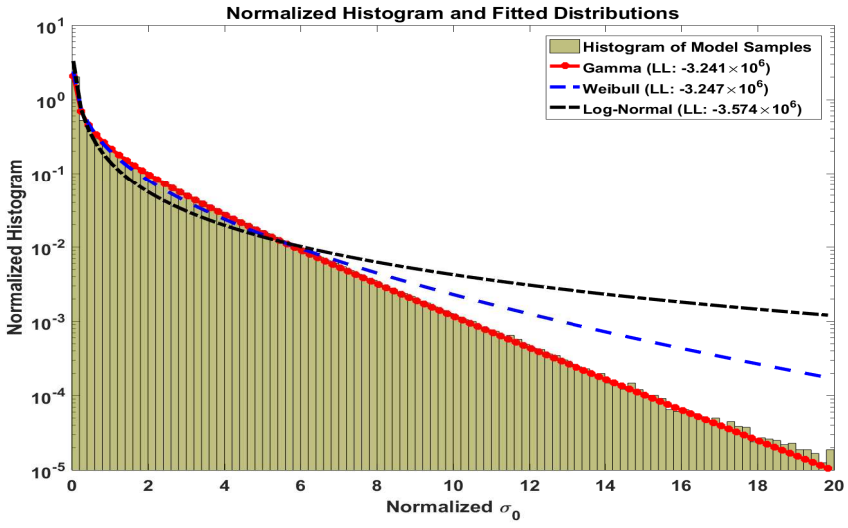

Figure 5.3: Amplitude statistics of the simulation result scenario 1 - Normalized histogram and fitted distribution curves.

For the simulation result, Gamma distribution provides the best fit for σ_0 statistics with respect to the other investigated distributions as Gamma distribution yields the highest Log-likelihood value (as seen on Fig. 5.3). For the fitted Gamma distribution, the shape parameter, a equals to 0.44, and the scale parameter, b equals to 2.275.

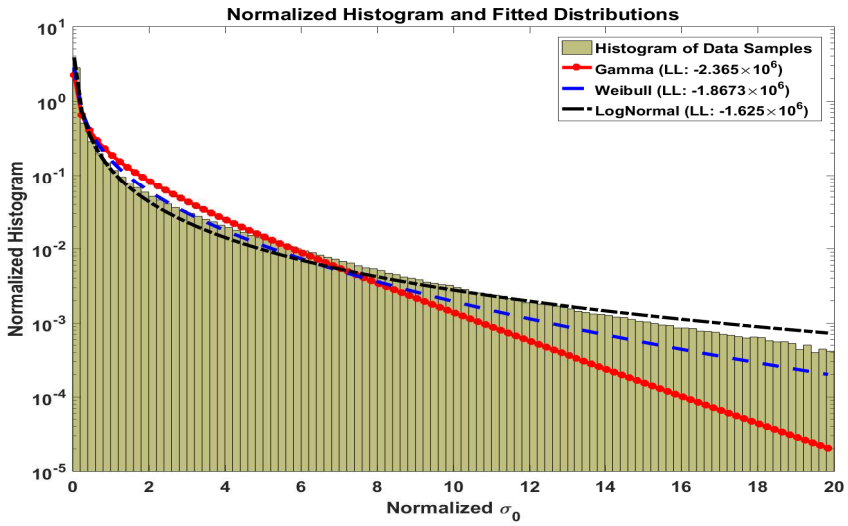

Figure 5.4: Amplitude statistics for the CFA16-002 dataset of [16] - Normalized histogram and fitted distribution curves.

For the CFA16-002 dataset of [16], as resulting highest LL parameter, Log-normal distribution provides the best fit for σ_0 statistics with respect to the other examined distributions (as seen on Fig. 5.4). For the fitted Log-normal distribution, the log mean parameter, μ equals to -1.955, and the log standard deviation parameter, σ equals to 2.221.

5.1.2 Range vs. Time Result for Scenario 2

This scenario is emulated from the CFA16-015 experimental dataset of CSIR [16]. RCS matrix of the proposed model for scenario 2 is given in Fig. 5.5, and amplitude of experimental data CFA16-015 is shown in Fig. 5.6. Notice the difference between previous scenario and this scenario, as slopes of high amplitudes, which are results of crests mostly, in time decrease and amplitudes due to troughs increase.

The log-scaled normalized histograms of obtained $\sigma_0/\overline{\sigma_0}$ values for both simulation result and experimental data CFA16-015 of [16] are illustrated in Fig. 5.7 and 5.8, respectively.

For the simulation result, Weibull distribution yields highest LL value. So, it provides the best fit for σ_0 statistics with respect to the other investigated distributions (as seen

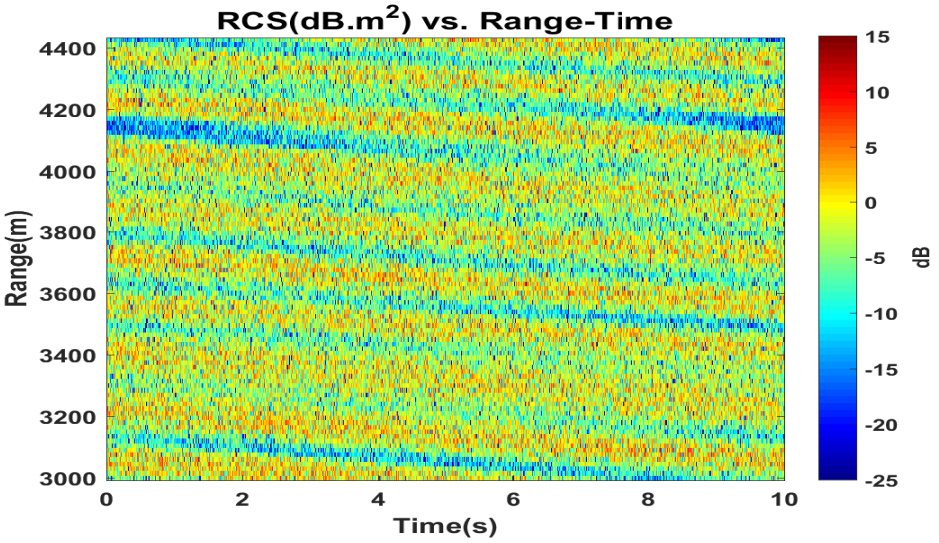

Figure 5.5: Amplitude of resulting complex matrix in range and time for scenario 2.

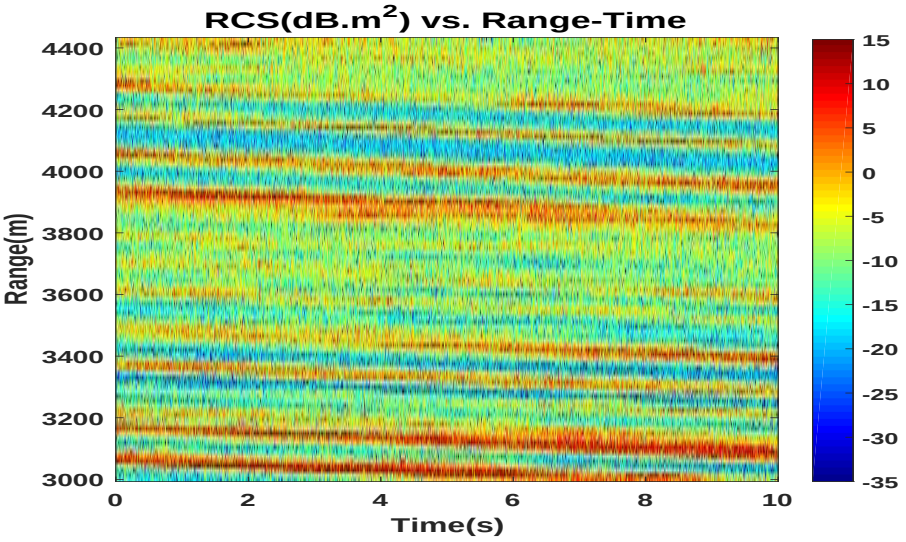

Figure 5.6: Amplitude of experiment data in range and time (CFA16-015 of [16]).

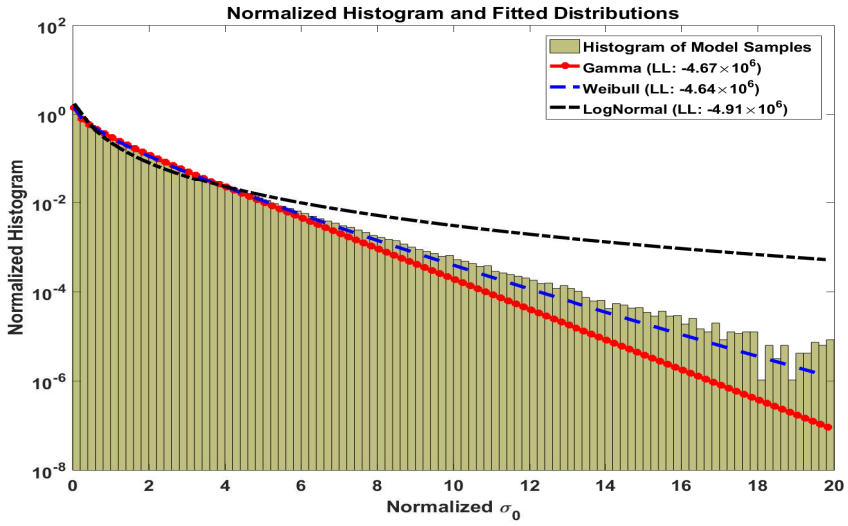

Figure 5.7: Amplitude statistics of the simulation result for scenario 2 - Normalized histogram and fitted distribution curves.

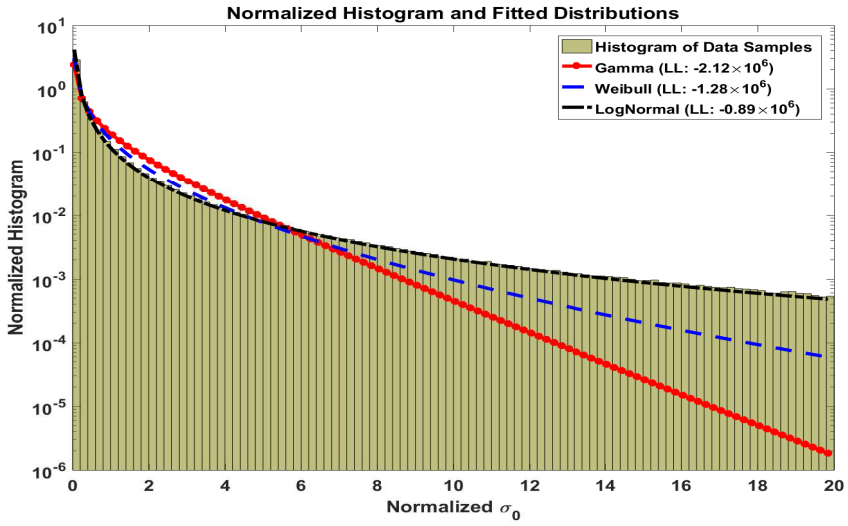

Figure 5.8: Amplitude statistics for the CFA16-015 dataset of [16] - Normalized histogram and fitted distribution curves.

on Fig. 5.7). For the fitted Weibull distribution, the shape parameter, a equals to 0.828, and the scale parameter, b equals to 0.9.

For the CFA16-015 dataset of [16], Log-Normal distribution provides the best fit for σ_0 statistics with respect to the other examined distributions (as seen on Fig. 5.8). Comparison of the goodness of the fits are again determined from the obtained Log-likelihood parameters. For the fitted Log-normal distribution, the log mean parameter, μ equals to -2.02, and the log standard deviation parameter, σ equals to 2.1.

5.1.3 Range vs. Time Result for Scenario 3

RCS matrix for this hypothetical scenario is illustrated in Fig. 5.9. Observe the irregularities in the amplitude distribution, that is, for a single range bin crest-trough-crest or trough-crest-trough pattern is observed. It is estimated that these patterns are formed due to cross-wind condition.

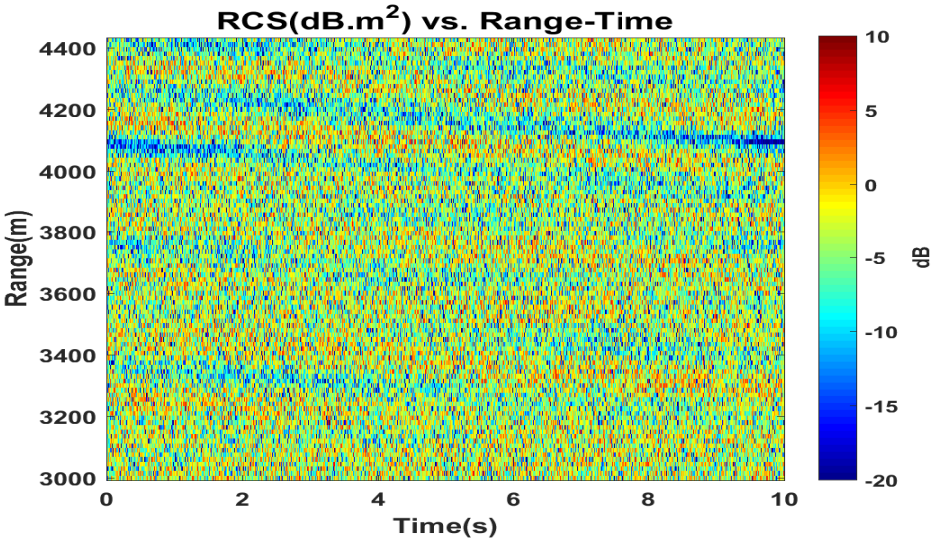

Figure 5.9: Amplitude of resulting complex matrix in range and time for scenario 3.

The log-scaled normalized histogram of obtained $\sigma_0/\overline{\sigma_0}$ values for the simulation result is given in Fig. 5.10.

Comparison of the obtained Log-likelihood parameters (as seen on Fig. 5.10) shows that Weibull distribution provides the best fit for σ_0 statistics with respect to the other inspected distributions. For the fitted Weibull distribution, the shape parameter, a

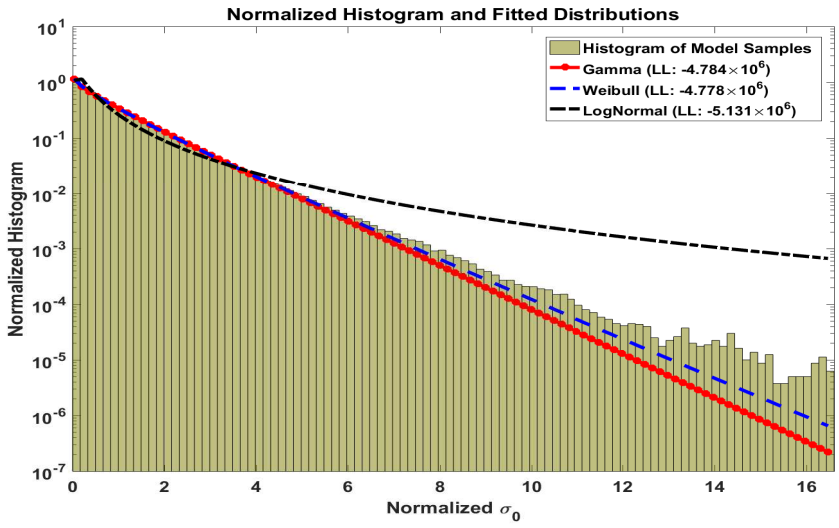

Figure 5.10: Amplitude statistics for the simulation of scenario 3 - Normalized histogram and fitted distribution curves.

equals to 0.931, and the scale parameter, b equals to 0.967.

5.1.4 Range vs. Time Result for Scenario 4

RCS matrix for the hypothetical scenario 4 is demonstrated in Figure 5.11. Notice the difference between Fig. 5.1 and 5.11, as for this case high amplitudes are due to the back faces of the crests which move away from the hypothetic radar.

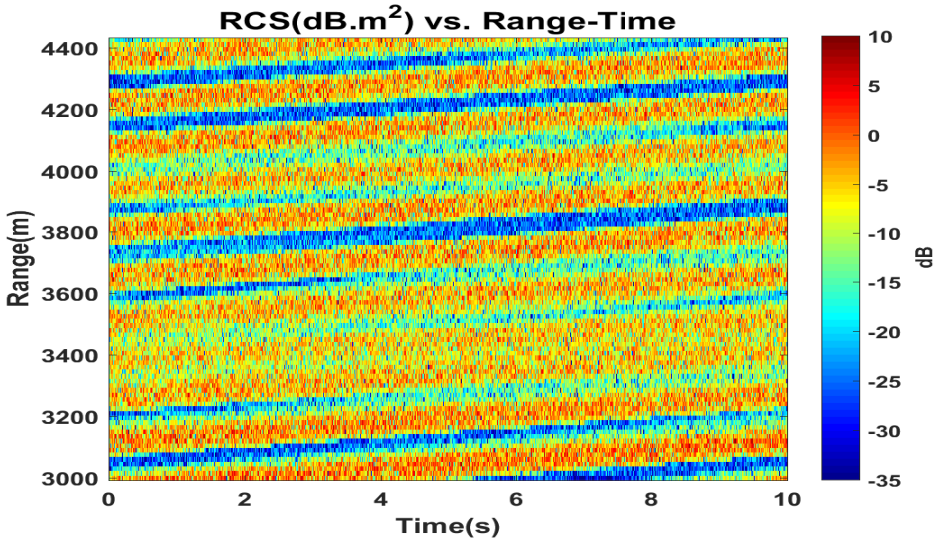

Figure 5.11: Amplitude of resulting complex matrix in range and time for scenario 4.

The log-scaled normalized histogram of obtained $\sigma_0/\overline{\sigma_0}$ values for the simulation result can be viewed in Fig. 5.12.

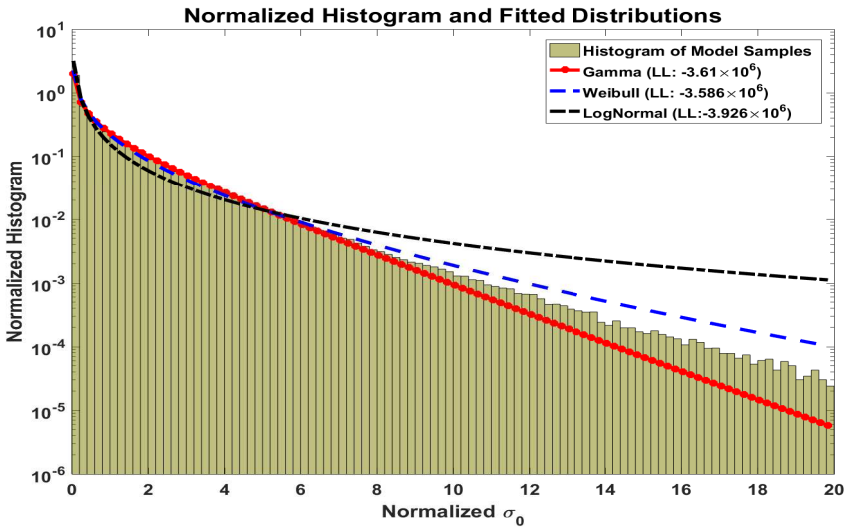

Figure 5.12: Amplitude statistics for the simulation of scenario 4 - Normalized histogram and fitted distribution curves.

Comparison of the obtained LL parameters (as seen on Fig. 5.12) shows that Weibull distribution provides the best fit for σ_0 statistics with respect to the other inspected distributions. For the fitted Weibull distribution, the shape parameter, a equals to 0.609, and the scale parameter, b equals to 0.687.

5.1.5 Comments on Amplitude Results

The simulation results resemble the empirical results [16] in the sense of presented range-time graphs. Almost all range-time plots give an idea about the direction of sea waves. Resulting normalized histograms provide a good fit for the well-accepted sea clutter amplitude distributions. For the scenario 1, our results are quite compatible with the CFA16-002 data of [16]. For this scenario, best-fitted distributions (Gamma for our simulation, Log-normal for the CFA16-002 data of [16]) with the presented parameters are shown in Fig. 5.13. The distributions are normalized based on the probability.

Symmetrized Kullback-Leibler distance [43, 44] between two fitted distributions is

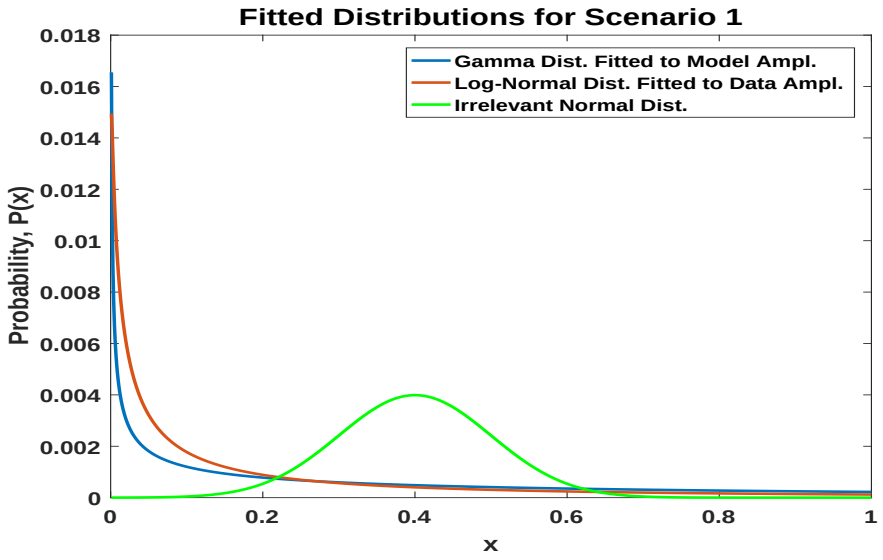

Figure 5.13: Comparison of the fitted amplitude distribution curves for the simulation result and CFA16-002 data [16].

calculated to measure the similarity of these distributions. Since the SKL distance is not an absolute measure, we have added a normal distribution ($\mathcal{N}(0.4,\ 0.1)$), which does not fit neither to data nor to model, to interpret the value of SKL distance correctly. To calculate this distance, we have selected 1000 equally spaced samples, x_i, between 10^{-3} and 1, and evaluated probability values at these sample points, $P(x_i)$, for all distributions. The Kullback-Leibler distance is calculated using these sample values and the formula given below:

$$\mathrm{KL}(P,Q) = \sum_i P(x_i)\ln(\frac{P(x_i)}{Q(x_i)}) \tag{5.1}$$

$$\mathrm{SKL}(P,Q) = \frac{\mathrm{KL}(P,Q)+\mathrm{KL}(Q,P)}{2} \tag{5.2}$$

where P and Q are probability values corresponding to two distributions. Calculated SKL distance between Log-normal distribution fitted to CFA16-002 data [16] and Gamma distribution fitted to amplitude of the model for scenario 1 is about 0.07. The SKL distance between the mentioned Log-normal distribution and irrelevant normal distribution is computed as 1.87. Secondly, we have increased the maximum limit of the samples from 1 to 10. As tail of the distribution curves diminish, SKL distances increases. For this case, while the SKL distance between distributions fitted to model and data increases to 0.12, the SKL distance between distribution fitted to data and irrelevant normal distribution increases beyond the largest number that can be repre-

sented by double precision arithmetic, as a result of relatively small tail probability of the given normal distribution. Note that these distances only provide inference on the similarity between two distributions for given sample interval. Obviously, drawn normal distribution is not even close to be a fit to the given data; however, we can say that fitted distribution to amplitude of the our model provides a good fit to the fitted distribution to the data for the selected sample intervals.

SKL distance is also calculated for scenario 2. While the result is 0.24 for x values taken from 10^{-3} to 1, it is 0.3 for x interval from 10^{-3} to 10. Therefore, our model has provided a better approximation to the data for scenario 1 according to chosen sample interval.

For scenario 3 and 4, one can say that the range-time RCS graphs are similar to the ones in the previous scenarios, and again the extracted amplitude statistics provide acceptable results.

5.2 Simulation Results for Clutter Doppler Shifts

After obtaining the complex matrix, one can show Doppler frequency shifts of the sea clutter in time by utilizing the method of spectrogram. The results shown in the following subdivisions are obtained by spectrogram with non-overlapping windows whose sizes are selected as 1024 sample points. In addition, one should have in mind that each shown time vs. Doppler graph presents results for only single range bin. At the end of this section, mean Doppler spectrums of the proposed model for all four scenarios are presented, and compared with the results of Whitrow [14].

5.2.1 Doppler Frequency Results for Scenario 1

For scenario 1, Doppler shifts in time domain is presented as in Figure 5.14, and the result for its counterpart from the experiment is given in Figure 5.15.

Results shown in Fig. 5.14 and in Fig. 5.15 are only for single range bin. As one can observe the positive Doppler shift from Fig. 5.14, since upwind condition is valid for scenario 1.

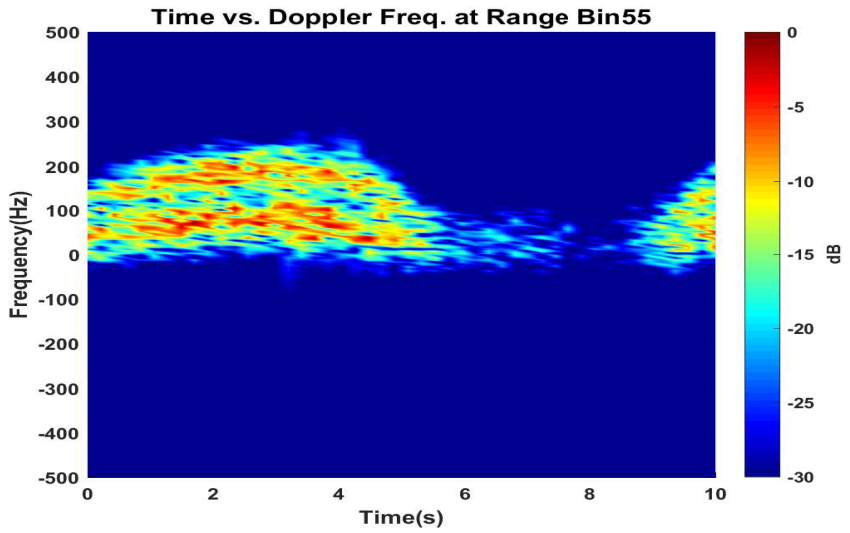

Figure 5.14: Simulation result of Time vs. Doppler frequency at range bin 55 for scenario 1.

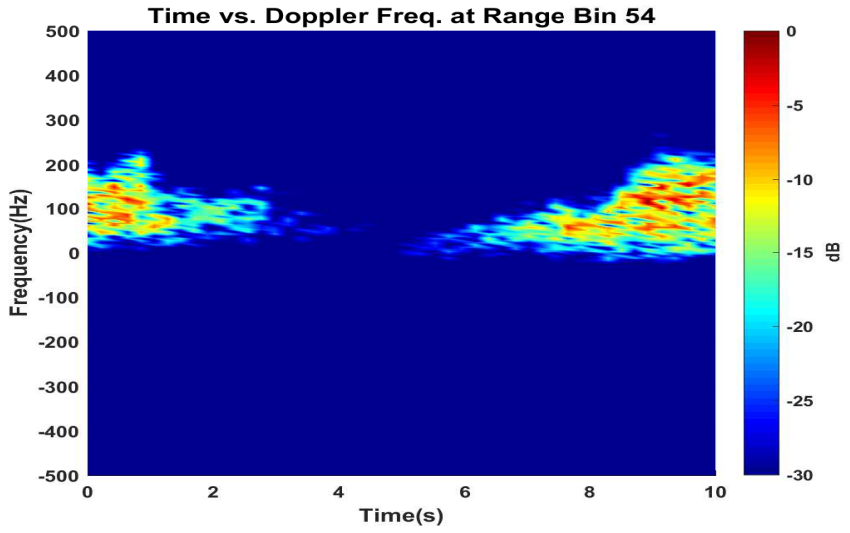

Figure 5.15: Time vs. Doppler frequency graph at range bin 54 for the experiment dataset of CFA16-002 [16]).

Since the created case is very similar to the upwind condition, in Figures 5.16 and 5.17 mean Doppler spectra of both the simulation and CFA16-002 data of [16] can be compared with the mean Doppler spectra data and model proposed to fit that data in [14].

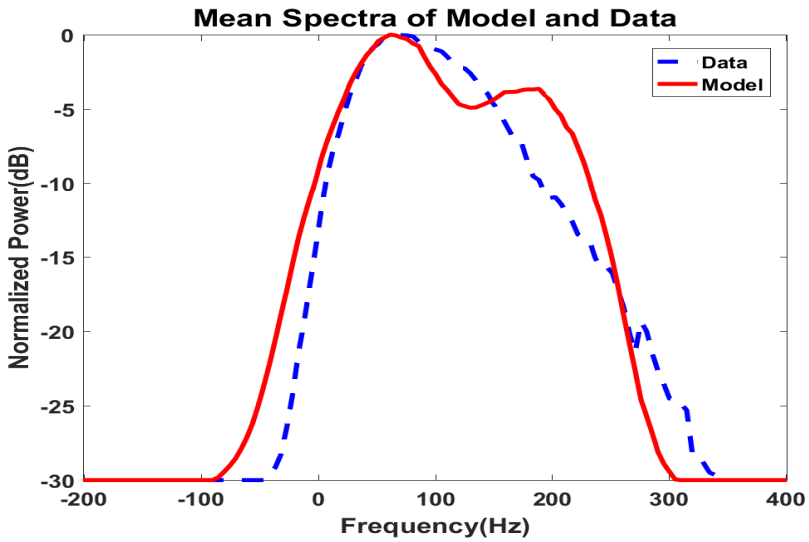

Figure 5.16: Mean Doppler spectra of both the simulation result for the scenario 1 and the CFA16-002 data of[16].

The Doppler spectra of the proposed model shows significant resemblance with the model and data in [14] besides the empirical CFA16-002 data of [16]. The two-sided spectrum in Fig. 5.16 reflects that the spectrum is modeled as a mixture of Bragg and whitecaps Gaussian spectra, and the presented spectrum in Fig. 5.17 verifies it.

5.2.2 Doppler Frequency Results for Scenario 2

For scenario 2, example of Doppler shifts in time domain for a single range bin can be given as in Figure 5.18, and its counterpart from the experiment data CFA16-015 [16] is given in Figure 5.19.

Notice the mean Doppler shift approach to zero mean with respect to the previous case. Mean Doppler spectra of the proposed model and the CFA16-015 data of [16] is illustrated in Fig. 5.20. There is neither model nor data spectra given in [14] that we can compare the results with.

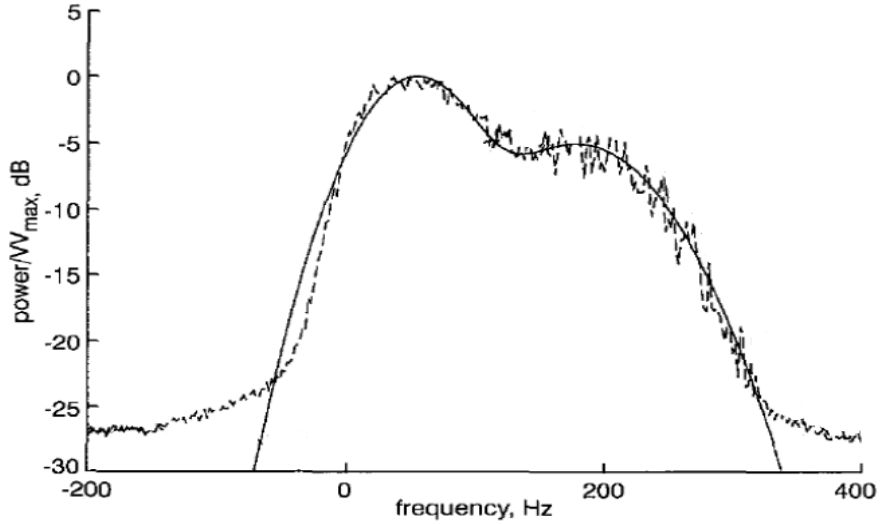

Figure 5.17: Mean Doppler spectra of both the model and the data in [14] for the upwind condition - dashed lines represent the data used in [14], solid line represents the model in [14].

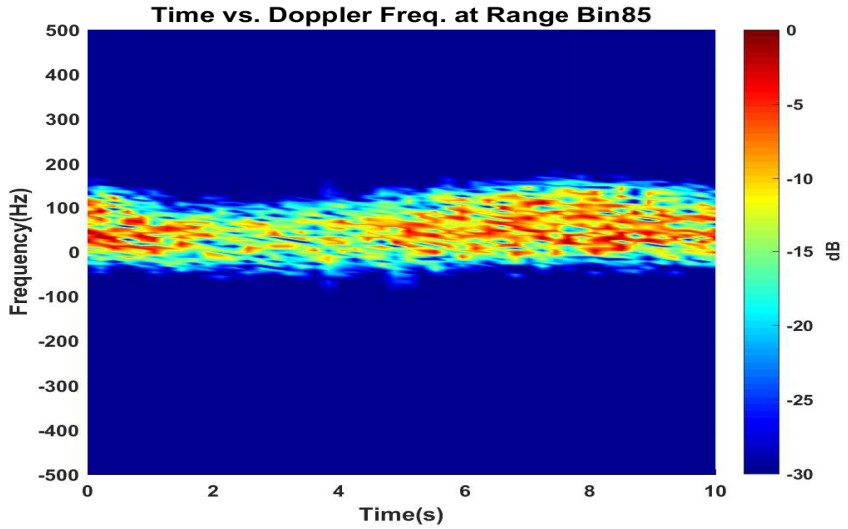

Figure 5.18: Simulation result of Time vs. Doppler frequency at range bin 85 for scenario 2.

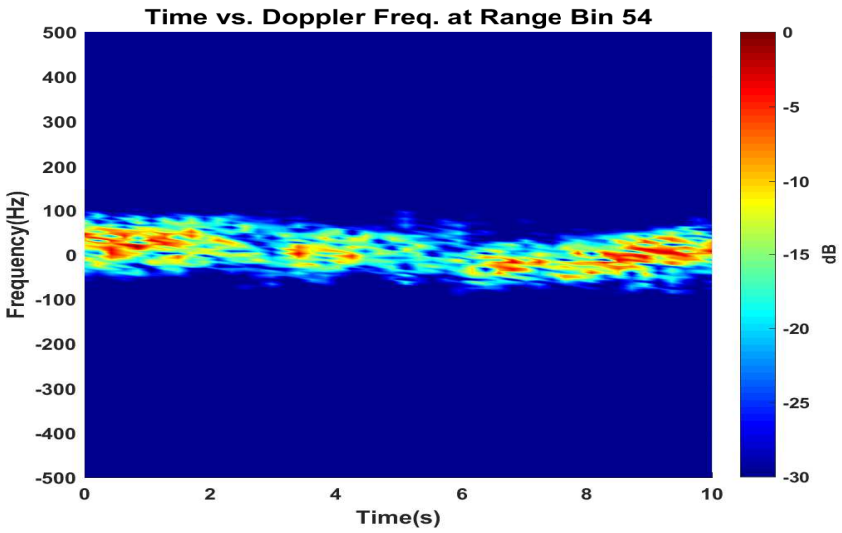

Figure 5.19: Time vs. Doppler frequency graph at range bin 54 for the experiment dataset of CFA16-015 [16]).

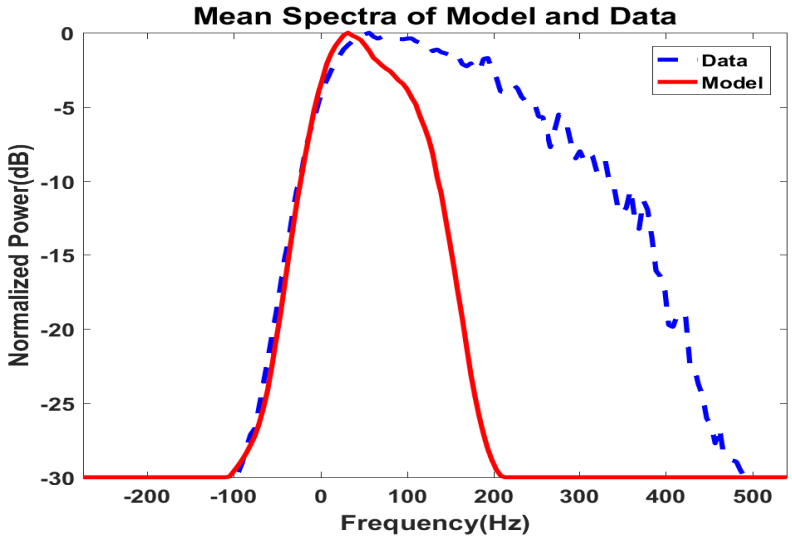

Figure 5.20: Mean Doppler spectra of both the simulation result for the scenario 2 and the CFA16-015 data of [16].

There is an ambiguity for the mean Doppler spectra of the CFA16-015 data of [16]. The reason for this may be the noise increasing noise floor and irregularities in the collected clutter returns. The mean Doppler frequency of the simulated spectra shifts to the zero mean level as expected.

5.2.3 Doppler Frequency Results for Scenario 3

Since there is no available data to compare for the scenario 3, spectrogram result and histograms are given only for the proposed model's resulting matrix. At range bin 75, Doppler shifts in time domain can be viewed in Fig. 5.21.

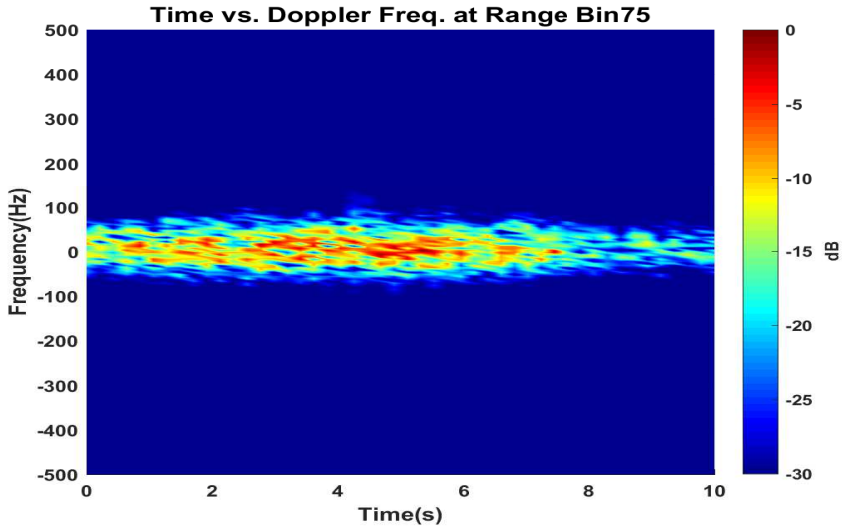

Figure 5.21: Simulation result of Time vs. Doppler frequency at range bin 75 for scenario 3.

One can observe that Doppler shifts occur around the zero-mean. This situation is expected since this scenario represents the almost cross-wind case. The mean Doppler spectra of the simulation result for this scenario is given in Fig. 5.22.

5.2.4 Doppler Frequency Results for Scenario 4

Since there is no available data to compare for the scenario 4, spectrogram result and histograms are given only for the proposed model's resulting matrix. At range bin 55,

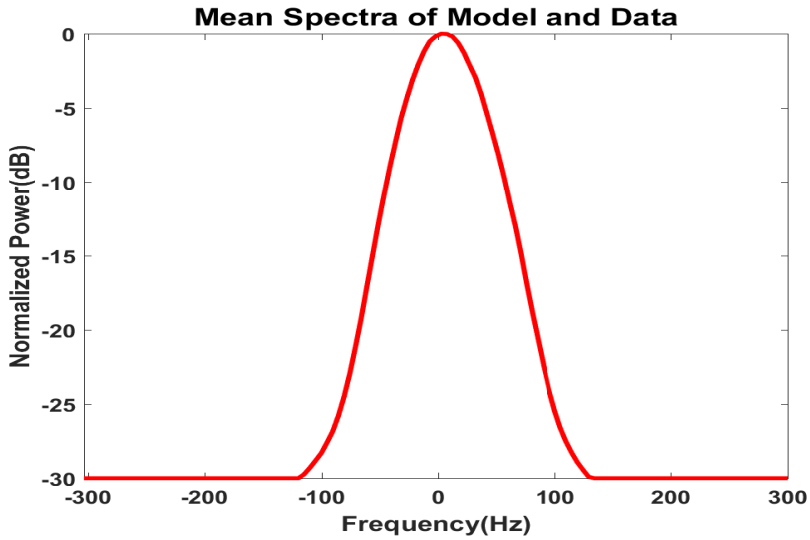

Figure 5.22: Mean Doppler spectra of the simulation result for the scenario 3.

Doppler shifts in time domain can be viewed in Fig. 5.23.

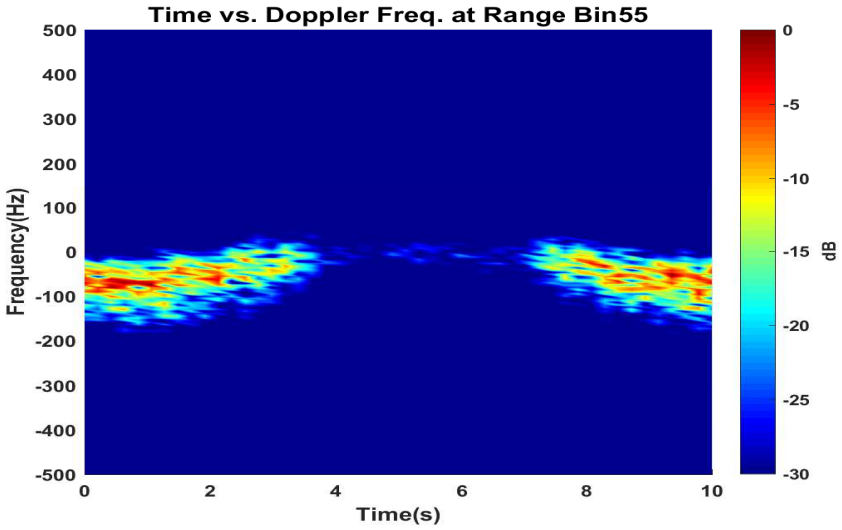

Figure 5.23: Simulation result of Time vs. Doppler frequency at range bin 55 for scenario 4.

One can observe that Doppler shifts occur at negative frequencies. This situation is expected since this scenario represents the down-wind case. The mean Doppler spectra of the simulation result for this scenario is shown in Fig. 5.24, and it can be compared with the mean Doppler spectra of the model and data given in Fig 5.25.

The model curve given in Fig. 5.25 (as solid line), which fits properly to the data pre-

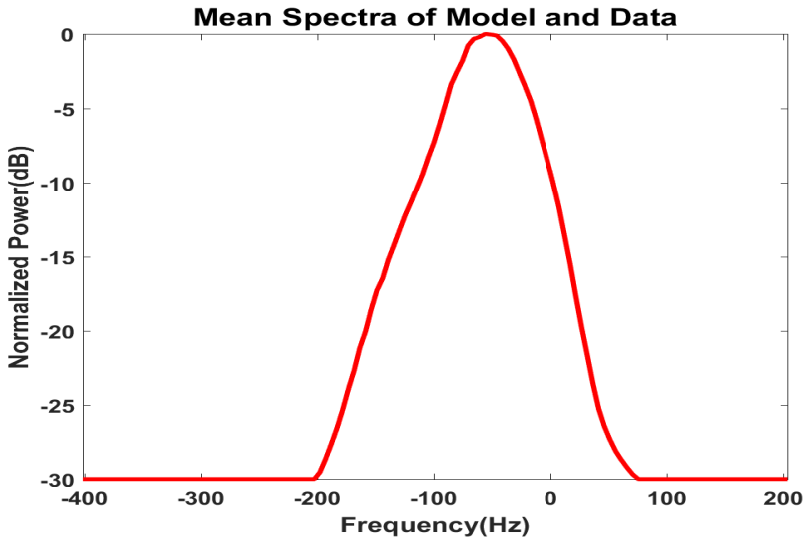

Figure 5.24: Mean Doppler spectra of the simulation result for the scenario 4.

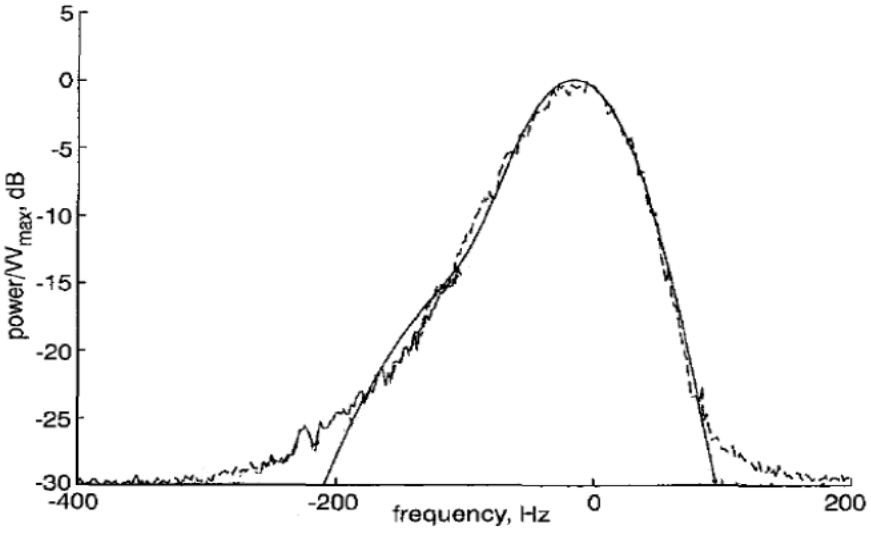

Figure 5.25: Mean Doppler spectra of both the model and the data in [14] for the downwind condition - dashed lines represent the data used in [14], solid line represents the model in [14].

sented in the same figure, ensures that our Doppler spectra is valid for the downwind condition.

5.3 Dispersion Relation Analysis

In this section, we aimed to ensure that sea wave dispersion relation holds for the simulations. For this purpose, the amplitudes of a simulated clutter returns are analyzed by applying 2D FFT. For each scenario, resulting spectral image in spatial-temporal frequency domain is presented. One can observe from the resulting images that there are linear relations between temporal and spatial frequencies. This indicates that the coastal water approximation is valid for the dispersion relation, as $\omega = k\sqrt{gd}$ holds. From the appeared line in the resulting image, we determine the radial velocity using the group velocity relation $v_g = \Delta\omega/\Delta k$, which is given in [20]. Simplifying the angular frequencies to the frequencies results in:

$$v_r = \Delta\omega/\Delta k = \frac{2\pi f_t}{2\pi f_s} = f_t/f_s. \tag{5.3}$$

For the Eq. 5.3, f_t represents temporal frequency and f_s represents spatial frequency.

Radial velocity for the sea waves is related to sea wave velocity as:

$$v_r = v_w \cos\theta_w \tag{5.4}$$

where v_w is the velocity of the sea waves and θ_w is the angle between radar look direction and sea wave direction.

There are two more techniques to determine radial velocity for the given scenarios. First, by using the relation 5.4, we can relate the radial velocity of a scenario to the radial velocity of another scenario as long as the only difference between the scenarios is due to θ_w value. For example, we can determine the radial velocity for the second scenario, from the one obtained for the scenario 1 as $v_{g2} = v_{g1}\cos\theta_w$ can be assumed (since we have upwind condition for the first scenario). Second, by using the 2D range time intensity graphs given in Sec. 5.1, one can observe the wavelength and the period of the sea waves. As wavelength and period are related to the angular spatial and temporal frequencies ($f_s = 1/\lambda_{water}$, $f_t = 1/T_{water}$), one can determine the magnitude of the radial velocity. For example, high amplitudes represent the

front faces for the scenario 1, while the low amplitudes mostly due to back faces and troughs. The wavelength of the sea waves can be determined by the observation of a slice of time and measuring the distance between two crests or troughs. Similarly, the period of the sea waves can be measured by the observation of a slice of range. Results for these two methods are also given in the following sub-sections.

Before moving onto the scenarios, temporal and spatial domain must be defined. Temporal frequency range is $-2500\,\mathrm{Hz}$ to $2500\,\mathrm{Hz}$, which is limited by the half of PRF. Spatial frequency limits are determined from the range resolution that is used in the simulations. The limits are $\frac{-1}{2}(c\tau/2) = -0.0333\,\mathrm{m}^{-1}$ to $\frac{1}{2}(c\tau/2) = -0.0333\,\mathrm{m}^{-1}$. Temporal frequency resolution is determined from the number of pulses used, and spatial frequency resolution is determined from the number of used range bins. Another important note is that sample points are taken from the appeared line of the spectral image by visual inspection, and shown images are scaled in temporal frequency.

5.3.1 Dispersion Relation Analysis for Scenario 1

The normalized spectrum of the proposed model's amplitude matrix (RCS) for scenario 1 is illustrated in Fig. 5.26, while its counterpart from CFA16-002 data of [16] is given in Fig. 5.27.

By taking two data points from the each appeared line on created images, spatial and temporal frequency changes are determined:

- For the proposed model, temporal frequencies selected on the appeared line are as $f_{t_1} = -0.25\,\mathrm{Hz}$ and $f_{t_2} = 0.35\,\mathrm{Hz}$. Chosen spatial frequencies are as $f_{s_1} = -0.0228\,\mathrm{m}^{-1}$ and $f_{s_2} = 0.0235\,\mathrm{m}^{-1}$. So, the differences are given as follows:

$$\Delta f_t = 0.6\,\mathrm{Hz}, \quad \Delta f_s = 0.046\,\mathrm{m}^{-1}. \tag{5.5}$$

  Calculation of the radial velocity of the sea waves for the proposed model is as:

$$v_{rM1} = \frac{\Delta f_t}{\Delta f_s} = 13.04\,\mathrm{m/s}. \tag{5.6}$$

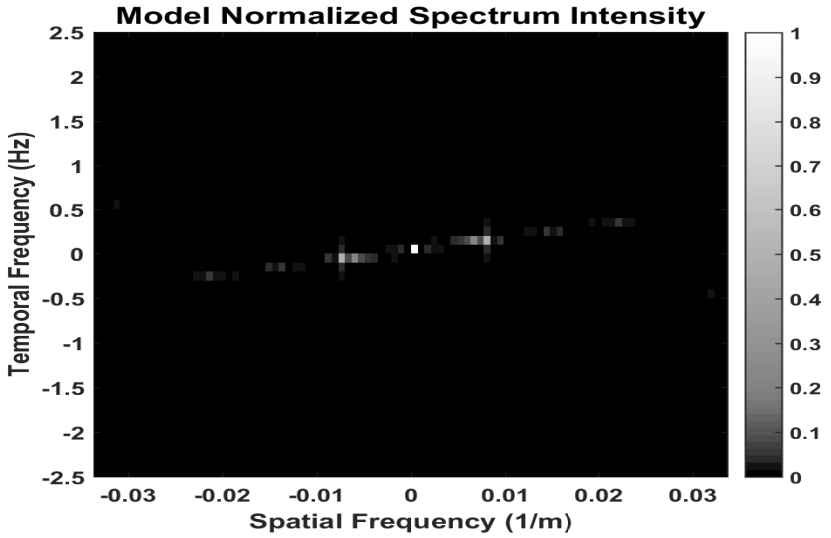

Figure 5.26: Normalized spectrum intensity of the simulated RCS for scenario 1, in spatial-temporal frequencies.

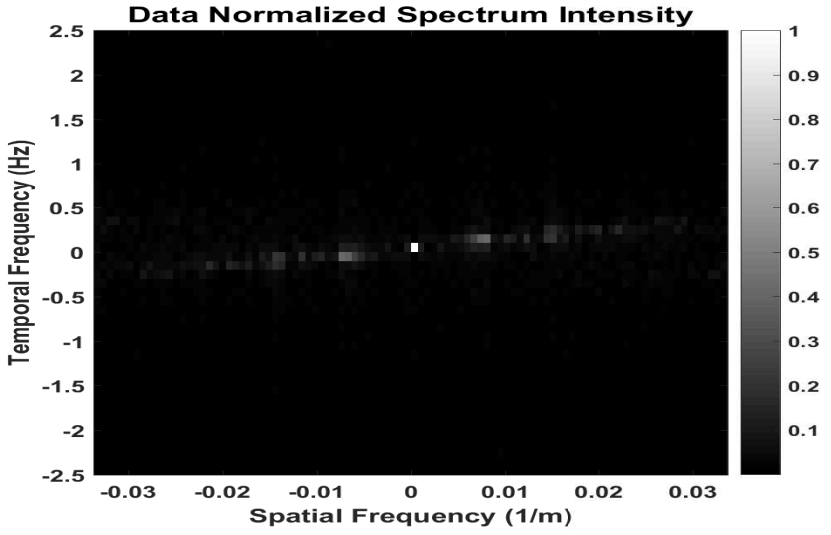

Figure 5.27: Normalized spectrum intensity of the CFA16-002 data [16] RCS, in spatial-temporal frequencies.

One can also estimate the magnitude of the radial velocity from the obtained range intensity graphs in Sec. 5.1. From Fig. 5.1, inspected sea wave wavelength and period are approximately as follows:

$$\lambda_{water} = 135\,\mathrm{m}, \quad T_{water} = 9.2\,\mathrm{s}. \tag{5.7}$$

Using $f_t/f_s = \lambda_{water}/T_{water}$ transition, the obtained radial velocity with this method equals to $14.67\,\mathrm{m/s}$, and is consistent with the one obtained from the spectral image.

- For the CFA16-002 data of [16], temporal frequencies selected on the appeared line are as $f_{t_1} = 0.35\,\mathrm{Hz}$ and $f_{t_2} = 0.35\,\mathrm{Hz}$. Chosen spatial frequencies are as $f_{s_1} = -0.029\,\mathrm{m}^{-1}$ and $f_{s_2} = 0.028\,\mathrm{m}^{-1}$.

$$\Delta f_t = 0.7\,\mathrm{Hz}, \quad \Delta f_s = 0.057\,\mathrm{m}^{-1}. \tag{5.8}$$

Calculation of the radial velocity for the data is given as follows:

$$v_{rD1} = \frac{\Delta f_t}{\Delta f_s} = 12.28\,\mathrm{m/s}. \tag{5.9}$$

Estimated sea wavelength and period from Fig. 5.2 are approximately as follows:

$$\lambda_{water} = 135\,\mathrm{m}, \quad T_{water} = 10.7\,\mathrm{s}. \tag{5.10}$$

Using $f_t/f_s = \lambda_{water}/T_{water}$ transition, the obtained radial velocity equals to $12.62\,\mathrm{m/s}$, and is consistent with the one obtained from the spectral image.

The selected SWH for our simulation corresponds to the wind speed of 11-13 m/s, which we consider as wave speed. Normally, wind speed is given as $U = 8.18\mathrm{m/s}$ for CFA16-002 data of [16]. Yet, the radial velocity obtained for the data verifies our assumptions. If we do not modify the GIT model that uses SWH as input, we would not get compatible radial velocity with the one obtained from the data, that is, greater discrepancy between them would be expected.

In addition, obtained radial velocities show real sea wave velocities in deed. As being positive and high, these radial velocities reflect that the sea waves move directly towards radar.

5.3.2 Dispersion Relation Analysis for Scenario 2

The normalized spectrum of the proposed model's RCS for scenario 2 is illustrated in Fig. 5.26, while its counterpart from CFA16-015 data of [16] is given in Fig. 5.27.

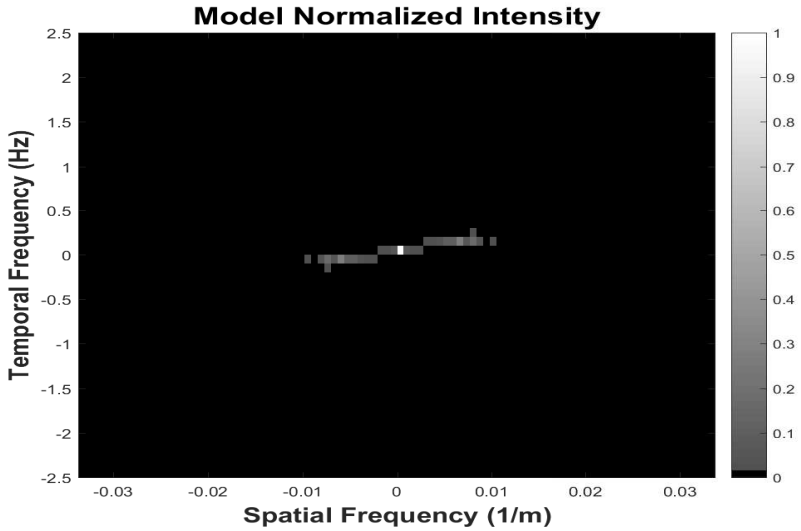

Figure 5.28: Normalized spectrum intensity of the simulated RCS for scenario 2, in spatial-temporal frequencies.

- For the proposed model, temporal frequencies selected on the appeared line are as $f_{t_1} = -0.05\,\mathrm{Hz}$ and $f_{t_2} = 0.15\,\mathrm{Hz}$. Chosen spatial frequencies are as $f_{s_1} = -0.0095\,\mathrm{m}^{-1}$ and $f_{s_2} = 0.0102\,\mathrm{m}^{-1}$. The radial velocity of the sea waves is given as:

$$\Delta f_t = 0.2\,\mathrm{Hz}, \quad \Delta f_s = 0.0197\,\mathrm{m}^{-1}$$
$$v_{rM2} = \frac{\Delta f_t}{\Delta f_s} = 10.1760\,\mathrm{m/s}. \tag{5.11}$$

  The result in Eq. 5.11 can also be validated through using the radial velocity, v_{rM1} and $\theta_w = 42°$:

$$v_{rM1} \cos\theta_w = 9.69\,\mathrm{m/s}. \tag{5.12}$$

  In addition, using the estimated sea wave wavelength $(90\,\mathrm{m})$ and period $(8.54\,\mathrm{s})$ from Fig. 5.5, and using $f_t/f_s = \lambda_{water}/T_{water}$ transition, radial velocity is obtained and it equals to $10.54\,\mathrm{m/s}$. Obtained radial velocities shows consistence which verifies the generated sea surface for the second scenario.

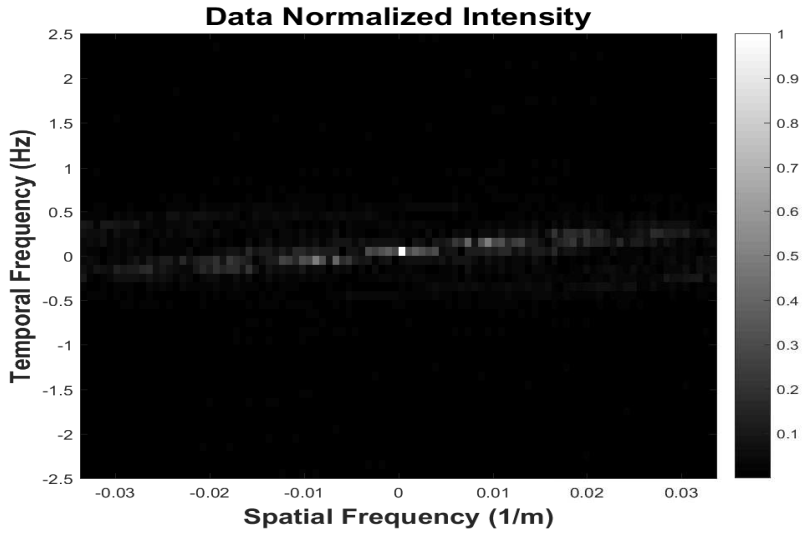

Figure 5.29: Normalized spectrum intensity of the CFA16-015 data [16] RCS, in spatial-temporal frequencies.

- For the CFA16-015 data of [16], temporal frequencies selected on the appeared line are as $ft_1 = -0.15\,\mathrm{Hz}$ and $f_{t_2} = 0.25\,\mathrm{Hz}$. Chosen spatial frequencies are as $f_{s_1} = -0.0249\,\mathrm{m}^{-1}$ and $f_{s_2} = 0.0221\,\mathrm{m}^{-1}$. The radial velocity of the sea waves is computed as:

$$\Delta f_t = 0.4\,\mathrm{Hz}, \quad \Delta f_s = 0.047\,\mathrm{m}^{-1}$$
$$v_{rD2} = \frac{\Delta f_t}{\Delta f_s} = 8.51\,\mathrm{m/s}. \tag{5.13}$$

  The result in Eq. 5.13 can also be validated by using the obtained radial velocity of the CFA16-002 data in [16] and $\theta_w = 42°$:

$$v_{rD1} \cos\theta_w = 9.13\,\mathrm{m/s}. \tag{5.14}$$

  Moreover, using the determined sea wave wavelength of $105\,\mathrm{m}$ and period of $9.64\,\mathrm{s}$ from Fig. 5.5, and using $f_t/f_s = \lambda_{water}/T_{water}$ transition, radial velocity is obtained and it equals to $10.89\,\mathrm{m/s}$. Obtained radial velocities shows consistence for the experimental data as it is expected.

5.3.3 Dispersion Relation Analysis for Scenario 3

The normalized spectrum of the proposed model's RCS for scenario 3 is illustrated in Fig. 5.30.

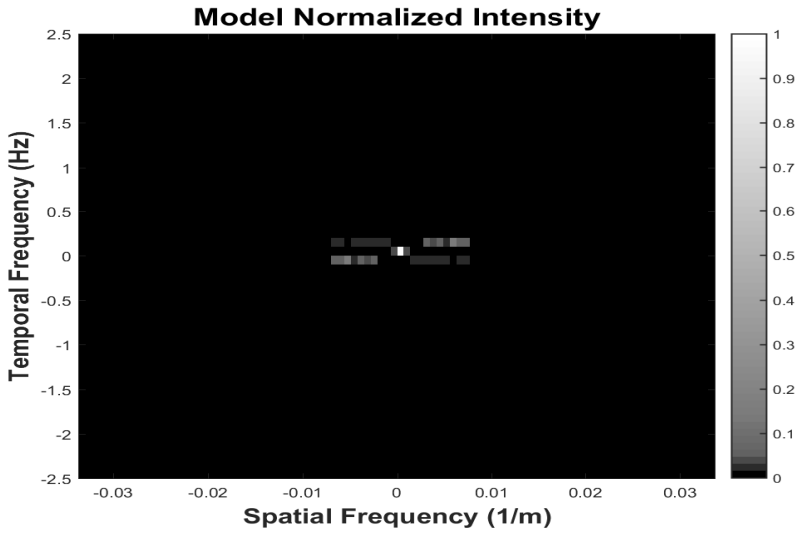

Figure 5.30: Normalized spectrum intensity of the simulated RCS for scenario 3, in spatial-temporal frequencies.

One can notice the line becomes more parallel as it reflects the fact that the radial velocity of sea waves decreases near to zero level. Since the temporal resolution is low, determining the radial velocity from the resulting spectral image is very difficult. Thus, only the expected radial velocity is given for this scenario as:

$$v_{rM3} \cos \theta_w = 2.26 \, \mathrm{m/s}. \tag{5.15}$$

Also, it is difficult to extract sea wave wavelength and period from the Fig. 5.9. Since the scenario is based on almost cross-wind condition, the period of generated sea waves cannot be estimated from single range bin.

5.3.4 Dispersion Relation Analysis for Scenario 4

The normalized spectrum of the proposed model's RCS for scenario 4 is illustrated in Fig. 5.31.

Notice the difference between the lines appeared in Fig. 5.26 and Fig. 5.31. The reason for this situation is the generated sea surfaces for the scenario 1 and scenario 4 move towards opposite directions. As this scenario represents the downwind condition, the expected radial velocity is negative. Obviously, the slope of the line appeared in Fig. 5.31 is negative, that indicates our basic expectation has already been met.

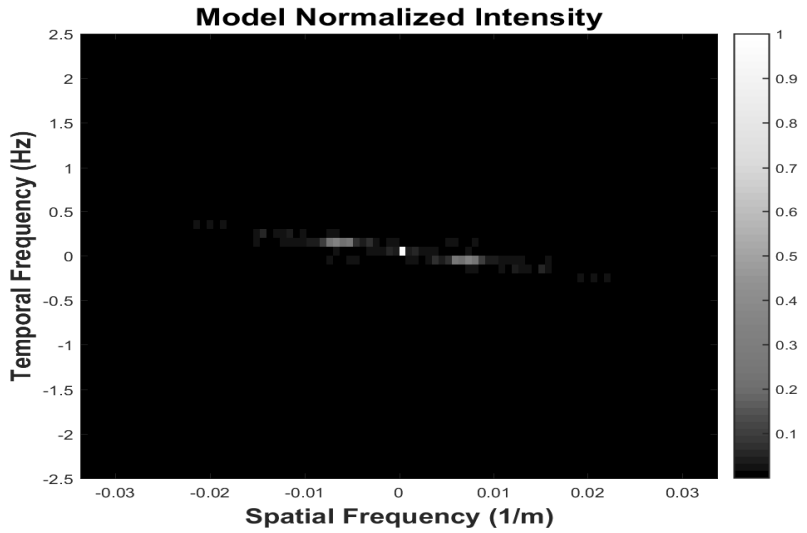

Figure 5.31: Normalized spectrum intensity of the simulated RCS for scenario 4, in spatial-temporal frequencies.

Temporal frequencies selected on the appeared line are as $f_{t_1} = 0.35\,\mathrm{Hz}$ and $f_{t_2} = -0.25\,\mathrm{Hz}$. Chosen spatial frequencies are as $f_{s_1} = -0.0214\,\mathrm{m}^{-1}$ and $f_{s_2} = 0.022\,11\,\mathrm{m}^{-1}$.

$$\Delta f_t = 0.6\,\mathrm{Hz}, \quad \Delta f_s = 0.0435\,\mathrm{m}^{-1} \tag{5.16}$$

Calculation of the radial velocity for the proposed model is given as follows:

$$v_{rM4} = \frac{\Delta f_t}{\Delta f_s} = -13.79\,\mathrm{m/s}. \tag{5.17}$$

The radial velocity found almost equals to the negative of the radial velocity calculated in 5.6, $v_{rM4} = -v_{rM1}$, as expected.

In addition, using the approximate sea wave wavelength of $135\,\mathrm{m}$ and period of $8.62\,\mathrm{s}$ determined from Fig. 5.11, and using $f_t/f_s = \lambda_{water}/T_{water}$ transition, the magnitude of the radial velocity (radial speed) is obtained and it equals to $15.66\,\mathrm{m/s}$. Obtained radial velocities verify the validation of the generated down-wind sea surface.

5.3.5 Comments on Dispersion Relation Analysis

The simulation results basically show that the dispersion relation holds and mentioned coastal water approach is valid. The obtained radial velocities are logical. Slopes of

the appeared lines are compatible with the direction of the generated sea waves for each scenario. The occurred discrepancies may be due to as follows:

- Low resolution of temporal and spatial frequencies,
- Randomness of generated sea surfaces,
- Sample points chosen by visual inspection of the spectral images.

5.4 Brief Evaluation of The Simulation Results

Simulation results compared with the experimental data and/or the results in literature show that the proposed sea clutter model is valid. Other simulation results that are not compared in this work also indicate that modeled Doppler shifts are acceptable as well as the obtained amplitude and radial velocity results. In the simulation time aspect, our algorithms operate fast during the simulations. To give an example, for a scenario containing sea surface motion of ten seconds and ninety-six range bins, the total simulation duration lasts about thirty seconds on a computer having 16 GB RAM.

CHAPTER 6

CONCLUSIONS

Sea clutter has been a problematic issue during the detection of targets, especially at low grazing angles. Over the decades, characterization and simulation of sea clutter have been made to lower its effects on detection and recognition of the targets. However, the general trend of such characterizations is to model sea clutter statistically, that is, amplitude and Doppler shifts of the clutter are generally modeled in terms of mean and standard deviation values for a given environmental condition. These statistical values are extracted in a long observation time, and therefore such models cannot characterize the sea clutter scattering parameters based on the instantaneous physical sea surface. In addition, applying computational EM methods like FEM or MOM to determine scattering parameters of the sea surfaces for a short time is computationally expensive.

In this thesis, we proposed a new model that enables one to observe changes in the clutter's amplitude and Doppler shifts which are compatible with the sea surface itself. To this end, the geometric optics is applied to the dynamic sea surfaces generated by using WAFO and WAFOL toolboxes. Resulting grazing angles are used as inputs of the modified GIT model besides of radar frequency, angle between radar and sea wave direction, significant wave height. Modified GIT model is applied for each patch to obtain NRCS values. These NRCS values may be attenuated based on the visibility analysis performed by X-Draw algorithm. The attenuation is applied to the non-visible sea surface patches according to the obtained grazing angles. The amplitude variance of the proposed model is then determined by computing the RCS of each range bin. In addition to these, Doppler spectra of the clutter are modeled based

on the resulting amplitude variance matrix and given environmental conditions. Mean Doppler spectra are defined by the two component Gaussian spectrums, however; the fluctuations on the spectra are given by the obtained RCS values. In addition, some modifications are made on the mean parameters to enhance the similarity between the proposed model and the presented experimental results. Fourier synthesis method is employed to obtain complex scattering parameter from the resulting amplitude variance and Doppler spectra. During the synthesis, we ensure that the average power is conserved. Then, the complex radar data matrix is constructed concatenating each range bin data. Lastly, we give discussions on the limitations of the suggested model.

In this study, we also showed the simulation results of four different scenarios. The sea waves in each scenario move towards different direction, while the other conditions are chosen to be same. The simulation results for each scenario is compared with either the empirical data or the ones shown in the literature. The simulation results can be categorized in three groups. The first group is the amplitude, RCS, results which are presented in range-time graphs. Moreover, NRCS values obtained from the resulting RCS matrices are illustrated in histograms. By fitting the statistical clutter amplitude models like Weibull, Log-normal and Gamma distributions, we verified that our amplitude results are acceptable in the statistical manner. The second group is the Doppler spectra analysis of the simulation results. The comparisons of time-Doppler graphs are made in order to examine the changing Doppler shifts in a short observation time. Furthermore, resulting mean Doppler spectra for each scenario are plotted with the ones obtained from the available empirical data and compared with the mean Doppler spectra of sea clutter presented in the literature, if available. The third and final group is the dispersion relation analysis which implies the calculation of the radial velocity of the sea waves. This analysis is performed to validate our sea surface model, as obtained radial velocities are reasonable and compatible with the ones obtained from the experimental data. Almost all simulation results demonstrate that the proposed model for the sea clutter is feasible and it shows good agreement with the compared data. Moreover, duration of the simulation for a mentioned scenario indicates the computational rapidness of the suggested algorithms.

6.1 Future Studies

In this thesis, we make some assumptions during the calculation of the clutter returns, and we limited the scope of the study. Therefore, one can enhance the proposed model in a more adaptive way as follows:

- The model can be expanded to the medium and high grazing angles.
- The model can be adapted to the different polarizations like HH, HV and VH polarizations.
- The model can be integrated with other target detection algorithms to simulate small target detection on the sea surface.
- For low sea states, other empirical or statistical models may be employed to characterize the sea clutter more accurately.
- Ray tracing algorithms can be used to observe the multipath effects on the sea clutter besides the shadowing, which is performed via viewshed algorithms in our work.

REFERENCES

[1] K. Ward, S. Watts, R. Tough, I. of Engineering, Technology, and I. of Electrical Engineers, *Sea clutter: scattering, the K-distribution and radar performance 2nd Edition*. IET radar, sonar and navigation series, Institution of Engineering and Technology, 2013.

[2] D. Holliday, L. L. DeRaad, and G. J. St-Cyr, "Forward-backward: a new method for computing low-grazing angle scattering," *IEEE Transactions on Antennas and Propagation*, vol. 44, pp. 722–, May 1996.

[3] F. Arikan and N. Vural, "Simulation of sea clutter at various frequency bands," *Journal of Electromagnetic Waves and Applications*, vol. 19, no. 4, pp. 529–542, 2005.

[4] M. M. Horst, F. B. Dyer, and M. T. Tuley, "Radar sea clutter model," in *Antennas and Propagation*, pp. 6–10, 1978.

[5] F. Nathanson, J. Reilly, and M. Cohen, *Radar Design Principles: Signal Processing and the Environment*. Scitech Pub., 1999.

[6] V. Gregers-Hansen and R. Mital, "An improved empirical model for radar sea clutter reflectivity," *IEEE Transactions on Aerospace and Electronic Systems*, vol. 48, pp. 3512–3524, October 2012.

[7] A. Khenchaf, "Sea clutter and radar complex targets," in *2013 International Conference on Radar*, pp. 11–16, September 2013.

[8] M. Skolnik, *Introduction to Radar Systems*. Electrical engineering series, McGraw-Hill, 2001.

[9] F. Arikan, "Statistics of simulated ocean clutter," *Journal of Electromagnetic Waves and Applications*, vol. 12, no. 4, pp. 499–526, 1998.

[10] W. Pidgeon, "Doppler dependence of radar sea return," *Journal of Geophysical Research*, vol. 73, 02 1968.

[11] P. H. Y. Lee, J. D. Barter, K. L. Beach, C. L. Hindman, B. M. Lake, H. Rungaldier, J. C. Shelton, A. B. Williams, R. Yee, and H. C. Yuen, "X band microwave backscattering from ocean waves," *Journal of Geophysical Research: Oceans*, vol. 100, no. C2, pp. 2591–2611, 1995.

[12] D. Walker, "Experimentally motivated model for low grazing angle radar doppler spectra of the sea surface," *IEE Proceedings - Radar, Sonar and Navigation*, vol. 147, pp. 114–120, June 2000.

[13] D. Walker, "Doppler modelling of radar sea clutter," *IEE Proceedings - Radar, Sonar and Navigation*, vol. 148, pp. 73–80, April 2001.

[14] J. L. Whitrow, "A model of low grazing angle sea clutter for coherent radar performance analysis," tech. rep., Defence Science and Technology Organisation (DSTO), Australia, 2013.

[15] A. D. Rozenberg, D. C. Quigley, and W. K. Melville, "Laboratory study of polarized scattering by surface waves at grazing incidence. i. wind waves," *IEEE transactions on geoscience and remote sensing*, vol. 33, no. 4, pp. 1037–1046, 1995.

[16] P. Herselman, "2006 fynmeet sea clutter measurement trial: Datasets." [Online]. Available: `http://researchspace.csir.co.za/dspace/handle/10204/1847`, September 2007. Accessed on 02/08/2017.

[17] S. Watts, L. Rosenberg, S. Bocquet, and M. Ritchie, "Doppler spectra of medium grazing angle sea clutter; part 1: characterisation," *IET Radar, Sonar Navigation*, vol. 10, no. 1, pp. 24–31, 2016.

[18] WAFO-group, *WAFO - A Matlab Toolbox for Analysis of Random Waves and Loads - A Tutorial*. Math. Stat., Center for Math. Sci., Lund Univ., Lund, Sweden, 2000.

[19] L. G. and P. M., *WafoL - a Wafo module for Analysis of Random Lagrange Waves - Tutorial for WafoL version 1.2*. Math. Stat., Center for Math. Sci., Lund Univ., Lund, Sweden, 2015.

[20] L. Holthuijsen, *Waves in Oceanic and Coastal Waters*. Cambridge University Press, 2007.

[21] M. Skolnik, *Radar Handbook, Third Edition*. Electronics electrical engineering, McGraw-Hill Education, 2008.

[22] "WMO Code Tables." [Online]. Available: `https://www.nodc.noaa.gov/woce/woce_v3/wocedata_1/woce-uot/document/wmocode.htm`, 2002. Accessed on 07/22/2017.

[23] H. Güneş, "Sea Surface Motion Induced Effects on High Frequency Underwater Acoustic Signals," Master's thesis, Middle East Technical University, Turkey, 2014.

[24] R. Stewart, *Introduction to Physical Oceanography*. University Press of Florida, 2009.

[25] A. Techet, "13.42 design principles for ocean vehicles." [Online]. Available: `http://web.mit.edu/13.42/www/handouts/reading-wavespectra.pdf`, 2005. Accessed on 07/22/2017.

[26] W. J. Pierson and L. Moskowitz, "A proposed spectral form for fully developed wind seas based on the similarity theory of sa kitaigorodskii," *Journal of geophysical research*, vol. 69, no. 24, pp. 5181–5190, 1964.

[27] "Ocean-wave spectra - wikiwaves." [Online]. Available: `http://www.wikiwaves.org/Ocean-Wave_Spectra`, 2012. Accessed on 07/22/2017.

[28] K. Hasselmann *et al.*, "Measurements of wind wave growth and swell decay during the joint north sea wave project (jonswap)," *Dtsch. Hydrogr. Z.*, vol. 8, p. 95, 1973.

[29] O. Rodriguez, A. Silva, J. P. Gomes, and S. M. Jesus, "Modeling arrival scattering due to surface roughness," in *Proc. 10th European Conference on Underwater Acoustics*, pp. 1–8, European Conference on Underwater Acoustics, 2010.

[30] M. Richards, W. Holm, and J. Scheer, *Principles of Modern Radar: Basic Principles*. Electromagnetics and Radar, Institution of Engineering and Technology, 2010.

[31] L. Rosenberg and S. Watts, "High grazing angle sea-clutter literature review," tech. rep., Defence Science and Technology Organisation (DSTO), Australia, 2013.

[32] A. M. Raynal and A. W. Doerry, "Doppler characteristics of sea clutter," *New Mexico: Sandia National Laboratories*, 2010.

[33] I. Konuganti, M. Chowdary, and J. Valarmathi, "Sea clutter modelling and target detection," *International Journal of Computer Applications*, 2015.

[34] V. Gregers-Hansen and R. Mital, "An empirical sea clutter model for low grazing angles," in *2009 IEEE Radar Conference*, pp. 1–5, May 2009.

[35] T. Lamont-Smith, K. D. Ward, and D. Walker, "A comparison of em scattering results and radar sea clutter," in *RADAR 2002*, pp. 439–443, October 2002.

[36] Y.-H. Kim, S. Rana, and S. Wise, "Exploring multiple viewshed analysis using terrain features and optimisation techniques," *Computers & Geosciences*, vol. 30, no. 9, pp. 1019–1032, 2004.

[37] J. C. Bravo, T. Sarjakoski, and J. Westerholm, "Efficient implementation of a fast viewshed algorithm on simd architectures," in *2015 23rd Euromicro International Conference on Parallel, Distributed, and Network-Based Processing*, pp. 199–202, March 2015.

[38] B. Kaučič and B. Zalik, "Comparison of viewshed algorithms on regular spaced points," in *Proceedings of the 18th Spring Conference on Computer Graphics*, SCCG '02, (New York, NY, USA), pp. 177–183, ACM, 2002.

[39] M. S. Greco, "Radar clutter modeling." [Online]. Available: `http://www.iet.unipi.it/m.greco/esami_lab/Radar/Clutter_modeling.pdf`. Accessed on 05/01/2018.

[40] F. Arikan and H. Raemer, "A methodology for modeling and simulation of radar clutter and multipath," *Journal of Electromagnetic Waves and Applications*, vol. 10, no. 2, pp. 215–242, 1996.

[41] D. Panchenko, "18.650 Statistics for Applications." [Online]. Available: `https://ocw.mit.edu/courses/mathematics/18-443-statistics-for-applications-fall-2006/`, 2006. Accessed on 22/12/2017.

[42] G. Rodriguez, "Lecture Notes on Generalized Linear Models." [Online]. Available: `http://data.princeton.edu/wws509/notes/`, 2007. Accessed on 17/12/2017.

[43] I. Dagan, L. Lee, and F. Pereira, "Similarity-based methods for word sense disambiguation," in *Proceedings of the 35th ACL/8th EACL*, pp. 56–63, 1997.

[44] Z. Yao, Z. Lai, and W. Liu, "A symmetric kl divergence based spatiogram similarity measure," in *2011 18th IEEE International Conference on Image Processing*, pp. 193–196, 2011.

[45] V. Chen and H. Ling, *Time-frequency Transforms for Radar Imaging and Signal Analysis*. Artech House radar library, Artech House, 2002.

APPENDIX A

SPECTROGRAM

Being visualized as 2D magnitude representation, the spectrogram provides spectral information on the signal of interest at different time instants [45]. The spectrogram can be used to analyze time-frequency characteristics of signals, especially having frequency agility. It is the magnitude squared of the short-time Fourier transform (STFT) of the signal. The STFT of a signal for corresponding range profile is [45]:

$$STFT(t, W) = \int s(t')W(t' - t)exp(-j\omega t')dt' \tag{A.1}$$

where $W(.)$ is a short-time window function.

The spectrogram is defined as the magnitude square of the short-time Fourier transform, $|STFT(t, W)|^2$.

APPENDIX B

SOME STATISTICAL DISTRIBUTIONS USED TO MODEL SEA CLUTTER

B.1 Rayleigh Distribution

It is the basic type of amplitude statistics that models the both land and sea clutter. It represents the envelope of a Gaussian random process. The model becomes more valid when resolution cell size gets larger [8]. The distribution is given as follows:

$$p(x) = \frac{2x}{b^2} \exp\left(-\frac{x^2}{b^2}\right), \quad x \geq 0 \tag{B.1}$$

where b is the scale parameter.

B.2 Log-Normal Distribution

This distribution is constructed to model Non-Rayleigh clutter amplitude [8]. It is represented by the following equation:

$$p(x) = \frac{1}{x\sigma\sqrt{2\pi}} \exp \frac{-(\ln x - \mu)^2}{2\sigma^2}, \quad x \geq 0 \tag{B.2}$$

where μ is the logarithmic mean, and σ is the logarithmic standard deviation.

B.3 Weibull Distribution

The Weibull distribution is the simplest one that fits both land and sea clutter measurements accurately. This distribution provides better fit than both log-normal and

Rayleigh in most conditions [8]. The distribution is as follows:

$$p(x) = \frac{a}{b}\left(\frac{x}{b}\right)^{a-1} \exp\left(-\left[\frac{x}{b}\right]^{a}\right), \quad x \geq 0 \tag{B.3}$$

where a is the shape parameter, b is the scale parameter.

B.4 Gamma Distribution

The exponential and the chi-squared distributions are special cases of this distribution. The envelope of the K-distribution is provided by this distribution. The equation for this distribution is given as follows:

$$p(x) = \frac{1}{b^{a}\Gamma(a)} x^{a-1} \exp\left(\frac{-x}{b}\right), \quad x \geq 0 \tag{B.4}$$

where a is the shape parameter, b is the scale parameter.

B.5 K Distribution

K-distribution is formed from the speckle and texture components. The speckle component varies fast on the order of milliseconds, and it is represented by Rayleigh distribution. On the other hand, the texture component, which is represented by Gamma distribution, varies slowly on the order of seconds [8]. The K-distribution is given as follows:

$$p(x) = \frac{2b}{\Gamma(v)}\left(\frac{bx}{2}\right)^{v} K_{v-1}(bx), \quad x \geq 0 \tag{B.5}$$

where v is the shape parameter, b is the scale parameter.